Spectroscopic Characterization of Extrasolar Planets from Ground-, Space- and Airborne-based Observatories

A thesis accepted by the Faculty of Aerospace Engineering and Geodesy of the Universität Stuttgart in partial fulfilment of the requirements for the degree of Doctor of Natural Sciences (Dr. rer. nat.)

by

Daniel Angerhausen
born in Krefeld-Uerdingen

Committee chair: Prof. Dr. rer. nat. A. Krabbe
Committee member: Prof. Dr. rer. nat. W. Kley
Date of defence: 17.11.2010

German SOFIA Institute
Institute of Space Systems

Universität Stuttgart
2010

Contents

0.1. List of abbreviations and acronyms

AO	Adaptive Optics
CCD	Charge-coupled Device
CoRoT	COnvection, ROtation and planetary Transits
DIT	Detector Integration Time
DDT	Director's Discretionary Time
DRP	data reduction pipeline
ESO	European Organisation for Astronomical Research in the Southern Hemisphere
ExoPTF	ExoPlanet Task Force
FIR	far infrared
FLITECAM	First Light Infrared Test Experiment CAMera
FOV	field of view
FRD	Focal Ratio Degradation
FWHM	full width at half maximum
HAT	Hungarian-made Automated Telescope
HIPO	High-speed Imaging Photometer for Occultation
HST	Hubble Space Telescope
IFS	Integral Field Spectroscopy
IFU	integral field unit
IR	infrared
IRAC	Infrared Array Camera
IRTF	InfraRed Telescope Facility
JWST	James Webb Space Telescope
LMSS	Lower Main-Sequence Stars
LCP	Lomb-Scargle periodogram
MACAO	Multi Application Curvature Adaptive Optics
MAL	micro-lens array
mas	milli-arcsecond
MIR	mid infrared
MOS	multi-object spectroscopy
NASA	National Aeronautics and Space Administration
NDIT	Number of sub integrations with DIT
NEO	near earth Orbit
NICMOS	Near Infrared Camera and Multi-Object Spectrometer
NIR	near infrared
NWO	New World Observer
OSIRIS	OH-Suppressing Infra-Red Imaging Spectrograph
PAC	Pupil Apodization Coronagraph
PAM	pupil alignment mechanism
ppm	parts-per-million
PSF	Point-Spread Function
PT	primary transit

RV	radial velocity
S/N	signal to noise ratio
SINFONI	Spectrograph for INtegral Field Observations in the Near Infrared
SE	secondary eclipse
SOFIA	Stratospheric Observatory for Infrared Astronomy
SpeX	IRTF Medium-Resolution IR Spectrograph
SPIFFI	SPectrograph for Infrared Faint Field Imaging
SST	Spitzer space telescope
ST	secondary transit
STIS	Space Telescope Imaging Spectrograph
STScI	Space Telescope Science Institute
TReS	Trans-Atlantic Exoplanet Survey
UV	ultraviolet
VLT	Very Large Telescope
WASP	Wide Angle Search for Planets
WFC	Wide Field Camera
WISE	Wide-field Infrared Survey Explorer

0.2. Thesis abstract

This thesis deals with techniques and results of observations of exoplanets from several platforms. In this work I present and then attempt solutions to particular issues and problems connected to ground- and space-based approaches to spectroscopic characterization of extrasolar planets. Furthermore, I present the future prospects of the airborne observatory, SOFIA, in this field of astronomy.

The first part of this thesis covers results of an exploratory study to use near-infrared integral-field-spectroscopy to observe transiting extrasolar planets. I demonstrate how adaptive-optics assisted integral field spectroscopy compares with other spectroscopic techniques currently applied, foremost being slit spectroscopy. An advanced reduction method using elements of a spectral-differential decorrelation and optimized observation strategies is discussed. This concept was tested with K-Band time series observations of secondary eclipses of HD 209458b and HD 189733b obtained with the SINFONI at the Very Large Telescope (VLT), at spectral resolution of $R \simeq 3000$. In ground-based near infrared (NIR) observations, there is considerable likelihood of confusion between telluric absorption features and spectral features in the targeted object. I describe a detailed method that can cope with such confusion by a forward modelling approach employing Earth transmission models.

In space-based transit spectroscopy with Hubble's NICMOS instrument, the main source of systematic noise is the perturbation in the instrument's configuration due to the near Earth orbital motion of the spacecraft. I present an extension to a pre-existing data analysis sequence that has allowed me to extract a NIR transmission spectrum of the hot-Neptune class planet GJ436b from a data set that was highly corrupted by the above mentioned effects. Satisfyingly, I was able to obtain statistical consistency in spectra (acquired over a broad wavelength grid) over two distinct observing visits by HST. Earlier reductions were unable to achieve this feat. This work shows that systematic effecting the spectrophotometric light-curves in HST can be removed to levels needed to observe features in the relatively small scale-height atmospheres of hot Neptune class planets orbiting nearby stars.

In the third and final part of this thesis, I develop and discuss possible science cases for the airborne *Stratospheric Observatory for Infrared Astronomy* (SOFIA) in the field of detection and characterization of extrasolar planets. The principle advantages of SOFIA and its suite of instrumentation is illustrated and possible targets are introduced. Possible next generation instrumentation (dedicated to exoplanetary science) is discussed.

0.3. Zusammenfassung der Dissertation

In der hier vorgelegten Dissertation beschreibe ich zunächst die spezifischen Probleme und ihre möglichen Lösungen im Bereich der boden- und weltraum-gebundenen spektroskopischen Charakterisierung von extrasolaren Planeten. Weiterhin werden zukünftige Perspektiven mit dem Flugzeugteleskop SOFIA in diesem Feld präsentiert.

Der boden-gebundene Teil dieser Dissertation beschreibt Ergebnisse einer Beispielstudie zur Anwendung abbildender Spektrographen in der Charakterisierung extrasolarer Planeten. Hier vergleiche ich die Kombination aus adaptiver Optik und abbildender Spektroskopie mit anderen spektroskopischen Methoden, insbesondere der Spalt-Spektroskopie. In diesem Teil diskutiere ich eine fortgeschrittene Methode der Datenreduktion, die Elemente einer spektral-differentiellen Dekorrelation enthält, und erarbeite eine optimale Beobachtungsstrategie. Das hier präsentierte Konzept wurde an K-Band Zeitserien-Beobachtungen eines sekundären Transits der Planeten HD 209458b und HD 189733b getestet. Diese Beobachtung wurden mit dem SINFONI Instrument am Very Large Telescope der ESO (VLT) bei einer spektralen Auflösung von $R \simeq 3000$ durchgeführt. Für boden-gebundene Nahinfrarot-Beobachtungen ist das zentrale Problem die Absorption tellurischer Spurengase wie Wasser oder Methan, die auch in den beobachteten Planeten vermutet werden. In dieser Dissertation beschreibe ich eine Methode zur Lösung dieses Problems, unter anderem durch die Anwendung von Transmissionsmodellen der Erdatmosphäre.

Bei weltraum-gebundenen Beobachtungen der gleichen Art mit dem NICMOS-Instrument des Hubble Weltraumteleskopes ist die Hauptquelle systematischen Rauschens die Störungen in der Instrument-Konfiguration, die durch die Bewegung des Satelliten-Teleskopes durch den erdnahen Orbit hervorgerufen werden. Hier präsentiere ich eine Erweiterung der bestehenden Datenreduktions-Sequenz. Diese Methode konnte aus einem Datensatz, der hochgradig von diesen Effekten gestört ist, ein Nahinfrarot-Spektum des 'heissen Neptun' Planet GJ 436b extrahieren. Im Ergebnis war es mir möglich, ein statistisch konsistentes Spektrum für zwei unabhängig beobachtete Bedeckungen zu berechnen. Diese Arbeit zeigt, dass systematische Effekte in spektro-photometrischen Lichtkurven des Hubble Weltraumteleskops bis auf Niveaus korrigiert werden können, die es ermöglichen, selbst die Atmosphären heisser Neptun Planeten mit relativ kleinen Äquivalenthöhen zu charakterisieren.

Im dritten und letzten Teil der Arbeit entwickle und diskutiere ich zukünftige Einsatzmöglichkeiten des Flugzeugteleskops SOFIA (Stratosphären Observatorium für Infrarot Astronomie) im Bereich der Detektion und Charakterisierung extrasolarer Planeten. Generelle Vorteile von SOFIA und ihrer Instrumentierung werden dargestellt und mögliche Beobachtungs-Projekte vorgestellt. Zuletzt werden mögliche, auf die Charakterisierung von Exoplaneten spezialisierte Instrumente der zweiten Generation diskutiert.

1. Introduction

The first chapter is an introduction to the scientific field of extrasolar planets. I discuss the central questions that trigger the exploration in this field. I also present important milestones of discoveries and discuss observational challenges. Solutions are presented and the method of transit spectroscopy is motivated. Finally I will give a brief introduction to exoplanetary atmospheres, which are the main target of this work.

1.1. Extrasolar planets

1.1.1. Science motivation

The exploration of extrasolar planetary systems is intimately connected to a series of questions important to modern astronomy and to mankind at large. Questions that fascinate me personally about *origins* can be formulated simply, but are of increasing complexity:

How do planetary systems form and evolve?

How many habitable planets are there?

What are the chances for bioactive systems or even life on other planets?

How and where does biotic, prebiotic chemistry evolve?

How and where does life evolve?

Where does mankind come from? Are we alone in the universe?

These are also philosophical questions, and will be the primary science drivers for this field of inquiry for as long as the long term goals of observing the first signs of life on an extrasolar Earth analog are not surmounted. Scientists and technologists have banded together (in conferences and working groups such as Pathways, Blue Dots and ExoPTF) to formulate a set of milestones of key projects that can enable tackling of these grand goals. Furthermore, the importance of these questions is amplified by the great public interest in the physical properties of extrasolar planets and the ultimate question of NASA's *origins* program.

1.1.2. Milestones of discoveries

Ever since the first detection of an exoplanet orbiting a main sequence star in 1995 (Mayor & Queloz), and the first observation of an exoplanet transiting its host star (Henry et al., 2000), entirely new successes like the detection of atoms and molecules in the atmospheres of giant planets (Charbonneau et al., 2002; Swain, Vasisht & Tinneti, 2008), or the direct imaging of a multiple planet system around the A5V-star HR 8799 (Marois et al., 2008) have been made (see fig. 1.1). Within this context it is hardly a surprise that exoplanet research is actually of one the fastest growing areas in any field of scientific inquiry these days. The number of known planets is steadily on the rise (see fig. 1.2). More transiting exoplanets will be detected from the ground, and with space-based fixed-line-of-sight surveys such as CoRoT and the recently launched *Kepler*, and possibly with future orbiting all-sky monitors. Radial velocity surveys may continue to improve in sensitivity, and imaging-spectroscopy instruments on large telescopes with next-generation adaptive optics will bear results in the next few years. A quick literature search shows that both aspects of extrasolar planet science, observational as well as theoretical, are growing exponentially and spinning off specialized fields such as e.g. astrobiology or exoplanetary meteorology.

The growing sample of planets must, however, be characterized by spectroscopic methods. Here, the greatest successes have been with the stable space-based platforms such as the Hubble and Spitzer space telescopes. One of the main bottlenecks in follow-up spectroscopic characterization today is due to the reduced capabilities of warm Spitzer, and

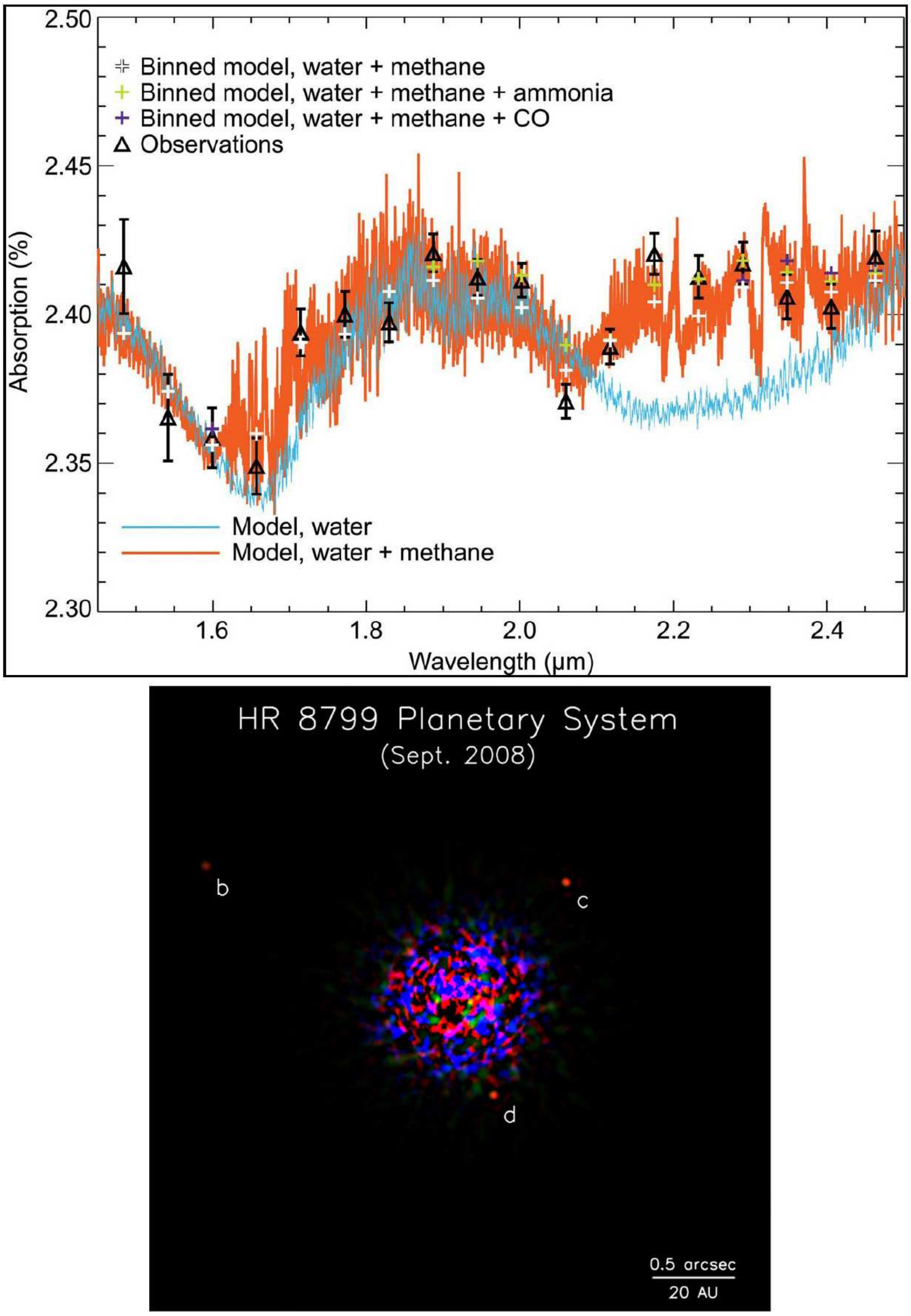

Figure 1.1.: Example of two major discoveries in the field of extrasolar planets in 2008: the detection of methane in the atmosphere or HD 189733b (Swain, Vasisht & Tinneti, 2008; top) and the direct imaging of the multiple system HR 8799 (Marois et al., 2008; bottom).

on-going technical problems with Hubble's near-infrared NICMOS instrument (although some of these may be overcome if observers are able to utilize the infrared channel of the new WFC 3, see 1.4 and 5.2).

1.2. Characterization of extrasolar planets

1.2.1. Observational challenges

Observations of extrasolar planets are always limited by the contribution of their parent stars. While 'Hot Jupiters' for example show a reasonable IR-contrast ratio but are too close to parent star to be spatially separated with today's telescopes, other extrasolar substellar objects such as *Epsilon Eridani* show a reasonable angular separation. However, since they are much more separated from their host-star they are cooler and therefore have a much lower contrast in the optical and near-infrared (see fig.1.3). To separate the planetary signal in imaging as well as in spectroscopic observations, methods are needed, that cancel out or suppress the stellar contribution .

There are two different groups of methods used to separate the stellar from the planetary contribution in the observed signal or to even completely suppress the stellar part. On the one hand there is the rather technical approach using optical systems such as coronagraphs, e.g., combined with pupil-apodization units to cancel the central starlight (see section 4.3.2). The other approach is to use sophisticated differential observing strategies, such as spectral-, angular- and phase-differential observations.

The observations I present in this work are based on a phase-differential method in the sense that I compare the signal of the star/planet-system before and/or after and during an occultation or transit, revealing the contribution of the planet itself (see next section, 1.3.1). The main observational challenge is the low contrast ratio between star and planet, typically of the order of $1 : 10^{-6}$ to 10^{-10} in the optical. However, in the near-infrared (NIR), the situation is much improved: for transiting Hot Jupiters the contrast ratio is of the order 10^{-4} to 10^{-3}. However, given the limited observing time per transit of about 2 hours, and given the fact that these transitions are only observable a few times per year and per observatory (see 2.4.4), only very sensitive spectrometers used at reasonably

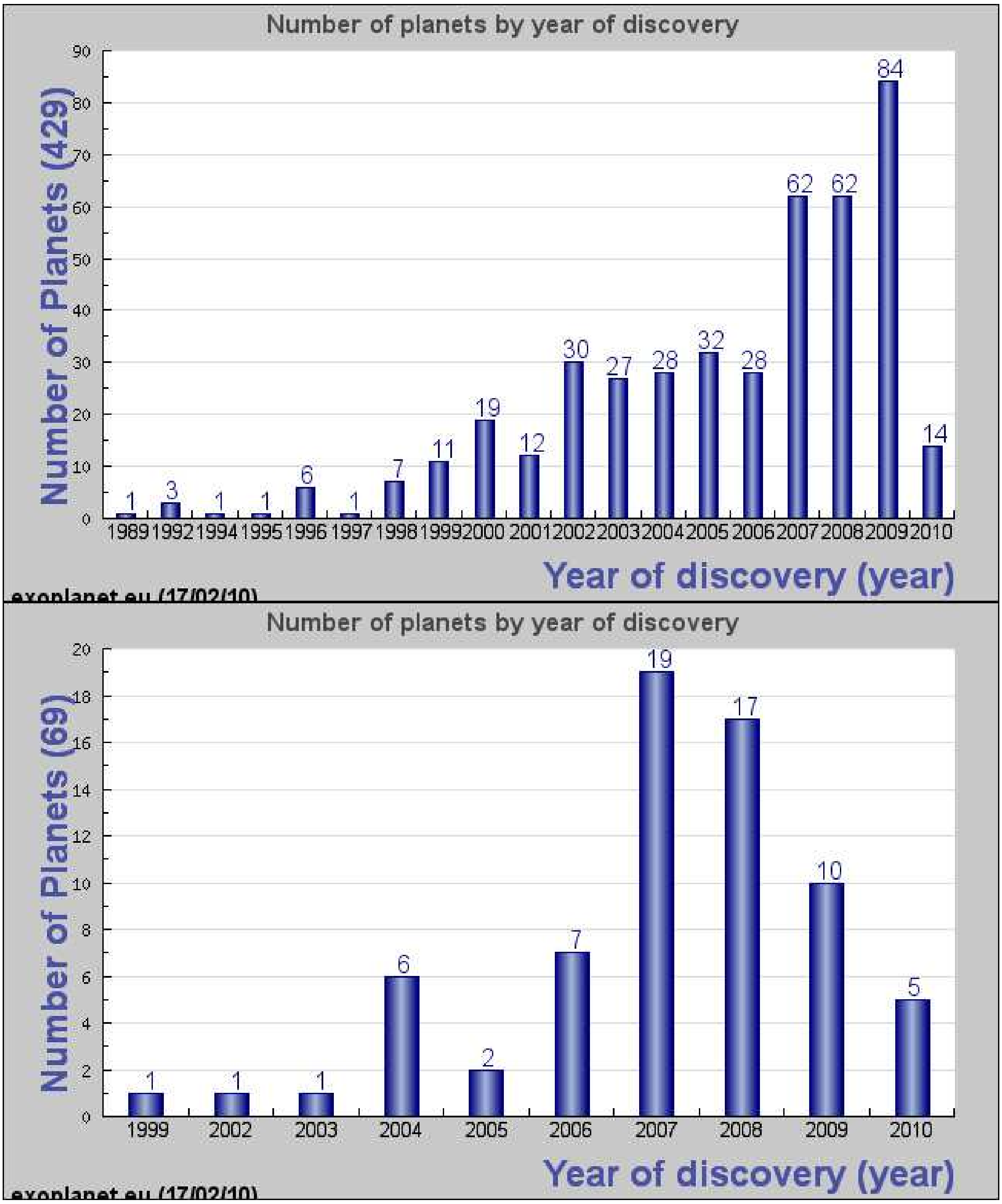

Figure 1.2.: Number of detected extrasolar planets versus year of detection (by Feb. 17th 2010) for all detected planets (top) and transiting planets (bottom). Ground- and space-based surveys such as HAT, CoRoT or the recently launched Kepler-mission will even increase that number, so that in the near future the number of newly detected exoplanets could be dominated by transiting ones (Credits: exoplanet.eu).

large telescopes can achieve a significant signal to noise ratio.

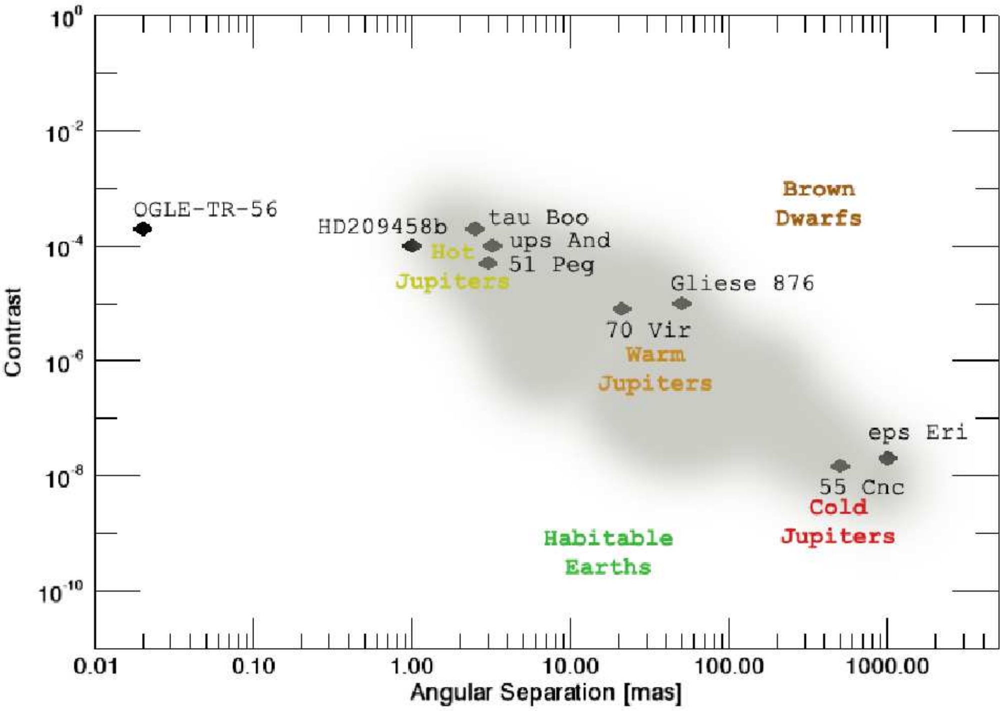

Figure 1.3.: Contrast vs angular separation diagram for extrasolar planets. Most of the known extrasolar planets are located in the grey area. Observations are restricted by the trade off between separation and contrast for those sub-stellar companions.

1.3. Spectroscopy of exoplanetary atmospheres

1.3.1. Optical and infrared transit spectrophotometry

Systems with transiting extrasolar planets mostly offer two important opportunities for observations (see fig. 1.4). In ***primary transit*** the planet occults the star. The broad-band transit-light-curve, in this case, measures the planetary radius R_p in units of the stellar radius R_s. The depth of the occultation is $\sim (R_p/R_s)^2$, which for a Jupiter radius planet transiting a sun-like star, is of the order of $\sim 1\%$ (e.g Henry et al., 2000). At such a signal level, several topics can be addressed. Coupled with Doppler measurements, and few further assumptions, the masses and radii of these planets can be determined. These are the most fundamental of physical parameters, not easily obtained by any other method of exoplanetary observations. Transit timing variations, caused by third bodies in the observed system, can be detected by improved photometric precision.

Spectroscopic observations during the planet's passage, (***transmission spectroscopy***), provides a measure of the upper atmosphere at the planetary terminator at infrared and optical wavelengths and the tenuous thermosphere and exosphere at ultraviolet wavelengths. The transit depth variation with wavelength depends on the atmosphere's scale height and its chemical composition with absorbers selectively attenuating the stellar radiation. Here, the primary observable is the change of the effective planetary radius (i.e. $R_p(\lambda)$) as a function of color due to this selective absorption of starlight along the slant geometry.

Due to the slant optical path, transmission spectroscopy probes relatively high pressure depths in the atmosphere, e.g. $(10^{-2} - 10^{-4}$ bar) at near-infrared wavelengths. Due to the somewhat reduced optical depth due to small scatterers (e.g. molecular hydrogen or aerosols), which can dominate at optical wavelengths (Pont et al., 2008), the near infrared provides an important window for observing atmospheric composition and conditions at the terminator. The dynamical range due to spectral bands (at low spectral resolution, $R \simeq 50$), or the variation in transit depth between two wavelengths channels (e.g. as in the methane signature detected by Swain, Vasisht & Tinneti 2008) is several hundred parts-per-million (ppm) in hot hydrogen dominated gas giants, but smaller (or order 100 parts-per-million) in cooler Neptunes such as the well known nearby system GJ 436b.

The size of a spectroscopic signal during primary transit is proportional to the atmospheric scale height H, defined by:

$$H = \frac{kT}{g\mu} \tag{1.1}$$

where T is the effective temperature, g is the surface gravity, and μ is the mean molecular weight of the atmospheric constituents. If we take the typical hot Jupiter HD 189733b as an example and assume a globally-averaged temperature of 1100 K (Knutson et al., 2009), a surface gravity of 2140 cm/s^2 (Bouchy et al., 2005), and an atmosphere of molecular hydrogen, this would correspond to a scale height of about 190 km or 0.25 percent of the planetary radius.

During ***secondary eclipse*** the planet disappears behind its host star. For a Hot Jupiter, the flux deficit during secondary eclipse (assuming a black-body planet) is only about 300 ppm at about 2 microns in the near infrared, but considerably larger at thermal wavelengths at which Spitzer has observed many of the known transiting planets. However, detectivity is helped by the fact that the planet is not a simple black-body and that in atmospheric opacity windows, one looks at deeper and hotter layers of the atmosphere. Secondary-eclipse ***emission spectroscopy*** provides a direct measure of the planet's disk averaged day-side emission. In the near-infrared, the relevant photosphere of emission lies deep in the atmosphere at pressure-depths ranging between 0.01-1 bar (depending on the exact composition). Deep stratospheres, that are often seen in these hot planets, change the picture with strong emission often observed in the opacity bands.

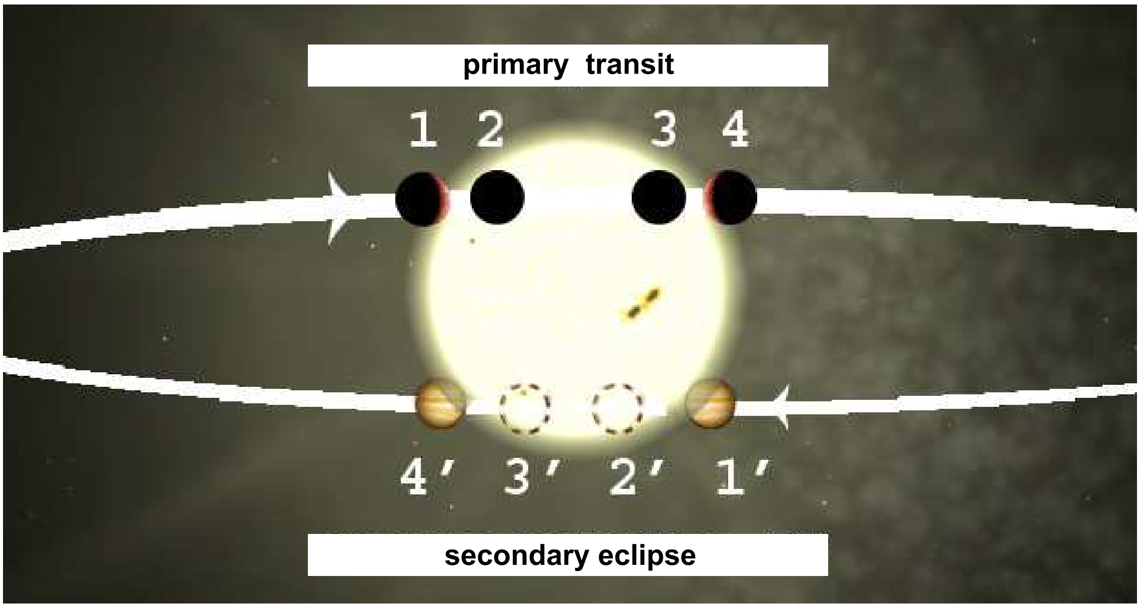

Figure 1.4.: Planetary systems with mutual eclipses of the star and the planet offer two opportunities for transit observations. In primary transit the planet occults the star, while in secondary eclipse the planet disappears behind its host star. During the two important orbital phases, the primary transit and secondary eclipse, distinct parts of the atmosphere may be studied (see text).

1.3.2. Comparative spectroscopy of exoplanet atmospheres

The observable atmosphere of a planet is a window into its composition and provides clues to its formation history. Since the close-in planets are highly irradiated, of major interest is how the stellar insolation affects the atmosphere, i.e. how the irradiation affects the atmospheric structure, its temperature distribution and dynamics, its chemistry, and the planet's cooling and contraction. Equilibrium temperatures of the day-sides of the close-in transiting planets are often very high, $T_{eff} > 1000$ K, making the near infrared an important wavelength region for study. A large fraction of the deposited energy is reradiated in the octave between $1.5 - 3$ μm.

The emission photospheres lie deep in the atmosphere. One expects molecular populations to be in near thermochemical equilibrium due to the associated short chemical timescales. Hence the recent discoveries of deeply-seated disequilibrium species has been a surprise. Many stable molecules (of abundant reactive elements - H, C, N and O) in reducing atmospheres, e.g. H_2O, CO at high T and H_2O, CH_4, NH_3 etc. at lower T, have strong rotational-vibrational transitions in the NIR under these temperature/pressure conditions. Higher in the atmosphere at pressure-depths lower than 0.1 bar it is likely that populations are increasingly affected by disequilibrium processes such as due to the photolytic absorption of the incident high-energy radiation. Given a favorable temperature profile across the relevant emission photosphere, chemical signatures of the exoplanetary atmosphere are strongly imprinted in the emergent spectra.

The principle approach is to use optically active molecules such as atmospheric water, and carbon species such as carbon-dioxide and methane as diagnostic. An example of the power of comparative exoplanetary spectroscopy is shown in figures 1.5 and 1.6, which my collaborators and me already published in Swain et al. 2009b.

I have argued that the near infrared is an important wavelength region for characterization of hot extrasolar planets, not only because a large fraction of the flux is emitted in this region but also because major atmospheric constituents are optically active in these bands. Combining emission spectra (from secondary transit observations) with transmission spectra (from primary transit observations) acquired in the near infrared and optical wavelengths allows the formulation of a fairly advanced physical picture of the exo-atmosphere's properties, providing clues about the atmospheric composition, the prevalent chemistry and possibly the history of formation and evolution.

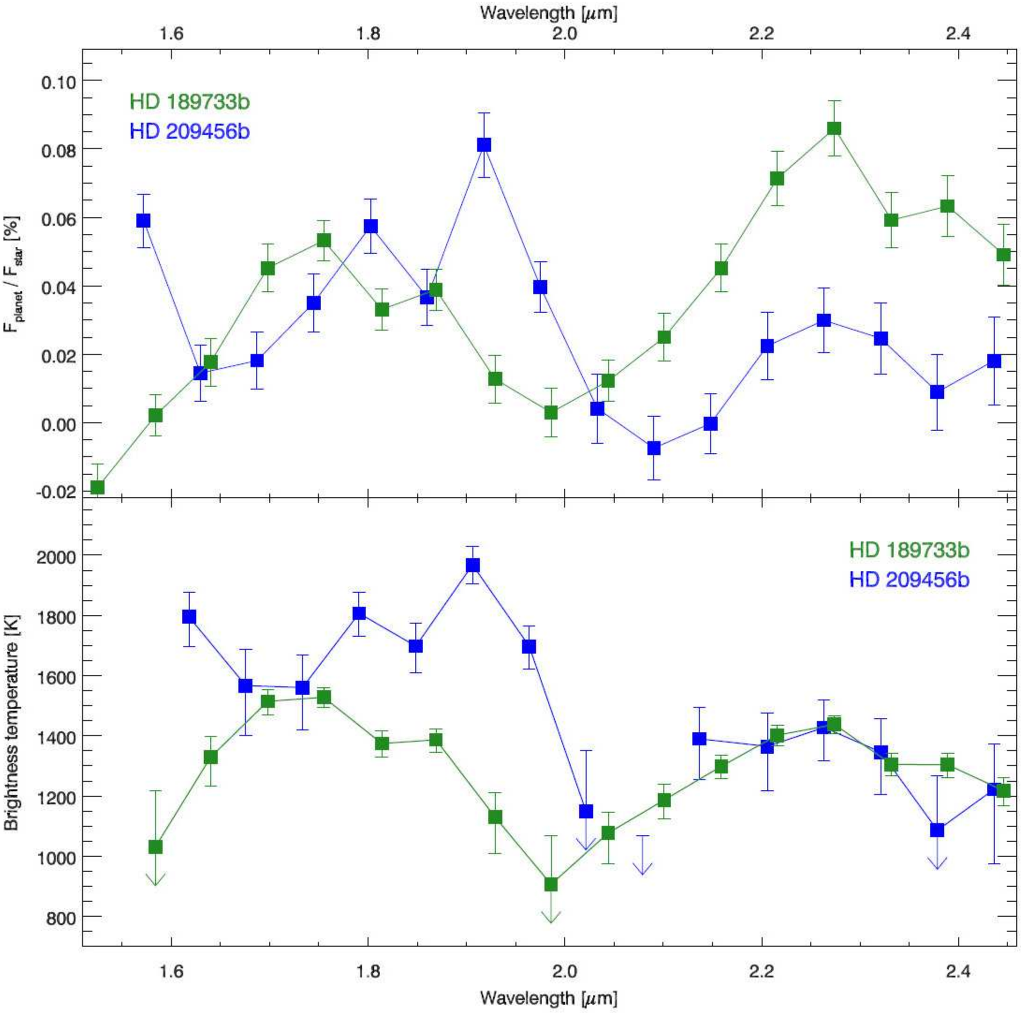

Figure 1.5.: Example for comparative spectroscopy of exoplanet atmospheres with the HST-NICMOS instrument (reproduced from our publication, Swain et al. 2009b). Top: The near-infrared day-side emission spectra of HD 189733b and HD 209458b, showing the significant differences in the nature of the spectra. Bottom: The brightness temperature spectrum of HD 189733b and HD 209458b. The spectra probe similar pressure scales in the day-side atmosphere. The difference in these spectra are primarily due to (1) the presence of significant CH_4 enhancement, and (2) increased temperature in HD 209458b relative to HD 189733b.

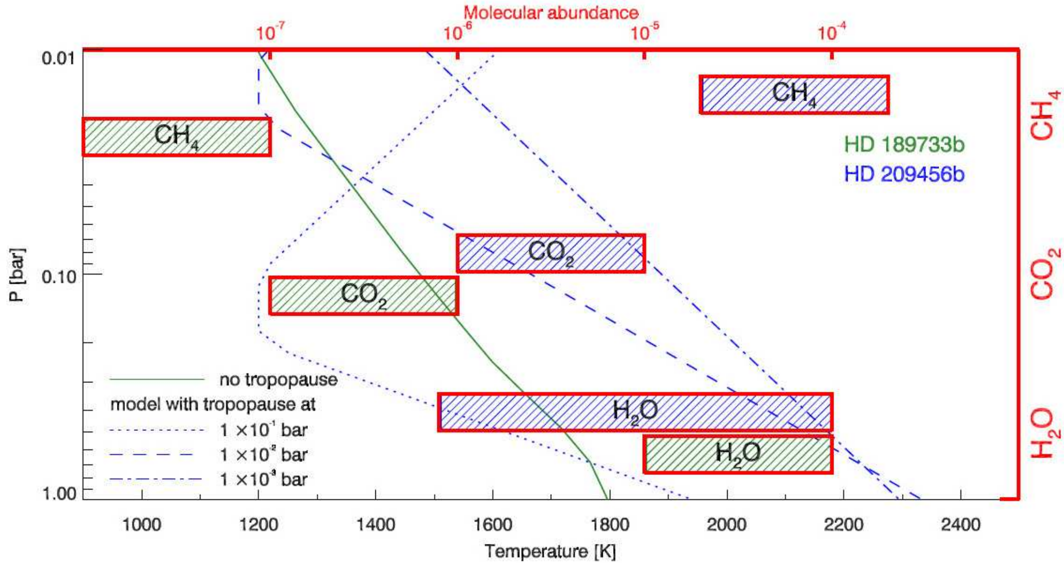

Figure 1.6.: A preliminary comparison of HD 189733b and HD 209458b in terms of the temperature and molecular abundances. The lines show possible temperature-pressure profiles (see legend), the boxes mark the molecular abundances (see top axis) for the different species. There is a suggestion of enhancement in the abundance of CH_4 and H_2O in HD 209458b relative to HD 189733b (reproduced from our publication, Swain et al. 2009b).

1.4. Strategic considerations

The exploration of exoplanets is a key area of scientific investigations within today's astrophysics. NASA's great observatories, the Hubble and Spitzer space telescopes, have made landmark observations of hot, Jupiter-like planets orbiting other stars. These telescopes have detected atmospheric constituents such as methane and water in exo-atmospheres – the same molecules that might serve as tracers of life if discovered around smaller, rocky planets in the future (the discovery of methane on Mars is a case in point).

However, Spitzer meanwhile warmed up, is left only with reduced capabilities and no spectroscopic mode and the future role of HST's infrared capabilities is uncertain. The next few years will see the expansion of observable extrasolar planets using ground-based discovery methods as well as the brightest targets from Kepler and CoRoT (see fig. 5.1).

While space-based platforms deliver stable measurements, they have certain limitations; for example, limitations to aperture and/or a limited set of instrumentation. For example, space-based moderate-resolution infrared spectroscopy (R $\geq$ 1000) will not be available until the launch of the James Webb Space Telescope (JWST). Large ground-based telescopes can provide the next set of breakthrough measurements, i.e., moderate to high resolution spectra of transiting planets in the near infrared atmospheric bands.

1.5. Outline

Motivated by to these strategic considerations, this thesis focusses on issues connected with ground-, space-based as well as airborne-based approaches for spectroscopic characterization of extrasolar planets. This work presents observations from space- and ground-based observatories and gives an outlook to future possibilities for airborne observations.

Chapter 2 of this thesis describes my research in the field of ground-based transit spectroscopy, which is only now showing early results. The main goal is to improve their efficiency in observing transiting planets. I am presenting a study mainly using the integral field spectrograph SINFONI at the VLT on the Hot Jupiter planets HD 189733b and HD 209458b.

In chapter 3 I analyze a space-based HST-NICMOS primary transit data set of the Hot Neptune planet GJ436b using methods that I have developed to accommodate data-sets of moderate photometric quality.

In chapter 4 I develop an exoplanetary science case for the Stratospheric Observatory for Infrared Astronomy (SOFIA) with the hope of implementing some of these ideas during early operations of this airborne observatory.

Lastly, I will present a synopsis of results and an outline of future perspectives.

In the Appendices some theoretical background is presented.

2. Ground-based: Transit Spectroscopy using the SINFONI Instrument

In the last chapter I presented an introduction to the science of spectroscopy of exoplanetary atmospheres. I have argued that the near infrared is an important wavelength region and emphasized the importance for ground-based observations in this field. In this chapter I will present an exploratory study to use adaptive optics assisted near-infrared integral field spectroscopy to observe extrasolar planets from ground-based telescopes. First I briefly describe the general problems of ground-based observations, give an introduction to adaptive optics-assisted integral field spectrographs, using the example of the SINFONI instrument, and demonstrate how it compares with other spectroscopic techniques currently applied. After that I present the observations and the basic data reduction pipeline. Central part of this chapter will be the illustration of 3 different methods, used to analyze the spectral time-series. Finally conclusions and results will be discussed.

2.1. Observational hurdles in ground-based astronomy

Ground-based observations are limited by three main factors: atmospheric transmission, background emission and atmospheric turbulence.

Figure 2.1 shows the atmospheric transmission in the NIR. Changes in the concentration of atmospheric trace gases and therefore changes in atmospheric transmission are one of the biggest issues in time-resolved ground-based spectroscopy. In ground-based exoplanet spectroscopy, there is considerable likelihood of confusion between telluric features and spectral features of the targeted object. The traditional method of observing telluric standards is problematic because of airmass error, possible features in the standard star, and due to short-timescale variability of absorbing species e.g. differences in water vapor content etc. These effects can lead to systematic photometric errors of up to a percent in corrected lightcurves in the vicinity of the strongest H_2O features and somewhat smaller errors around weaker features of telluric CH_4, thus limiting the signal-to-noise achievable in differential spectrophotometry from the ground.

Besides the absorption of telluric features, the emission of the sky background affects the signal. In H- and K- band the main contributor are OH-emission (below 2.2 micron) and the black-body emission of sky and telescopes optics. The background contribution is usually cancelled out by substraction of 'sky-frames' (see 2.4.4 and A.3), their contribution to the noise, however, persists.

Turbulence in the Earth's atmosphere cause astronomical seeing, the blurring and twinkling of astronomical objects. While big telescopes theoretically provide milli-arcsecond (mas) resolution, the real image will never be sharper than the average seeing effects during the observation. Adaptive optics and imaging spectroscopy help to overcome and reduce the consequential seeing (see 2.2). For example, an 8-10 m telescope like the VLT or Keck has a diffraction limit of 30-60 mas resolution at infrared wavelengths, while the seeing limited resolution without any correction is of the order of 1 arcsecond.

Another noteworthy task, that has to be executed when observing planetary transits, in particular when observing from the ground, is the exact timing of these event. Exact timing is critical since the observation time during the transit phase is limited to ~ 2 hours for close in Hot Jupiter class planets. The exact times of the secondary transit and its duration were still uncertain at the time of my first transit observation of HD 209458b. I assessed them from the times of primary transit, which had been determined quite frequently, from the best determination of the orbital eccentricity and from the longitude of periastron. In A.1 I describe the used calculations. My newer observations were made on targets already observed in secondary eclipse so that the calculations presented in A.1 were not necessary. However, for newly detected transiting planets, those calculations have to be executed for first time observations of a sec-

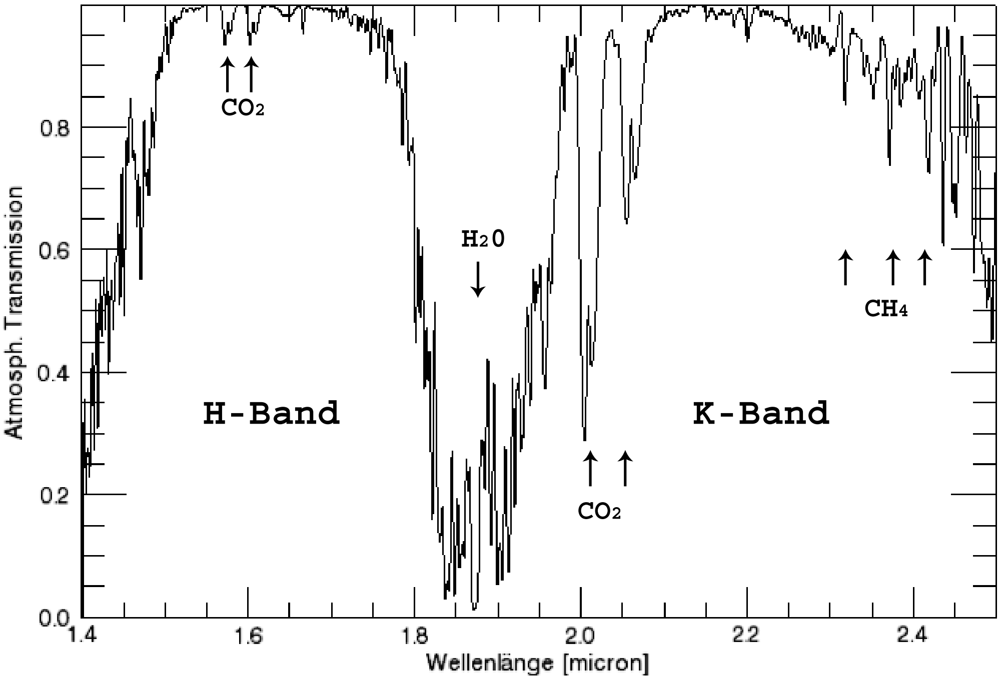

Figure 2.1.: Atmospheric transmission in H- and K-Band at the ESO-Paranal site. Absorption such as the water-band between the band or single molecular lines of carbon-dioxide or methane are serious noise sources for ground-based observations. Produced with ATRAN (Lord 1992).

ondary eclipse.

2.2. Adaptive optics assisted imaging spectroscopy with SINFONI

2.2.1. Adaptive optics

Adaptive optics (AO) is a technique used to improve the performance of optical systems by reducing the effects of high frequency atmospheric distortion, the seeing. Active optics, in turn, works on longer timescales and often uses the primary mirror for pure geometric correction.

Adaptive optics works by measuring the deformations in the wavefront and by correcting for them with a spatial phase modulator such as for example a deformable mirror.

A so called wavefront sensor is used as a device to observe the changes of an electromagnetic wavefront. A typical example is the Shack-Hartmann wavefront sensor. It consists of an array of lenslets of the same focal length. Each is focused onto a CCD array . The local tilt of the wavefront across each lenslet can then be approximated from the position of the focal spot on CCD. Any phase aberration can be calculated to a set of discrete tilts. By sampling an array of lenslets all of these tilts can be measured and the whole wavefront can be reconstructed to some accuracy.

The simplest form of wavefront control in adaptive optics is called tip-tilt correction. Tip-tilt compensates the tilts of the position offsets for the image in two dimensions. This is realized using a fast moving tip-tilt mirror which performs small rotations around two of its axes.

Nowadays, a common technique is to use (segmented or continuous) deformable mirrors (DM). The shape of the DM can be controlled with actuators at a speed that is appropriate for compensation of dynamic aberrations present in the optical system.

To perform the adaptive optics image correction the wavefront sensor measures the distortions the atmosphere has introduced on the timescale of a few milliseconds; the computer calculates the optimal mirror shape to correct the distortions and the surface of the deformable mirror is reshaped accordingly.

2.2.2. Integral field spectroscopy

Integral field spectrographs (IFS) or imaging spectrographs are instruments that are used to observe spectra of astronomical objects across a two-dimensional field-of-view. For all of the different techniques used (see below), the final product usually is a data-cube, with two spatial axes and one wavelength axis (see fig. 2.2, 2.3 and 2.6). Most of the latest IFS instruments are optimized for use in the optical-red and near-IR. An integral field spectrograph consists of two components: the spectrograph and an integral field unit (IFU). The job of the IFU is to divide the 2D spatial plane into a continuous array of pixels. This division can be achieved in three ways as described below and illustrated in the figure following (Westmoquette et al., 2009):

- **Lenslet array:** The input image is split up by a micro-lens array (MLA). Light from each element of the observed object is then concentrated into a small dot and dispersed by the spectrograph. Since the dots are smaller in size than the micro lenses themselves, it is possible to tilt the MLA about the optical axis of the system so that the spectra do not fall on top of each other, thus allowing the input image to be sampled contiguously (differentiating this technique from slit-less spectroscopy). The disadvantage is that the length of spectrum that can be produced without overlapping is very small and the packing of the CCD is not that efficient.

- **Fibres (with or without lenslets):** The input image is formed at the entrance to a 2D bundle of optical fibres which transfer the light to the slit of the spectrograph. The flexibility of the fibres allows the round/rectangular field-of-view to be reformatted into one (or more) "slits", from where the light is directed into spectrograph. In this case the spectra are obtained without wavelength shifts between them. The disadvantages of this techniques are: (a) the sampling of the sky is not contiguous since there are gaps between the fibre cores (fibres are cylindrical) and (b) the fibres do not work efficiently at the slow focal ratios at which most telescopes work resulting in focal ratio degradation (FRD). Disadvantage (a) can be overcome by placing an array of contiguous lenslets in front of the fibre bundle in order to focus all the light collected by that lenslet into the fibre (lenslet shapes are usually square or hexagonal and thus can be packed contiguously).

- **Image-slicer:** The input image is formed on a mirror that is segmented in thin horizontal sections, sending each ’slice’ in a slightly different direction. A second segmented mirror is arranged to reformat the slices so that, instead of being above each other they are now laid out end to end to form the slit of the spectrograph (see fig. 2.4). The advantage of this technique is that FRD is avoided and the slicing arrangement gives contiguous coverage of the field at potentially high spatial resolution. Because this system uses only mirrors, it is especially suitable for the infrared since it is inherently achromatic and can be cooled to cryogenic temperatures. Potential disadvantages are: (a) that the sampling along the slices is the same as that provided naturally by the telescope meaning there is reduced scope to include a slicer within a spectrograph that must also have a normal long-slit mode and (b) the optical system might be bulky and difficult to fabricate.

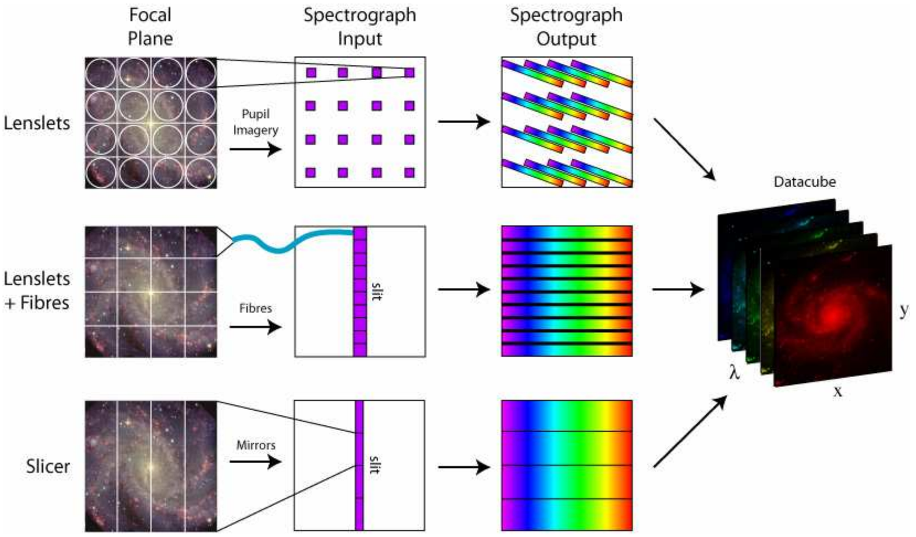

Figure 2.2.: The main techniques for achieving integral field spectroscopy. *Credit: M. Westmoquette, adapted from Allington-Smith et al. 1998*

2.2.3. The SINFONI instrument

SINFONI is a near-infrared ($1.1 - 2.45\mu$ m) integral field spectrograph fed by an adaptive optics module. The spectrograph operates with 4 gratings (J, H, K, H+K) providing a spectral resolution around 2000, 3000, 4000 in J, H, K, respectively, and 1500 in H+K. Each wavelength band fitting fully on the 2048 pixels of the Hawaii 2RG (2kx2k) detector in the dispersion direction. The SINFONI field of view on the sky is sliced into 32 slices. The pre-slit optics allows to chose the width of the slices. The choices are 250 mas, 100 mas and 25 mas, leading to field of views on the sky of 8”x8”, 3”x3”, or 0.8”x0.8” respectively. Each one of the 32 slitlets is

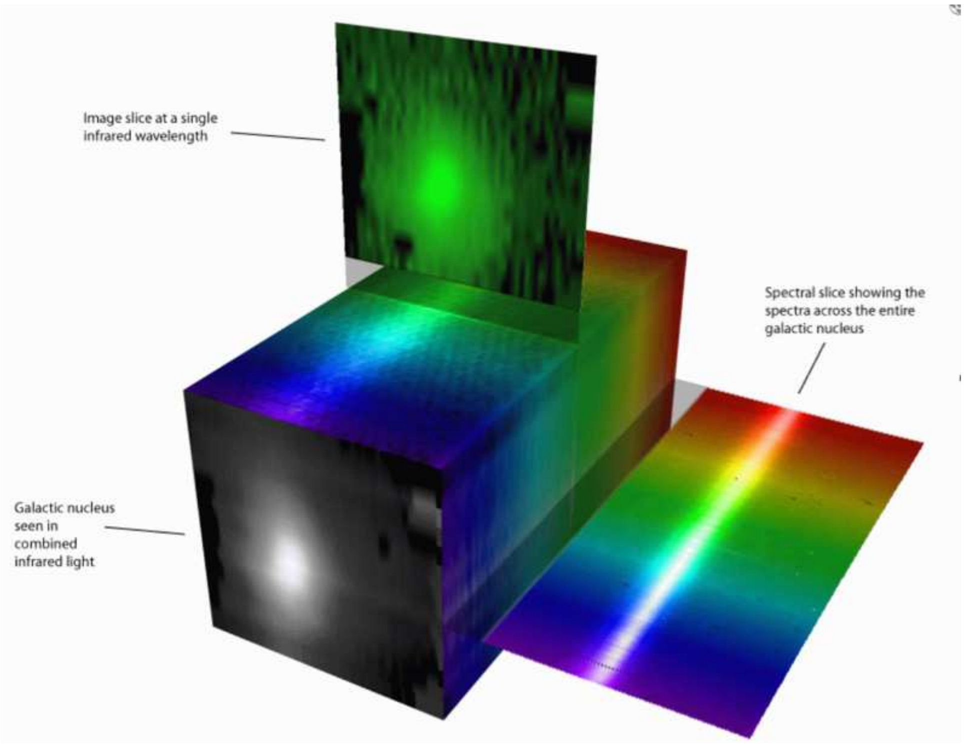

Figure 2.3.: The concept of a data cube. *Credit: Stephen Todd (ROE) and Douglas Pierce-Price (JAC)*

imaged onto 64 pixels of the detector. Thus one obtains 32x64 spectra of the imaged region on the sky (for some more details see B.1.2 and B.1.3).

SINFONI can be used without adaptive optics guide stars, in which case the AO module just acts as relay optics and the spatial resolution is dictated by the natural seeing. The full power of the instrument is, of cause, achieved when an adaptive optics guide star is available. For best correction, the star should be brighter then $\sim$ 11 mag. However, the AO can work (and will provide moderate image quality improvement) with stars as faint as R $\sim$ 17 mag in the best seeing conditions. Ideally, the AO guide star should be as close as possible to the scientific target (if not the science target itself), and usually closer than 10”. Depending on the atmospheric conditions (atmospheric coherence length) the AO guide star could be chosen as far as 30” for the AO system to still provide a mild improvement of the encircled energy.

SINFONI is built from two components - the SINFONI AO module and the SPIFFI infrared integral field spectrograph: The SINFONI Adaptive Optics Module is based on a 60-element curvature system, similar to the

Multi Application Curvature Adaptive Optics devices (MACAO), developed by the ESO Adaptive Optics Department and of which three have already been installed at the VLT.

Provided a sufficiently bright guide star is available within 60 arcsec of the observed field, the SINFONI AO module will ultimately offer diffraction-limited images (resolution 0.050 arcsec) at a wavelength of 2 μ m. At the center of the field, partial correction can be performed with guide stars as faint as magnitude 17.5.

SPIFFI is a fully cryogenic near-infrared integral field spectrograph allowing observers to obtain simultaneously spectra of 2048 pixels within a 64 x 32 pixel field-of-view. In conjunction with the AO Module, it performs spectroscopy with slit-width sampling at the diffraction limit of an 8-m class telescope. For observations of very faint, extended celestial objects, the spatial resolution can be degraded so that both sensitivity and field-of-view are increased (Thatte et al., 1998; Bonnet et al., 2003; Eisenhauer et al., 2003).

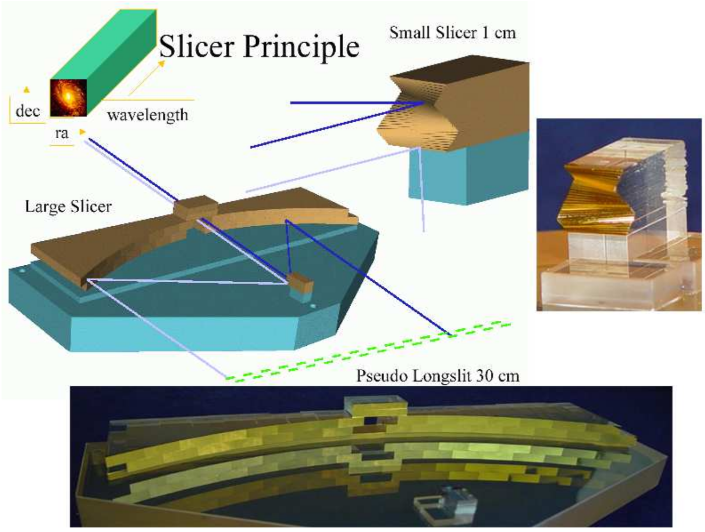

Figure 2.4.: Principle of the SINFONI/SPIFFI image slicing (Credits: eso.org).

Figure 2.5.: SINFONI mounted at the VLT (Credits: eso.org).

2.3. Advantages of integral field units for transit observations

The advantages of adaptive optics (AO) assisted diffraction limited imaging spectroscopy in the field of extrasolar planet characterization is very well discussed in the literature (Sparks & Ford 2002, Arribas et al. 2006, Angerhausen 2006).

Thanks to the 2d to 1d conversion done by an image slicer (or by a fiber bundle), the star light is spread along two directions. This technique allows to use a larger area of the detector, boosting the limit imposed by the photon-noise per exposure. By distributing the star light along the dispersion direction it is possible to increase the total number of photons collected before the detector reaches the saturation limit. This enhances the duty cycle of the instrument (i.e. total number of photons by unit of available time, including overheads), which translates to an increase in the S/N when the photon noise is the major source of noise. It also has the beneficial effect of averaging out flat field and sensitivity residuals. The ability to distribute the light over the whole detector is particularly relevant with the advent (and prospects) of very large telescopes that collect correspondingly large numbers of photons. This is a major advantage

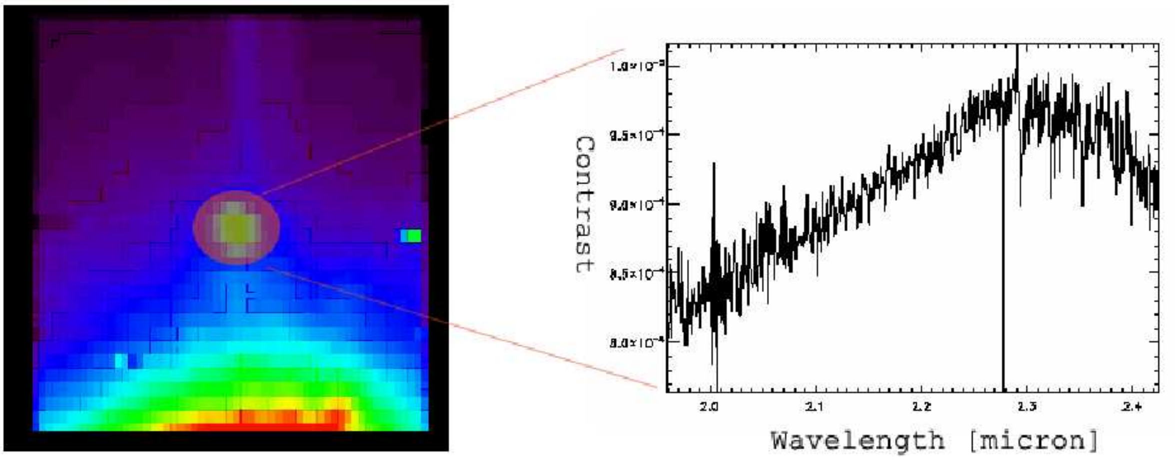

Figure 2.6.: Example of a SINFONI observation of the sub-stellar companion GQ Lup b (Angerhausen et al., 2006; data taken from ESO Archive). Left: Wavelength-collapsed image of star (bottom) and companion (center). Right: extracted spectrum of companion. Imaging spectroscopy offers the opportunity to extract a spectrum of every pixel in the 2D-field of view.

especially with regard to the usually very bright exoplanet host-stars.

Note that to optimize the use of the detector, the image of the star at the focal plane should be well over-sampled by the Integral Field Unit (IFU). Since for these transit observations we are interested in the total number of photons recorded in a limited period of time (i.e. duration of the transit), the image at the input of IFU could be de-focused (see 2.4.4). Note that de-focussing the star image on the IFU does not modify the spectral resolution of the observations, which is another practical advantage of the IFS method with respect to previously used spectroscopic methods.

Apart from the ability to gather photons, stability is crucial for exoplanetary transit observations. The unstable nature of the Earth atmosphere makes very accurate ground observations particularly challenging. In any case, when uncontrolled instabilities may affect the photometric accuracy of the system, a good record of them may give the possibility to decorrelate the photometric signal (see 2.8). This provides another important advantage of the IFS. Since both, the spectra from which the photometric information is obtained and the images of the object (PSFs) are extracted from the same data cube, it is possible to remove photometric variations induced by PSFs instabilities. Another advantage of IFS for these type of observations is a consequence of the large number of spectra collected simultaneously, which can be used to auto-calibrate the data themselves from detector and background signatures.

Summarizing, IFS provides three main advantages for transiting planets observations: i) improves the ability to collect photons during the transit, enhancing the S/N, ii) it allows to auto-calibrate the data, and iii) by tracking in an independent manner the instabilities produced at the focal plane and those due to the spectrograph, it is possible to remove noise correlated to PSF characteristics (Arribas et al. 2006).

Detailed models of contrast and expected signal to noise ratio (see A.2) show that a subgroup of transiting exoplanets around bright host stars should at least theoretically be observable with near infrared integral field spectroscopy from large ground based telescopes such as SINFONI at the VLT.

2.4. Observations

2.4.1. Target selection

By the time of our observations, the two most promising candidates for the proposed transit observation where HD 209458b and HD 189733b. Their advantage is that they have a reasonable contrast as hot close in Jupiter-sized planets and host stars bright enough get enough signal during the relatively short phases of conjunction.

For example the G0V host star HD 209458 at a distance of 46 parsecs has $m_V = 7.65$ mag. A superior conjunction can be observed about once a week during night time due to the rotation period of 3.525 days. The maximum elevation of HD 209458b at the VLT is about $47°$, limiting the observation to the time around local transit at the observatory. After the first feasibility study in 2005 on HD 209458b it turned out that HD 189733b is a slightly better candidate.

HD 189733b is a nearby hot-Jupiter in a circular orbit of radius 0.0313 AU around a K0V parent (Bakos et al. 2006). The planet's mass and radius are similar to those of Jupiter. The high effective day-side temperature $T_{eff} \simeq 1200$ K, as well as the large area ratio between stellar and planetary projected surfaces R_p^2/R_s^2, make HD 189733b the most accessible target in the sample of known close-in exoplanets. In the meantime, HD 189733b was already observed at $R \simeq 50$ in transmission and in emission at NIR wavelengths using NICMOS (Swain, Vasisht & Tinetti, 20008; Swain et al., 2009). The transmission spectrum, observed in primary transit, is explained primarily by water (present in nominal amounts) and CH_4 at cooler higher altitudes, but provides poor constraints for CO, the anticipated majority carbon carrier molecule on the day-side. In comparison, the emission spectrum, observed in secondary transit, is a disk-averaged view of the hot day-side (0.1-1 bar) - showing modulation by absorption bands of water and CO, and only upper limits for much depleted CH_4 (relative to the terminator). The deep absorption trough around 2.0 microns is explained by absorption via overtone bands of CO_2 (or possibly a mix of CO_2 and H_2S, the major sulphur carrier in these conditions) present in trace concentrations.

Even after first space-based results were achieved, there is significant motivation for observing HD 189733b with ground-based telescopes and instruments in general and SINFONI in particular. Scientifically, usable $R \sim 3000$ spectra would be a major advance as the low spectral resolution NICMOS data make retrieval of molecular species with overlapping bands next to impossible (e.g. as in the case of CO in a gaseous mixture of CO and CH_4). Its gross spectral shape and key atmospheric gases are determined from NICMOS measurements and radiative transfer modelling, and can serve as effective priors for sophisticated ”forward modelling” schemes in disentangling the planetary emission from the intervening telluric absorption at the native SINFONI spectral resolution. Finally, HD 189733b is a relatively bright, easily accessible target from Paranal with strong molecular absorption bands which modulate the contrast to $\sim 10^{-3}$ levels relative to the nominal continuum. Observing the HD 189733b spectrum from the ground is in many ways the most important step forward in ground-based exoplanetary spectroscopy. A proof of concept for this bright target with strong features could open the door to characterization of much fainter targets with weaker molecular features.

2.4.2. HD 209458b on August, 13th, 2005

HD 209458b was observed before and during its secondary eclipse on August, 13th, 2005 during 6 hours of Director’s Discretionary Time (DDT)-

Observation.

Under sub-optimal atmospheric conditions (very variable seeing, clouds passing by) I obtained 38 minutes worth of on target data during pre-secondary eclipse phase and 60 minutes during the secondary eclipse phase as well as the corresponding sky frames for background correction and some telluric standard stars for atmospheric correction. Clouds passed through several times during observation resulting in significant fluctuations of the atmospheric transmission. Due to this fact, correction of atmospheric changes exhibited one of the biggest challenges during data reduction. SINFONI operated in H+K mode where a complete H+K spectra at a spectral resolution of R = 1500 are imaged on the detector. The analysis of this data-set is described in Angerhausen et al. 2006. This first analysis of the potential of ground based imaging spectroscopy was used to optimize our observing strategy.

Here I summarize the results of those observations in order to provide some background on how the observing strategy was optimized over time and several observing run. It is important to understand the observing technique was still under development at that time. To some extend it still is.

HD 209458 - the parent star

Name	HD 209458
Distance	47 pc
Spectral Type	G0 V
Apparent Magnitude V	7.65
Mass	1.01 (± 0.066) M_{sun}
Age	4 (± 2) Gyr
ref. Effective Temperature	5942 K
ref. Radius	1.146 (± 0.059) R_{sun}
ref. Metallicity [Fe/H]	0.04
Right Asc. Coord.	22 03 10
Decl. Coord.	+18 53 04

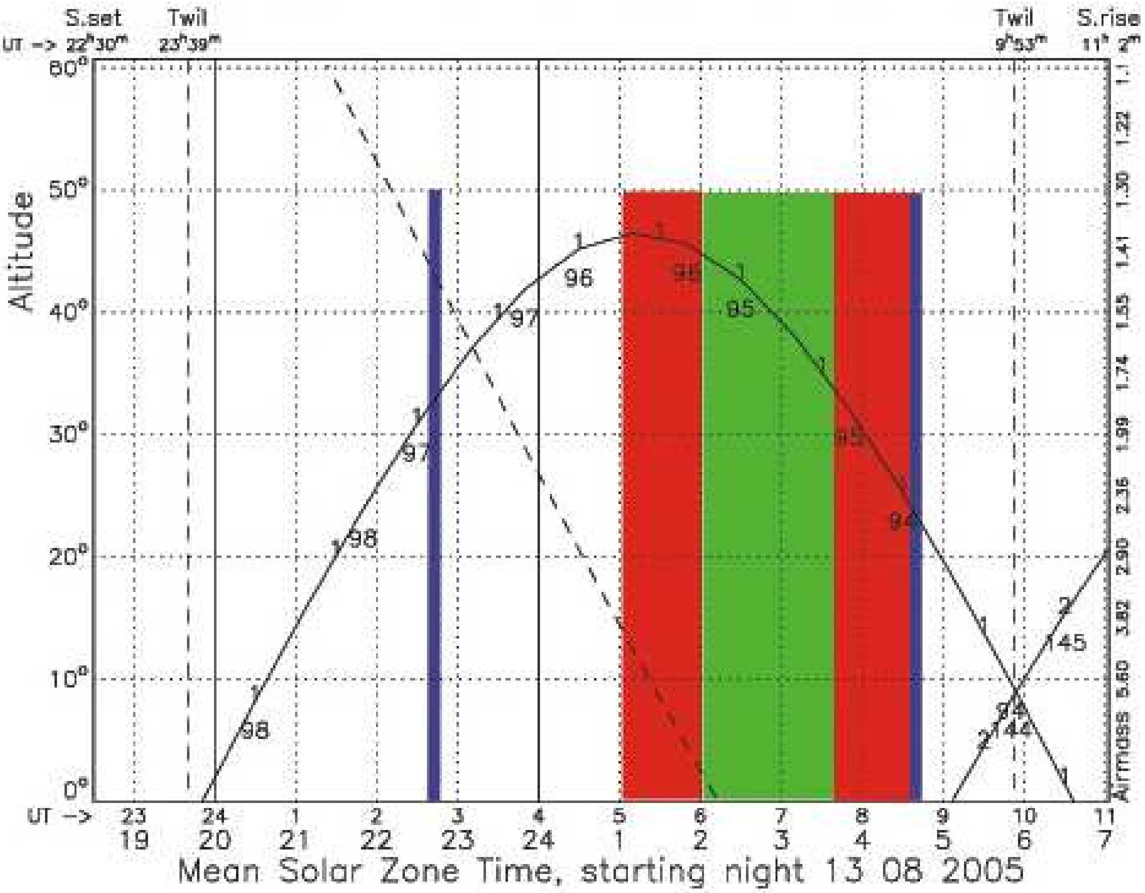

Figure 2.7.: Elevation versus time plot of the observation of HD 209458b on August, 13th, 2005. Blue lines represent start and end of our observation. The green area marks the phase of certain conjunction, red areas represent phases of ingress and egress. 'In' and 'out of' eclipse data can be observed at the same elevation/airmass.

HD 209458b - the planet

Name	HD 209458 b
Discovered in	1999
Mass	0.685 (± 0.014) M_{Jup}
Semi major axis	0.04707 (-0.00047+0.00046) AU
Orbital period	3.52474859 (± 3.8e-07) days
Eccentricity	0.07
ω	83 deg.
Radius	1.32 (±0.025) R_{Jup}
$T_{transit}$	2452826.628521 (± 8.7e-05)
Inclination	86.677 (± 0.06) deg.

2.4.3. HD 189733b on August, 10th, 2007

HD 189733b was observed before, during and after its secondary eclipse on August, 10th, 2007 during one night of visitor mode observation with SINFONI at the VLT.

With very poor atmospheric conditions (clouds passing) in the beginning of the night we obtained 36 minutes worth of on target data before, 53 minutes during and 26 minutes after secondary transit phase as well as the corresponding sky frames for background correction and some telluric standard stars for atmospheric correction, observed during egress and ingress phase.

SINFONI operated in K mode where a complete K spectrum at a spectral resolution of R = 3500 is imaged on the detector. The target was kept on the same position on the detector for all observations.

HD 189733 - the parent star

Name	HD 189733
Distance	19.3 (± 0.2) pc
Spectral Type	K1-K2
Apparent Magnitude V	7.67
Mass	0.8 (± 0.4) M_{sun}
Age	> 0.6 Gyr
Effective Temperature	4980 (± 200) K
Radius	0.788 (± 0.051) R_{sun}
Metallicity [Fe/H]	-0.03 (± 0.04)
Right Asc. Coord.	20 00 43
Decl. Coord.	+22 42 39

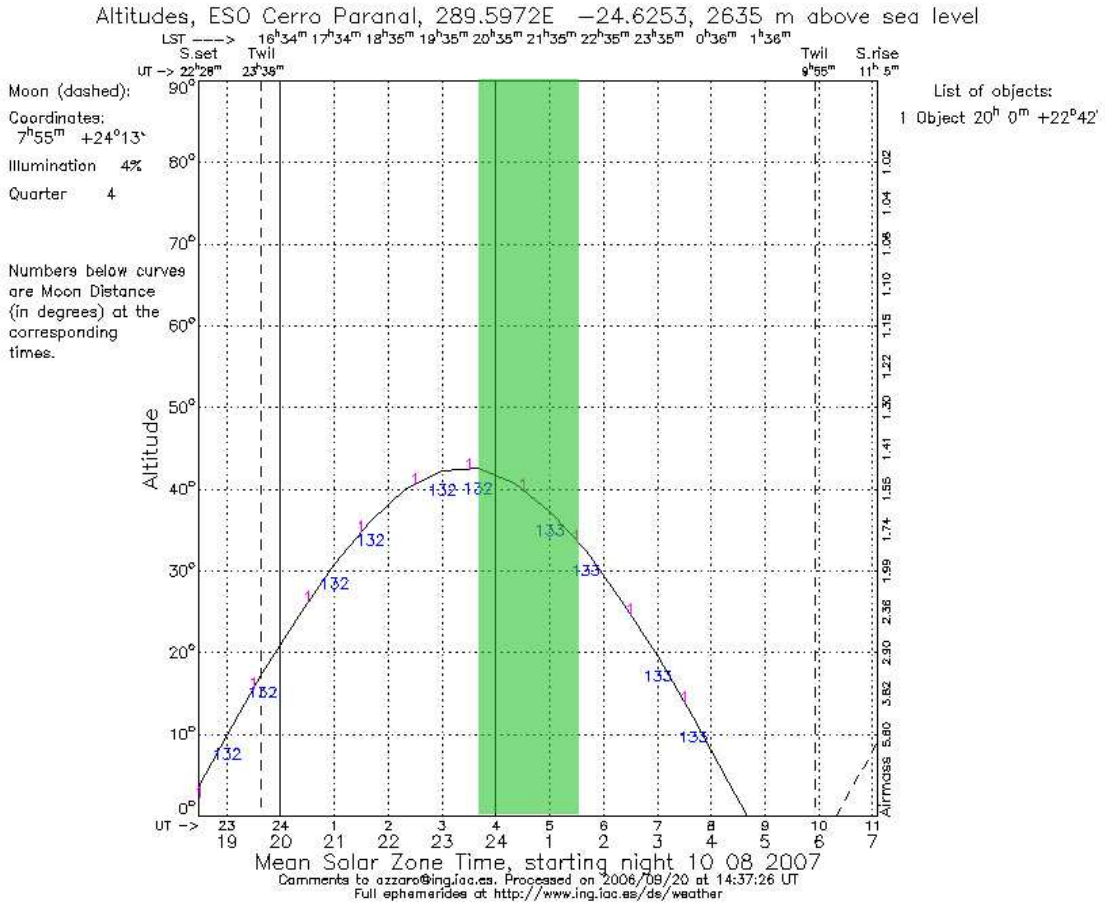

Figure 2.8.: Elevation versus time plot of the observation of HD 189733b on August, 10th, 2007. The green area marks the phase of certain conjunction. 'In' and 'out of' eclipse data can be observed at the same elevation/airmass.

HD 189733b - the planet

Name	HD 189733 b
Discovered in	2005
Mass	1.13 (± 0.03) M_{Jup}
Semi major axis	0.03099 (± 0.0006) AU
Orbital period	2.2185733 (± 0.00002) days
Eccentricity	0
Radius	1.138 (± 0.027) R_{Jup}
$T_{transit}$	2453988.80336 (±0.00024)
Inclination	85.76 (± 0.29) deg.

2.4.4. Calibration strategy

Optimization of the observing efficiency requires real time decisions regarding several parameters: i) The detector single integration time (DIT), since nonlinearity and saturation have strictly to be avoided, ii) Nodding frequency has to be matched with the DIT, iii) The frequency of sky and calibration star observations will be matched with prevailing weather conditions.

Since the target will be raising or setting or both during the observations, the secondary transit phase relative to the transit still is a free parameter. One possibility is to schedule the transit midpoint synchronized to local culmination of the target. The second is to schedule either ingress or egress in local culmination. Since the goal is to obtain two sets of data ('in' and 'out of' eclipse) under mostly identical atmospheric conditions, there is no intrinsic gain in distributing the observing time symmetrically with respect to transit midpoint. Ideally, local culmination of the host star should occur during egress or ingress. Then the range of zenith distance covered by both observations is mostly identical (see fig. 2.15), thus improving the data quality significantly over, e.g, data-sets with different airmass parameters for the 'in' and 'out of' eclipse data. Depending on the orbital phase of the planet, this synchrony between planetary transit and local culmination of the target can happen rather infrequently. For example, the optimal constellation for observing HD 209458b (as shown in fig. 2.7) in fact occurs only once or twice per year, strongly limiting the observing opportunities.

Due to relatively short transit times the observation of telluric standards during the phase of transit reduces the observing efficiency considerably, so that self-calibrating methods are preferred. Optimizing the observing efficiency with regard to the bright targets and short integration times on IFUs showed that observing in 'defocus' mode is the best choice. Though no defocus mode is available for SINFONI, it is possible to use a pupil viewing mode, that also spreads the signal over a wider part of the detector to early saturation. However, a careful analysis showed that in observing in pupil mode increases the background contribution to a unfavorable level. Therefore the final decision for the SINFONI observation was to observe with normal focus and not in the pupil. At similar observations using the OSIRIS instrument at Keck I actually used the offered defocus mode.

In order to collect as much on target signal as possible, sky frames were only obtained for each dithered pair of on-target frames for the HD209548b observation and for each set of 8 target frames for the HD189733b observation (see A.3, for a detailed analysis of the observing efficiency). Therefore, for each data frame the appropriate sky frame was constructed by time stamp sensitive linear interpolation (see 2.5).

The SINFONI setup for the 2005 observation was:

Filter	H+K
Dit	10 sec
Ndit	6
scale	100 mas
No. of frames	79

The SINFONI setup for the 2007 observation was :

Filter	K
Dit	20 sec
Ndit	5
scale	25 mas
No. of frames	70

2.5. Basic data reduction: standard pipeline

The basic data reduction from the raw science frames (fig. 3.2, left) to the final data-cubes was conducted using the standard ESO-SINFONI data reduction pipeline (for details see: ESO-SINFONI user manual and B.1.1) augmented by some special customizations according to our goal to achieve a stable high (relative) signal to noise. The data reduction pipeline is explained in detail in (Angerhausen et al., 2006). Here I present a brief summary.

- **Calibration files.** Each observational setup (filter, scale etc.) of SINFONI comes with a particular set of calibration frames. For an integral field unit (IFU) like SINFONI this set is larger and contains some more specialized exposures than for e.g. slit spectroscopic or ordinary imaging observations. These calibration frames are used to correct for detector specific features (such as for example bad pixels) or to calibrate and reconstruct the 3d data cubes from the original 2d raw frames (such as for example the wavelength calibration). Figure 2.10 shows examples of the various calibration frames used in the SINFONI data reduction pipeline (DRP).

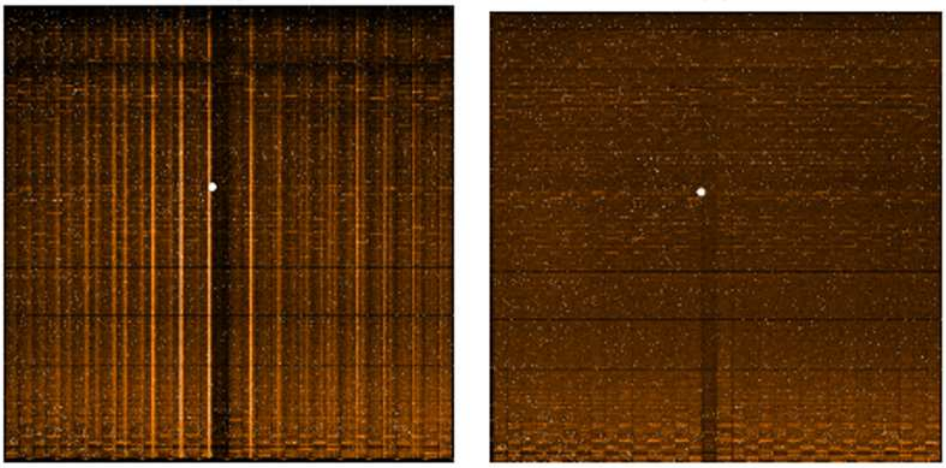

Figure 2.9.: The SINFONI science frames: example for a **science frame** (left, with an object in the FOV) and a **sky frame** (right, only background in the FOV, used for later substraction). The dot in the middle is a 'volcano', a cluster of bad pixels. Note the vertical lines in the science frame caused by the science target and the horizontal lines in each slitlet caused by atmospheric OH-emission.

- **Bad pixel correction.** It is possible to extract or directly discover bad pixels using a set of dark exposures, that were taken by reading out the unilluminated detector after various times between 3 and 500 seconds. So called non-linear pixel are identified by analysis of a set of flatfield exposures, that were taken by reading out the detector after different times of constant uniform illumination of a flat featureless source (usually a lamp, emitting a black-body spectrum of its temperature or exposures of the telescope dome). Those identified bad pixels from both procedures were put together in a global

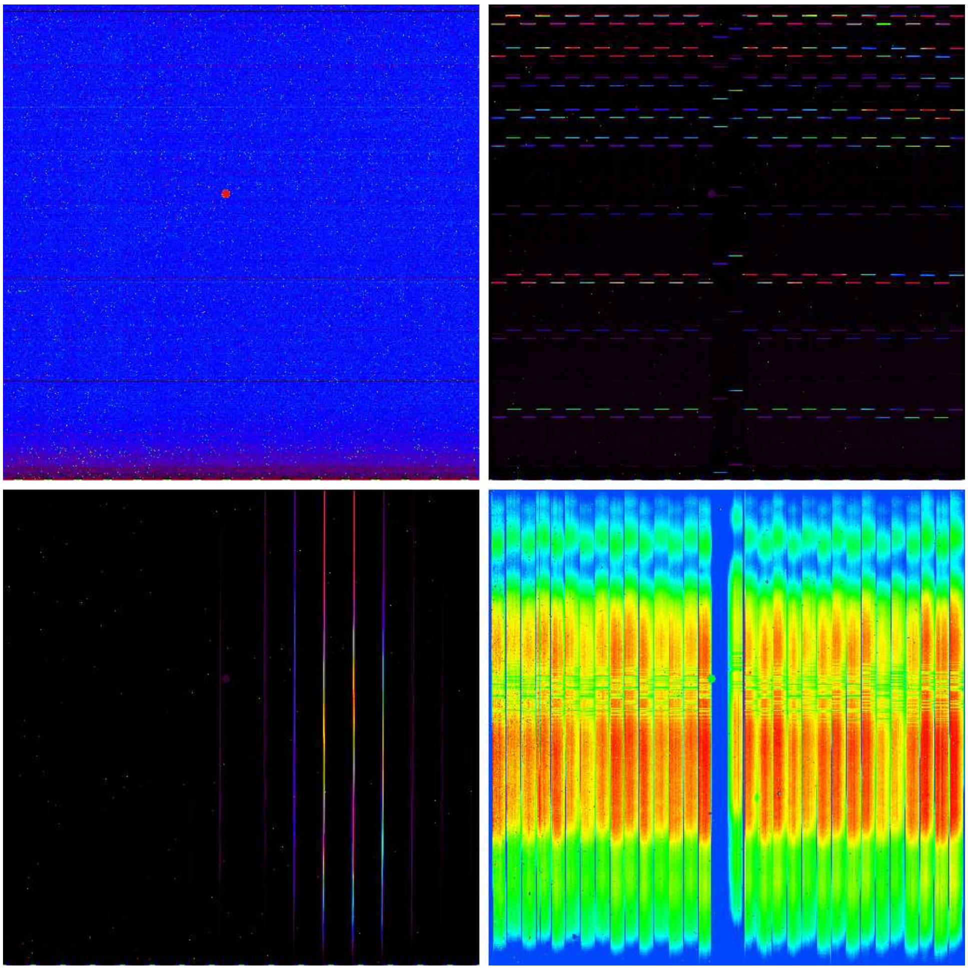

Figure 2.10.: The SINFONI calibration frames: example for a **dark frame** (top left), a **wavelength calibration frame** (top right) a **distortion frame** (bottom left) and a **flatfield exposure** (bottom right). See text for details on their acquisition and use.

bad pixel mask, that was used for all exposures of that particular observation night.

Quality of the bad pixel map is important for the quality of the end products. Especially the wavelength calibration and distortion determination are sensitive to the level of the bad pixel recognition. Due to our special need of high S/N and to detect possible impacts of cosmic rays in the detector that cause clusters of overexposed pixels, a dedicated algorithm was developed, to sort out pixels that vary too much from other pixels within a predefined surrounding area. This individual bad pixel mask for each exposure was added to the master bad pixel mask to obtain an individual mask for each exposure of our observation.

- **Wavelength calibration.** We used set of wavelength calibration frames, in order to define the wavelength position of each pixel on the 2d frame in the latter 3d data cube. Those calibration frames (’arc-lamp frames’) are exposures of noble-gas-lamp (neon+argon in K-band, xenon+argon in H, xenon in H+K and argon in J) that emit only specific atomic lines. Comparing the line list of the particular species with the peaks in the wavelength calibration exposures sets the wavelength position of the pixels.

  Positions of the slitlet edges for each spectral band and pre-optics were also determined from a spectral arc lamp frame.

- **Distortion correction.** Distortion correction was performed using a set of so called ’fiber frames’ obtained by placing a fiber at different positions on the image slicer (’north-south test’). They are used to determine the detector’s geometric distortions and the slitlet distances for each spectral band (see fig. 2.11). Products are:

  distortion coefficients: A table containing the coefficients for distortion correction. Geometric distortion depends on the spectral band used and is corrected for in stacked frames in north-south tests, wavelength calibrations and science data reduction.

  slitlet distances list: A table describing the distances from one slitlet edge to another. Pixel distances of the slitlets depend on which spectral band is used. These distances are used in cube reconstruction. Slitlet distances should remain constant unless the instrumental setup is changed.

- **Sky interpolation and substraction** At the beginning of this chapter I pointed out the importance of background emission correction. In the appendix (see A.3) I describe how and why we observed sky frames after every 8th object exposure. A sky frame (fig. 3.2,right) must be subtracted from the object frames, since the night-sky emission lines are very bright and vary both spatially and in time in the near-infrared. Therefore the sky frame must be obtained close in

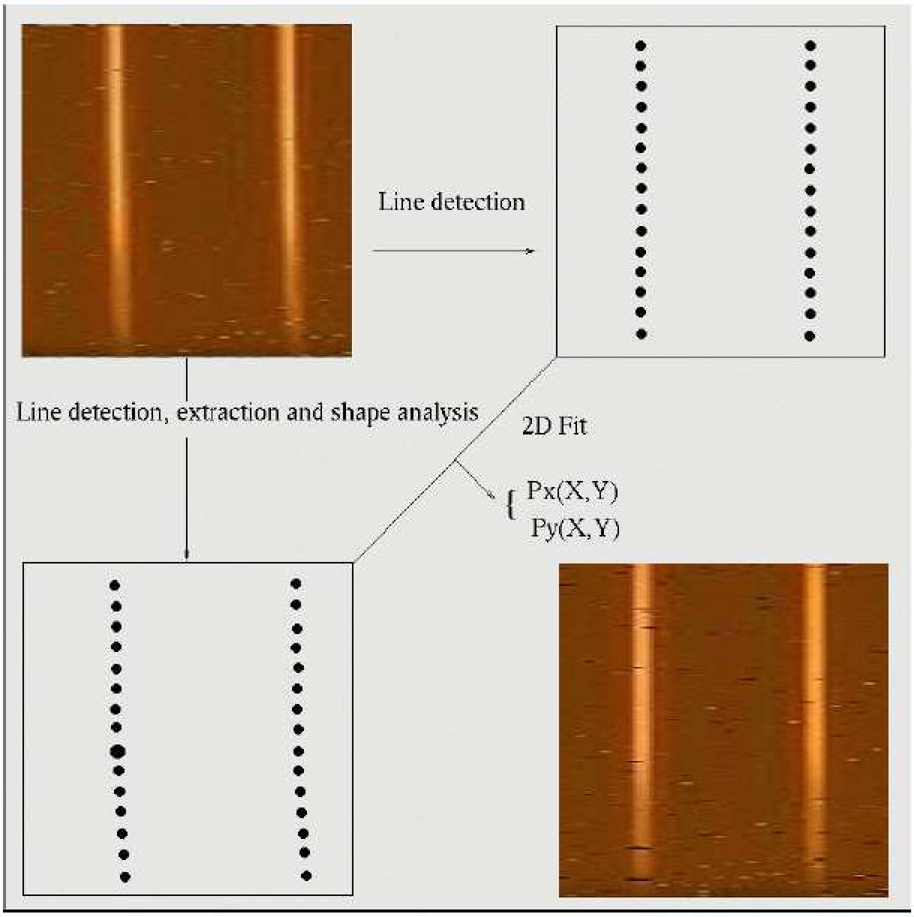

Figure 2.11.: This image describes the concept of the distortion computation algorithm. The spectra of the fibres that were positioned at different positions on the image slicer are traced, two grids on the distorted and undistorted space are built, then a 2D polynomial transformation is performed. This figure displays only two of the 32 slitlets. (from: ESO-SINFONI user manual).

time and angular distance form the science field - otherwise OH line remnants will appear in the final data cube.

The individual background frames S_{X_i} at the time t_{X_i} were calculated from the background exposures slightly before (S_1 at t_1) and after (S_2 at t_2) via (see also fig. 2.12):

$$S_{X_i} = \frac{t_{X_i} - t_1}{t_2 - t_1} * S_1 + (1 - \frac{t_{X_i} - t_1}{t_2 - t_1}) * S_2 \tag{2.1}$$

- **Flatfiedling** Flat field exposures are used to correct for pixel to pixel

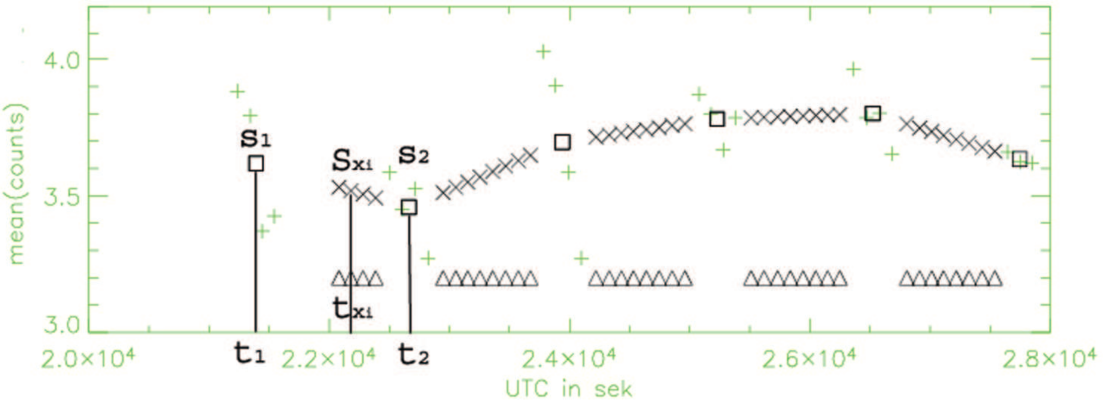

Figure 2.12.: Example for the interpolation of background exposures. The mean flux (y-axis) is plotted against the time of the exposure (x-axis). The individual background frames S_{X_i} at the time t_{X_i} were calculated from the background exposures slightly before (S_1 at t_1) and after (S_2 at t_2) via the formula given in the text.

sensitivity variations. There are various types of at flat field exposures. Standard flat fields, obtained by constant uniform illumination of a flat featureless source are used to generate detector sensitivity maps (master flat fields) and static bad pixel maps (see bad pixel correction). A set of linearity flat fields with increasing intensity (i.e. integration time of the same source) are used to determine and eventually correct for the detector's linearity and generate a bad pixel map for highly non-linear pixels. Flats are also taken together with distortion correction frames as part of the north south test to compute the detector's distortion. Since SINFONI is a Cassegrain instrument, the changing g-vector during observations with changing telescope inclination cause flexures on the detector that change the flatfield behavior. To control that changes we requested special calibration frames, flatfield exposures at different elevations covering the complete elevation range of our observations.

- **Cube reconstruction**

After subtraction of the interpolated background-frame, the frames were divided by flat-field, followed by a procedure to detect bad pixel and cosmic ray impacts on each individual frame. Each frame was then wavelength calibrated and converted into a data cube using

> the standard SINFONI reduction pipeline's reconstruction procedure (see fig. 2.13; B.1.1). For this reduction it was crucial to keep the same (real) detector pixels for all cubes to correct for be able to control shifts and to minimize residual flatfield effects.Therfore the option of automated correction of atmospheric dispersion, included the reduction pipeline, was not used, because it would have re-sampled each cube to different (interpolated) pixel grid.

The steps of the reduction described here do not differ significantly from usual reductions. After the cube reconstruction we obtained a set of 79 data cubes (for HD209458b, 2005) and 70 data cubes (for HD189733b, 2007) of the size 64x64X2048 pixels on which we carried on with the reduction targeting our science case.

Three different methods are used to analyze the data. Method A searches directly for the broadband shape of the planetary spectrum (see fig. 2.14, left) at full instrumental resolution of $R \simeq 3000$. Method B searches for narrow band molecular spectral features in the planetary atmosphere (see fig. 2.14, right) respectively. These two methods were already described in my diploma thesis (Angerhausen, 2006) and other publications (Angerhausen, 2007, 2009) and are here described just in brief. Method C represents a integrated approach to use time-series analysis to compute a broad-band spectrum at lowered spectral resolution of $R \simeq 30$ using a self-coherent Fourier-method.

2.6. Method A: Broad-band analysis at full spectral resolution

2.6.1. Motivation

The basic idea to obtain the broadband spectrum of the planet from our data-set was to compare pairs of 'in' and 'out of' eclipse spectra observed at the same airmass. Therefore observation nights were chosen, that provided local zenith at either egress or ingress so that the phases 'in' and 'out of' transit could be observed at same elevation ranges (see fig. 2.15). Averaging those spectra leads to a final broadband spectrum, that is independent of 1st order systematic effects due to airmass differences.

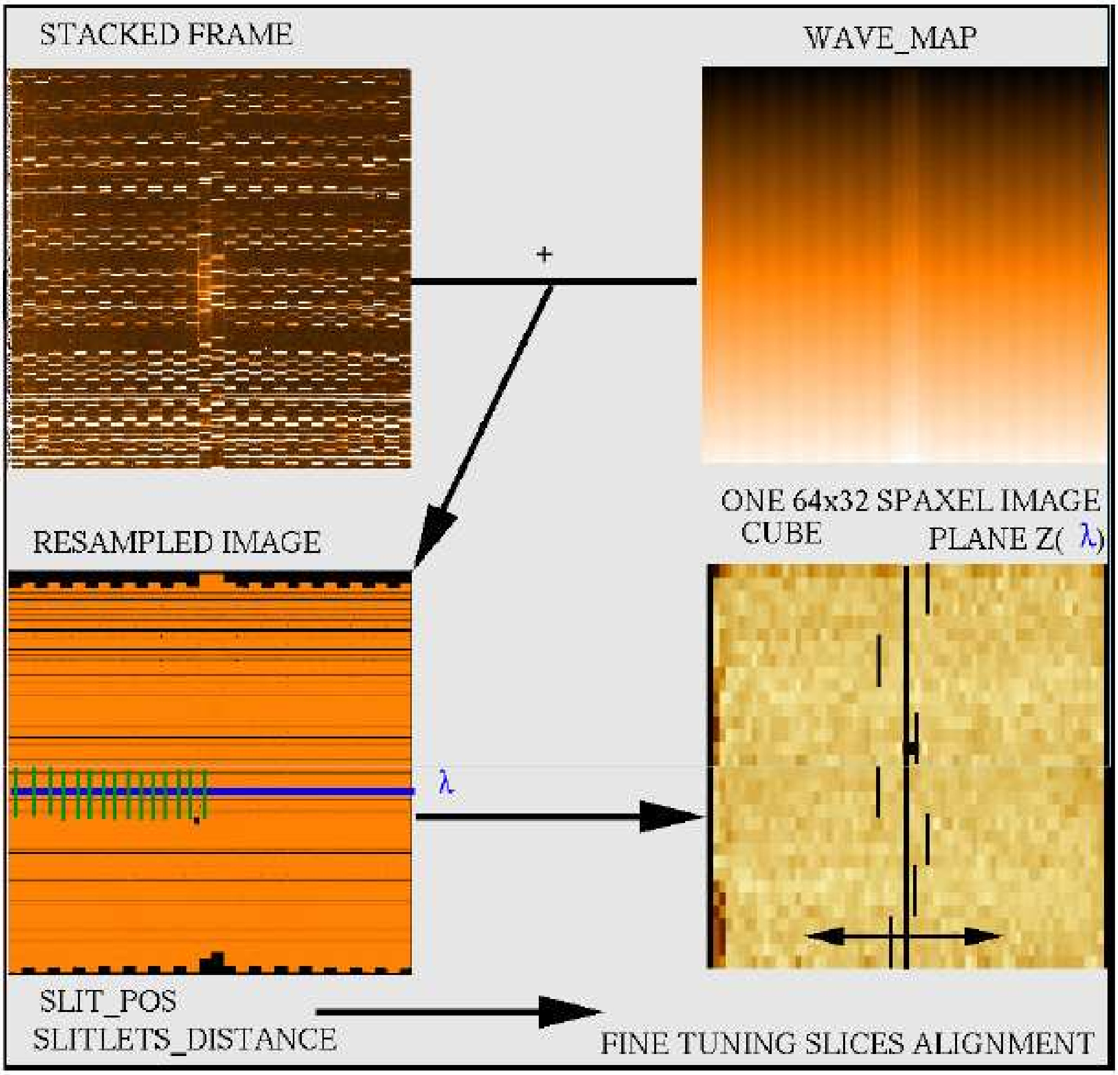

Figure 2.13.: Cube reconstruction: raw data are re-sampled using a wavelength map to remove the brick-wall pattern. The slitlets are then stacked into a cube taking slitlet distances and edge positions into account. Each plane of the cube is a monochromatic image of the instrument FOV. (from: ESO-SINFONI user manual).

2.6.2. Data analysis

After performing the customized standard reduction pipeline to produce the final 3d-data-cubes, spectra where then extracted from the cubes. Therefore I integrate the signal over the largest single extraction aperture around the fitted PSF peaks for each wavelength slice. Residual wavelength jitter between the single spectra of the order of 1/10 of a pixel was corrected by correlating the G0V stellar Brackett γ lines in every spec-

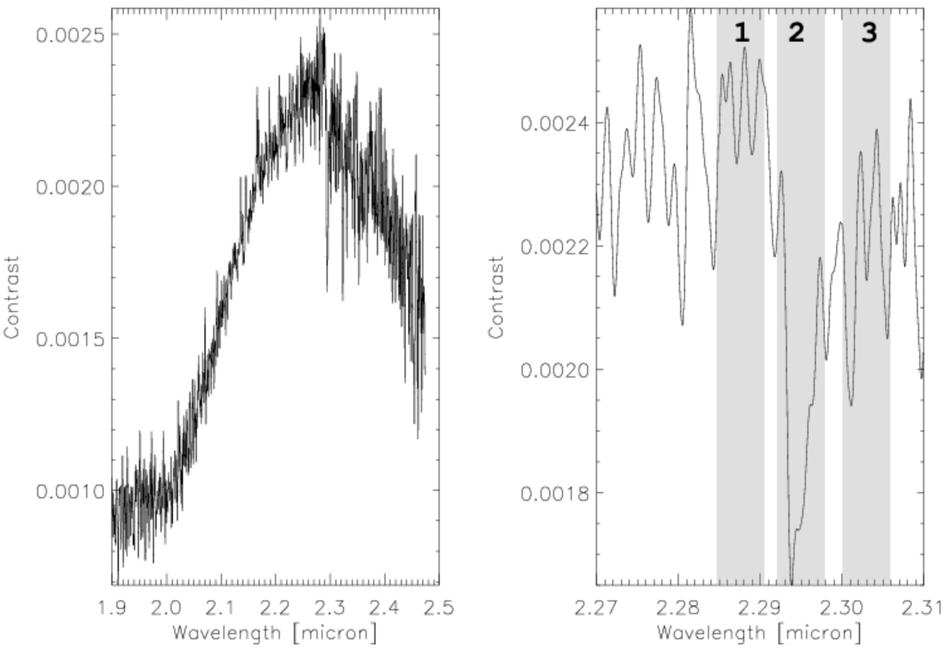

Figure 2.14.: Expected HD189733b K-Band spectrum based on a modified model spectrum by Barman (2005). Left: K-Band contrast model spectrum for HD 189733b. For analysis of the broad band spectrum (Method A), pairs of 'in' and 'out of' eclipse spectra taken at the same airmass were compared. Right: Narrow band CO-feature at 2.29 micron, grey areas and numbers highlight the wavelength ranges used to define the spectral index $I_s = (F_1 - F_2 + F_3)/(F_1 + F_2 + F_3)$. A time-series of this Index was analyzed in a spectral differential and decorrelation method (Method B).

trum. Alternatively cross-correlation of the complete extracted spectra over all wavelengths was used to compute the shifts in wavelength direction. This method is capable of measuring these pixel-shifts with an accuracy of about 1/100 pixel (Angerhausen et al., 2006).

We used a synthetic standard atmospheric spectrum based on the ATRAN code (Lord, 1992) and created a spectral box filter indicating those spectral bands with a transmission exceeding 97 percent (see fig. 2.16) . The product of such spectral box filter $F(\lambda)$ and each stellar spectrum S_i,

$$S_{i,tot} = \sum_{\lambda} S_i(\lambda)F(\lambda) \tag{2.2}$$

provided a reliable indicator of the transmission fluctuations throughout the night.

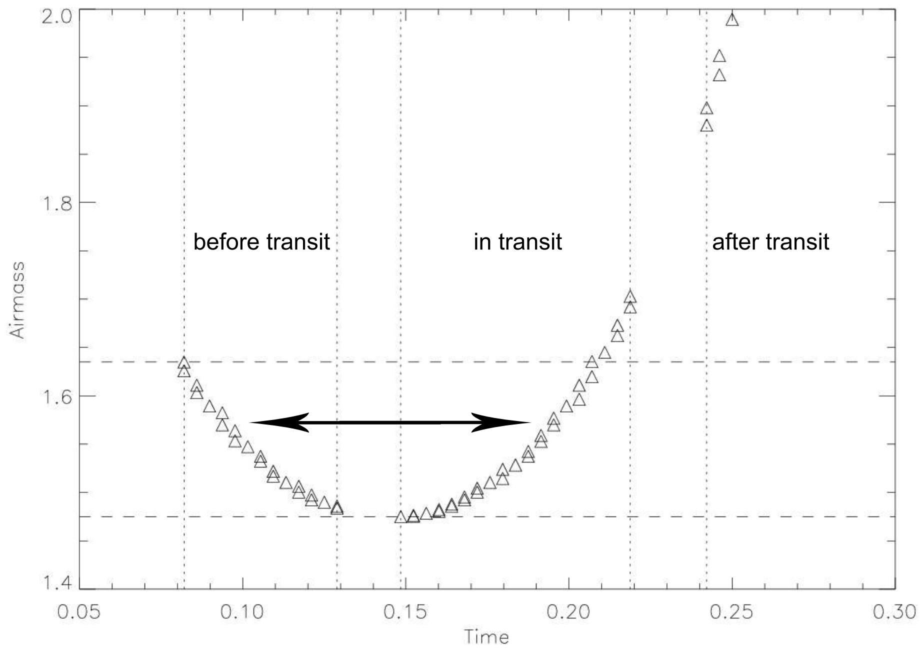

Figure 2.15.: Plot of airmass against time during the observation night to explain the basic idea of method A: Data before (left, between dotted lines) and in transit (middle, between dotted lines) were obtained in the same airmass range (between dashed lines). Pairs of spectra collected in both phases at the same airmass can be compared (arrow).

Each spectrum was then multiplied by the appropriate factor. As a next step the spectra were corrected for different air masses. Since each spectral channel has its own absorption characteristics, the individual zenith distance dependencies had to be computed and individually corrected for each wavelength channel. The spectra were divided into 2 groups, during occultation and out-of occultation and treated separately. A linear unconstrained ln(signal) versus airmass fit was used in each spectral channel for both data-sets.

After these corrections were applied, all spectra obtained were adjusted and aligned for overall transmission, wavelength shift and residual small airmass differences (see fig. 2.17).

Spectra from both phases were separately averaged to form two mean spectra. The planet/star contrast was obtained by dividing the out-of occultation spectrum by the occultation spectrum. Since the stellar component is present in both spectra, the ratio will cancel the stellar contribution completely, including stellar light reflected off the planetary atmosphere.

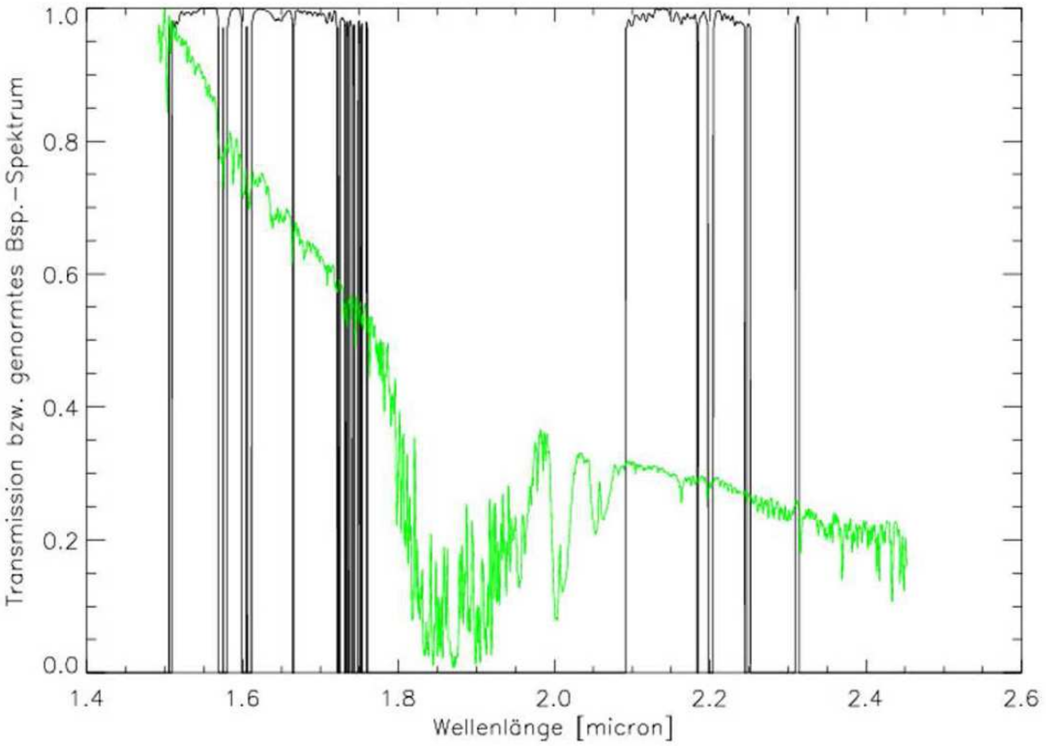

Figure 2.16.: Example of a SINFONI spectrum (green, scaled) and the atmospheric filter (black). We used a synthetic standard atmospheric spectrum based on the ATRAN code (Lord, 1992) and created the spectral box filter by indicating those spectral bands with a transmission exceeding 97 percent. The product of such spectral box filter and each stellar spectrum, provided a reliable indicator of the transmission fluctuations throughout the night.

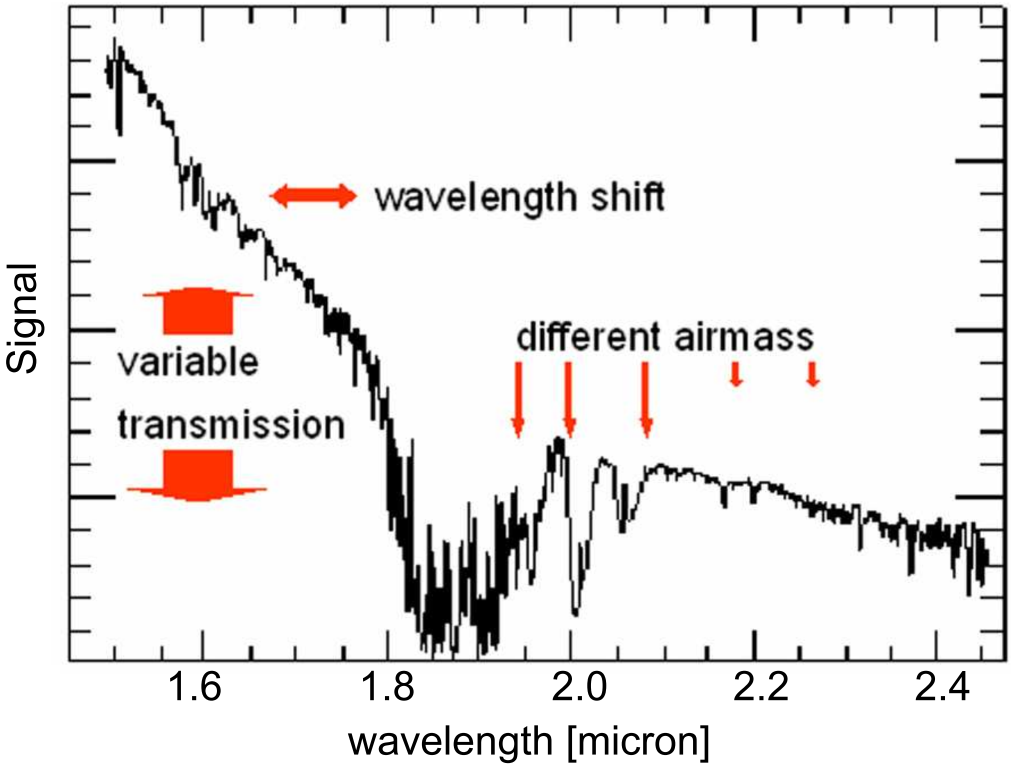

Figure 2.17.: Averaged spectrum for the 2005 HD209 observation in H+K-band. To directly compare the spectra corrections for different overall transmission, airmass and wavelength shift had to by applied.

It will also account for all instrumental effects. Alternatively spectra in and out of eclipse at same elevations were compared directly and average of this set of relative spectra computed. Results were almost identical (see fig. 2.18).

2.6.3. Results

The emerging final H- and K-band spectra of the 2005 SINFONI observation of HD 209458b are displayed in figure 2.18. The overall shape of the spectra seems to be dominated by systematic effects, since the baselines of the spectra are varying much more than what can theoretically be expected from the extrasolar planet in that system. The intrinsic noise per sample position, measured relative to a 60-channel smoothed spectrum (fig. 2.18), is of the order of 1/2500 in the H-band and 1/1400 in the K-band spectrum. These values are very close to the expected numbers from model S/N calculations (see A.2), if one also accounts for the fact that only a quarter of the expected data was accumulated. Based on these findings, the observation shows that, in general, single spectral features might not be affected by systematic noise and it might in fact be possible to correlate our data relative to model spectra in the literature. Since narrow band noise (see fig. 2.18) compares well with the calculations, spectral lines and narrow band features are probably not dominated by systematic effects.

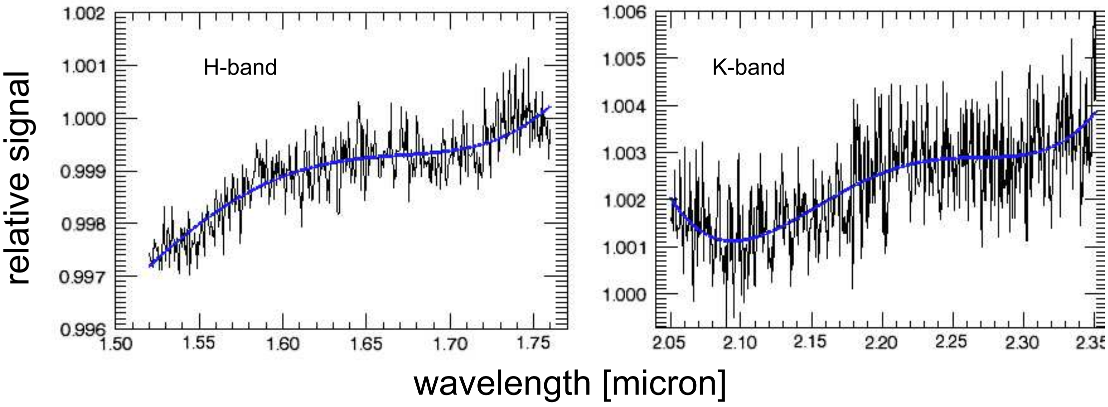

Figure 2.18.: Results of method A: the emerging final H- and K-band spectra of the 2005 SINFONI observation of HD 209458b. The overall shape of the spectra seems to be dominated by systematic effects, since the baselines of the spectra are varying much more than what can theoretically be expected from the extrasolar planet. The intrinsic noise per sample position, measured relative to a 60-channel smoothed spectrum (blue), is of the order of 1/2500 in the H-band and 1/1400 in the K-band spectrum. These values are very close to the expected numbers if one also accounts for the fact that only a quarter of the expected data was accumulated.

Analysis of the results and the residuals that remained in method A showed that one of the most important contributions of systematic noise is the change of concentration of atmospheric trace gases (see fig. 2.19). This together with the option to use the characteristic shape of a transit light-curve to actually search for the expected box-car-shaped transit signature, was a motivation for method B.

2.7. Parametrization of changes in atmospheric trace gas concentrations

Before I get to the second method, I insert a section that describes a method to parameterize changes in atmospheric trace gas concentrations during an observational night. These parameters describe the dynamic behavior of the atmospheric constituents during observation. They were used along with a set of other, mostly instrumental, observational parameters in the 'decorrelation' method B.

Spectral time-series observations, such as exoplanetary transit spectrophotometry or spectroscopically resolved observations of transient flares or variables, need photometric stability in each wavelength channel of up to 10^{-4}. However, for ground-based observations even slight changes in the concentration of trace gases in the optical path through the earth's atmosphere can change the transmission in certain lines up to a few percent on the same timescales like the observed events (fig. 2.19). Therefore knowledge about the changes of concentration of those molecules is absolutely necessary for temporally resolved ground-based spectroscopic investigations.

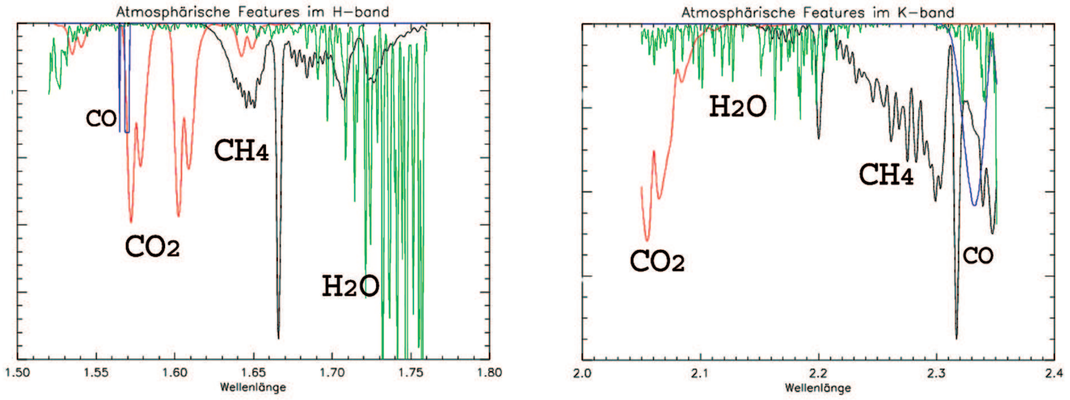

Figure 2.19.: Near infrared absorption characteristics of the dominant atmospheric trace gases in the NIR. The transmission curves caused by carbon-oxide (blue), carbon-dioxide (red), water (green) and methane (black) plotted for H- and K-band (not to scale). These spectra were computed using ATRAN (Lord, 1992).

The first tests of our observing strategy for ground-based exoplanet transit spectroscopy (Angerhausen, 2006) showed that the resulting spectra are still dominated by systematic effects, especially those caused by changes in atmospheric trace gases such as methane and water. However, further analysis showed that in general systematic effects in the time-series can be very well decorrelated if they can be parameterized by an observational parameter, observed simultaneously to the science data acquisition. It was shown to work especially for integral field units (Arribas et al. 2006) such as SINFONI or OSIRIS, that I use for my tests, because systematic changes are well conserved within the 3 dimensional data-cubes. For example the changes of the point spread function (x/y-center-position on the detector, FWHM, ellipticity etc.) as a function of wavelength and time are very well traceable with imaging spectrographs. I already expanded this method to meteorological parameters, such as local humidity or air-pressure, obtained from weather stations on the telescope site (Angerhausen et al. 2009). Here I present a method to also parameterize the changes of atmospheric trace gases (see fig. 2.19), caused e.g. by diurnal photochemistry of those molecules or temporal appearance of clouds of variable composition.

2.7.1. Basic concept

The principle idea of the presented method is to compare the signal in specific molecular absorption lines to the signal in windows of high atmospheric transmission. The first step is to define this window and the specific molecular lines. I used the program ATRAN (Lord, 1992) to compute atmospheric transmission models.

ATRAN is a program that computes a synthetic/theoretical spectrum of atmospheric transmission. It works for all infrared-wavelengths with selectable resolution. Input parameters are location of the observatory, zenith angle and the atmospheric concentration of various trace gases (methane, CO, CO_2, water etc.). It can be used to compute wavelength-dependent transmission filters and correlations between spectra and particular telluric species.

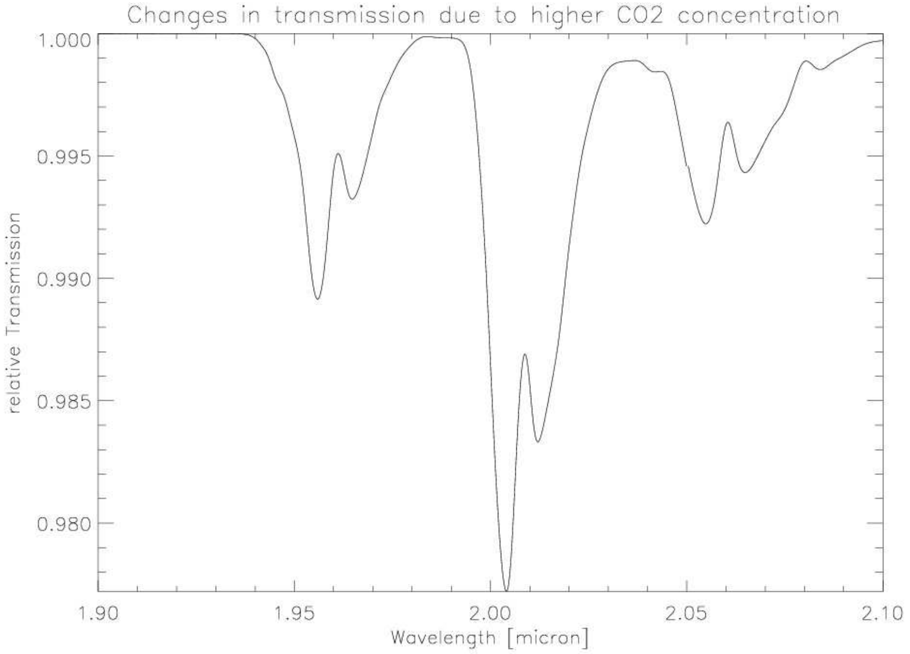

Figure 2.20.: Relative difference in transmission between a model assuming 320 ppm and a model with 330 ppm of CO_2: An increase of 10 ppm of atmospheric CO_2 causes an up to 2 percent deeper absorption in the CO_2-Bands between 1.9 and 2.1 micron (Modelled with ATRAN, Lord1992). Knowledge about the changes of concentration of molecules in the optical path through the earth's atmosphere is absolutely necessary for temporally resolved ground-based spectroscopic investigations. This increase in absorption of greenhouse gases is, by the way, also an example for the consequences of climate change, ground-based astronomers have to face nowadays.

)

Comparing models with different molecular abundances of the species that we are interested in (CH_4, H_2O, CO_2) reveals their specific absorption. Figure 2.21 shows an atmospheric transmission model (top) and the specific absorption spectra of water (2nd from top), methane (middle) and carbon-dioxide (2nd from bottom). The shaded grey areas mark the significant absorption lines of these species, such as those of water between 2.1 and 2.2 micron, methane at 2.2, 2.32 and 2.37 micron and the two broad carbon-dioxide bands between 2 and 2.1 micron. The bottom spectrum shows an average stellar spectrum of the 70 exposures of our observation. The spectral area between the two dashed lines defines the central wavelength band of maximum transmission that was used as reference signal.

2.7.2. Correlation with other observational parameters

Unfortunately, but not surprisingly those raw time-series of the flux-ratios between the molecular lines and the transmission window are not independent from other parameters. Obviously changing airmass during the observation directly correlates with the depth of the absorption lines (see fig. bottom). Calculations of the covariance of the molecule parameters with other observational parameters showed, that two other instrument specific values also strongly bias the result. One is the rather random change of the broadband slope of the spectra (see fig.2.22 top), caused by the spectral extraction routine, that was used to extract the spectra from the data-cubes. The other is the FWHM of the PSF in the original data-cubes.

To separate the effects caused by changing concentration of telluric molecules, the time-series of the flux-ratios need to be decorrelated with these three parameters. It should be mentioned that its also possible to perform a principle component analysis (Pearson, 1901) on all observational parameters (instrumental, PSF and atmospheric) for further analysis of the original science data time series. Here we emphasize on the

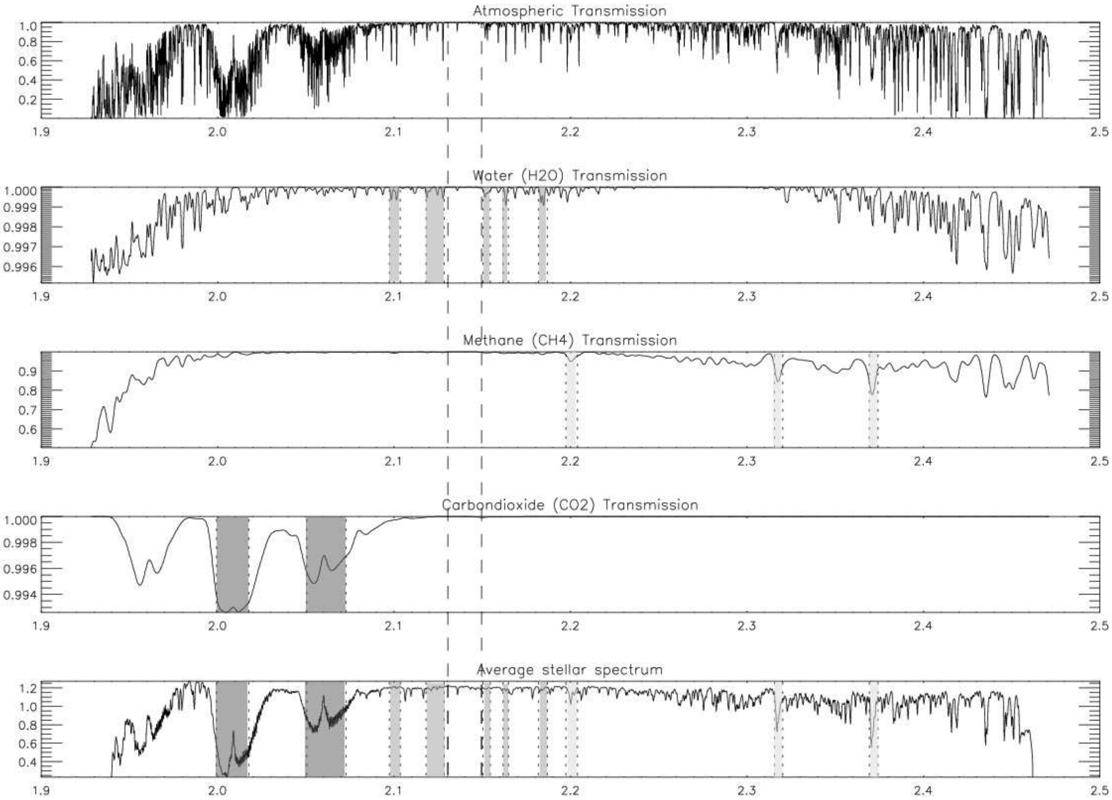

Figure 2.21.: Atmospheric transmission model (top) and the specific absorption spectra of water (2nd from top), methane (middle) and carbon-dioxide (2nd from bottom). The shaded grey areas mark the significant absorption lines of these species. The bottom spectrum shows an average stellar spectrum of the 70 exposures of our observation. The spectral area between the dashed lines defines the central wavelength band of maximum transmission that was used as reference signal. Parameters for the concentration of the atmospheric trace gases can be extracted by comparing the signal in the molecular lines to the reference signal.

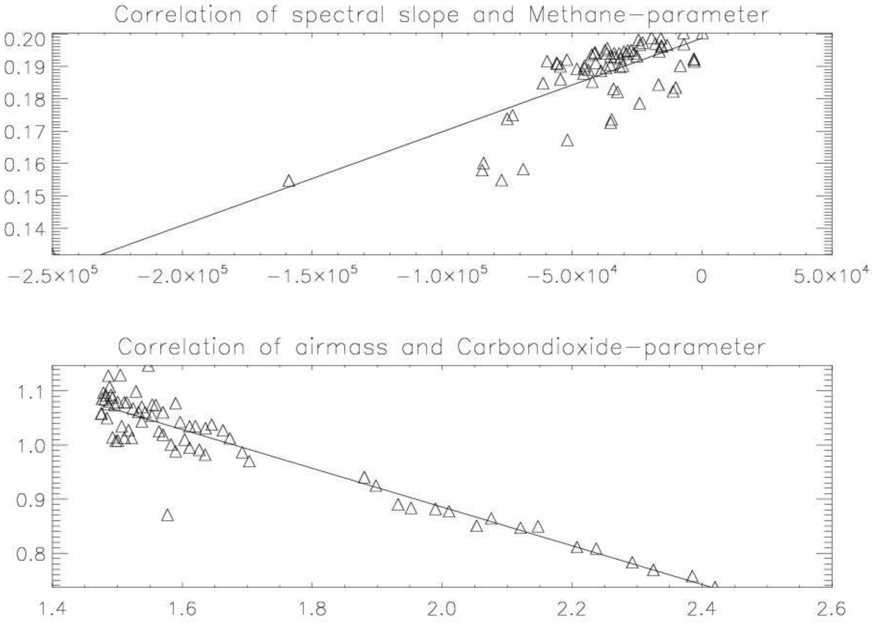

Figure 2.22.: Examples for the strong correlation between the raw methane index and the spectral slope (top) and between the carbon-dioxide index and the airmass. These effect as well a another correlation with the FWHM of the PSF had to be accounted for to obtain the final result (or final decorrelated index).

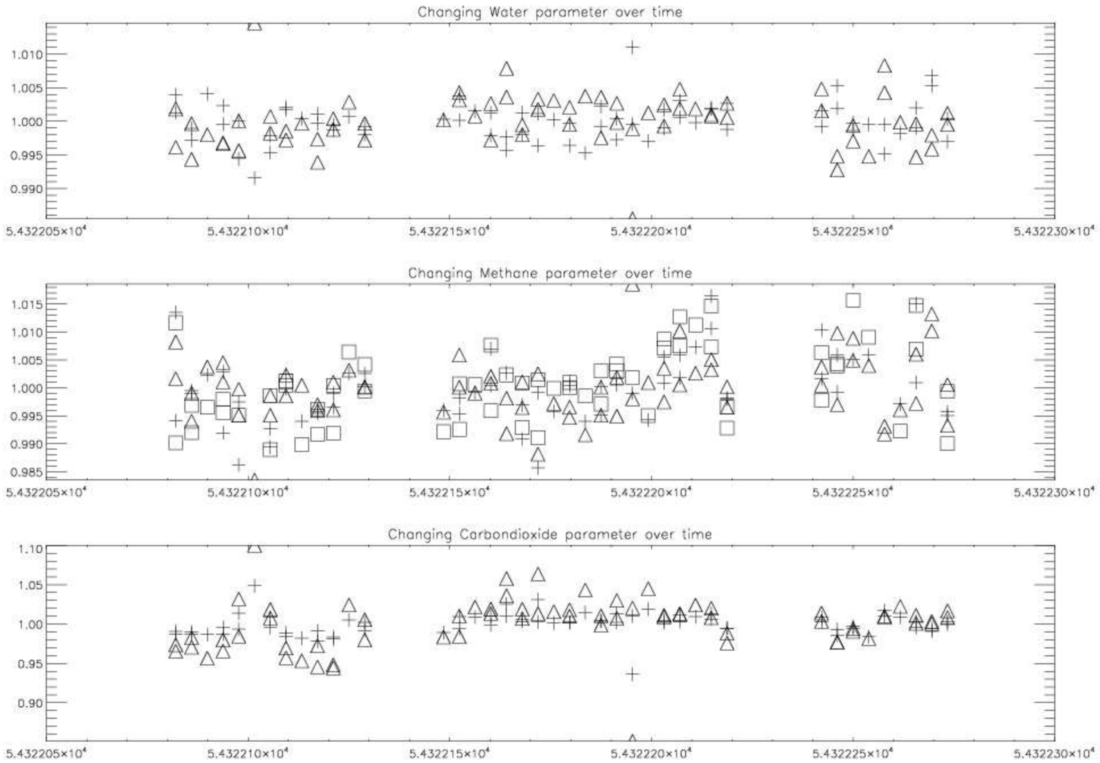

Figure 2.23.: Time-series of the water- (top), methane- (middle) and carbon-dioxide- (bottom) parameter. Different symbols refer to different reference lines of the specific molecule defined in figure 2.21 .

separation of the trace gas effect and therefore demonstrate this disentanglement.

After the decorrelation of the index from other observational parameters or instrumental effect, such as airmass variation or spectral slope, one is able to give a time-series of values representing the concentrations in the analyzed molecules. Figure 2.23 shows that for different reference lines of the particular species the variation is the same. Figure 2.24 shows time-series of the average for each of the 3 molecules.

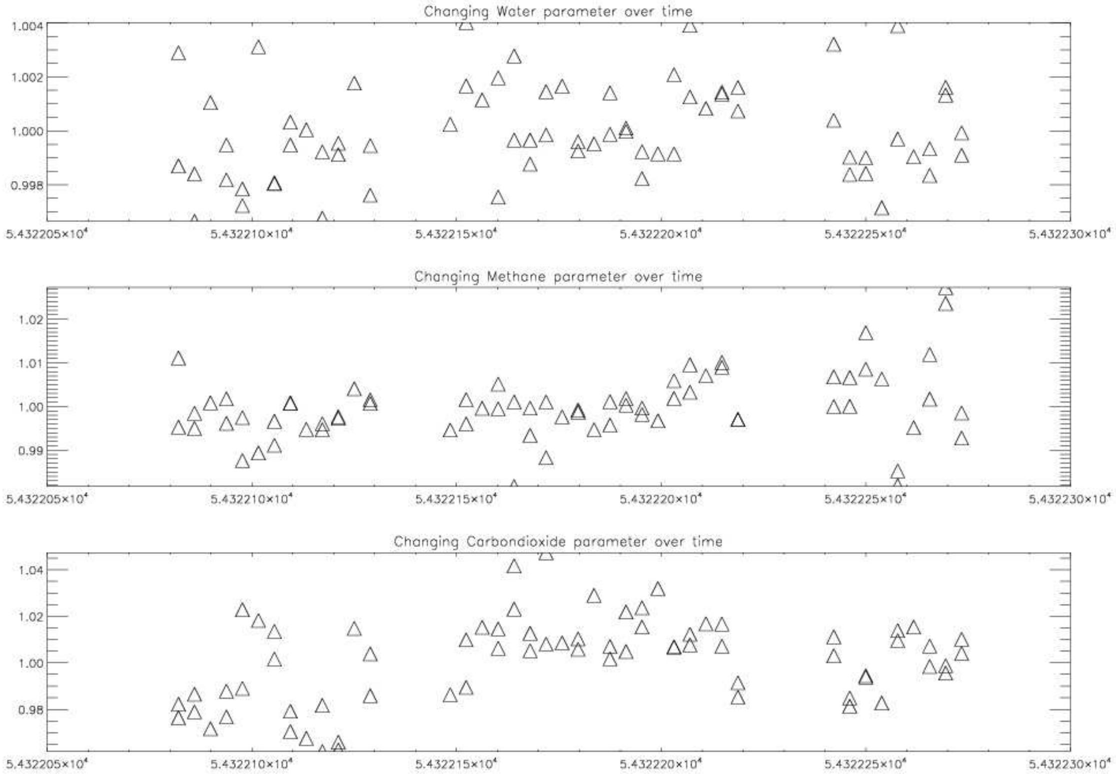

Figure 2.24.: Time-series of the *mean* water- (top), methane- (middle) and carbon-dioxide- (bottom) parameter. Random outliers possibly correlate with a yet undiscovered parameter. However the expected increase of methane and carbon-oxide during the night, caused by e.g. lower UV-photochemistry of CH_4 and photosynthesis for CO_2, is clearly present.

2.7.3. Summary

For our example night the water absorption only changes about 1 percent and rather randomly. One can also see clear trends of increasing methane and carbon-dioxide during the night. These effect are on a much higher level (up to some percents) and represent what one would expect from meteorological scenarios for the diurnal changes in the atmosphere's photochemistry.

It can even be shown (fig. 2.24) that the water-parameter derived by the introduced method correlates with the parameter given for the local humidity at the telescope site, provided by the observatories weather station.

This correlation of two independently acquired parameters and the reproduction of the expected trends in CO_2 and CH_4 are strong argument for the physical correctness of the described method.

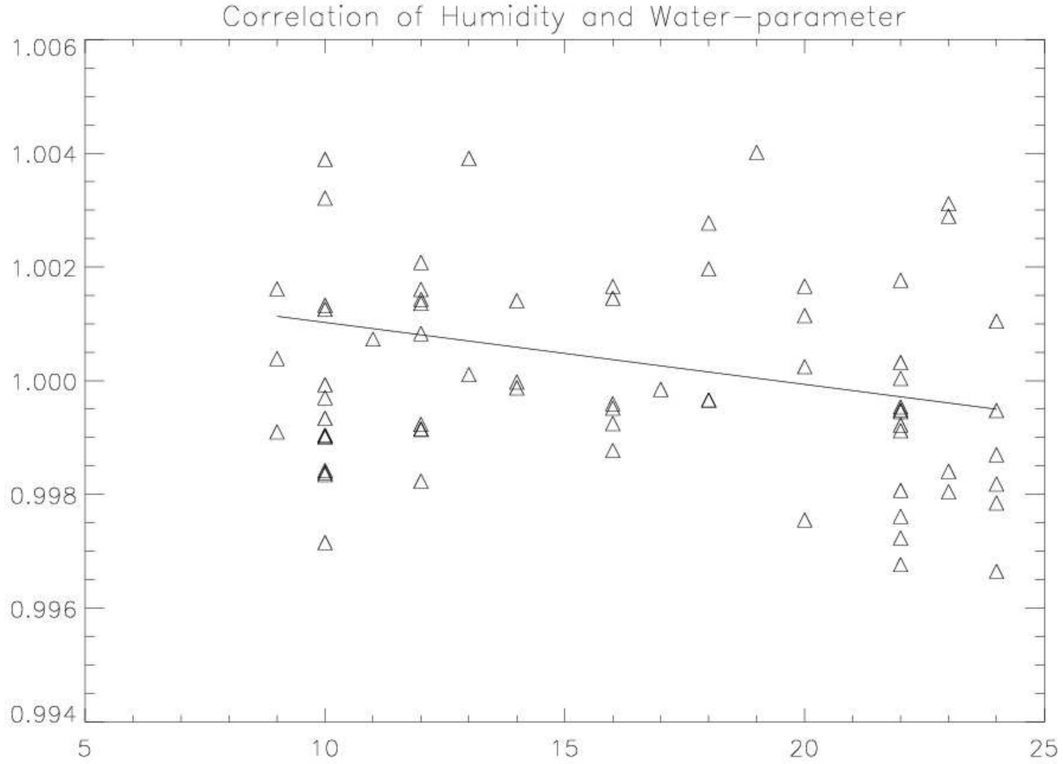

Figure 2.25.: Plot of the water-parameter, derived with the described method, versus the parameter of local humidity, obtained from the telescopes site weather station. The correlation of both independently acquired parameters is a strong argument for the physical correctness of the described method.

2.8. Method B: analysis of predicted narrow line features

I realized from method A that I can not separate effects of the earth's atmosphere in a direct spectroscopic approach. Instead I needed to make use of the fact that a transit light-curve has a characteristic box-car-shape with well known phase, while atmospheric effects may happen on the same timescale but as smoother functions of time. Method B searches for that characteristic transit shaped light-curve in the relative signal between three channels, of which one preferably contains a predicted feature in the planetary spectrum (see fig. 2.14 left).

Observational parameters

Arribas et al. (2006) presented a very powerful method to decorrelate observational parameters from the raw spectral light curves. Here I present an extension of that method to a wider range of parameters. First of all I present the way we derived those parameters, that can be divided into three parts. One are the observational parameters mostly derived from the header of the raw science files or local weather reports, such as airmass, seeing, local temperature or wind-speed . The second group is the parameters describing the point spread function at each wavelength over the time of the observation. The third are parameters that describe the change of atmospheric trace gases over the night (see previous section).

2.8.1. Decorrelation method

For the analysis of narrow band features a spectral index $I_s = \frac{F_{\lambda_1} - F_{\lambda_2} + F_{\lambda_3}}{F_{\lambda_1} + F_{\lambda_2} + F_{\lambda_3}}$ is defined, with λ_2 position near an expected spectral feature, e.g. the 2.3 micron CO-feature predicted by almost all models (fig. 2.14, left). The time-series of that index is decorrelated with the set of observational parameters such as airmass, seeing, location of the PSF on the detector, humidity and local temperature, that were mostly drawn from the science data headers (see fig. 2.26).

Each decorrelation step lowered the residual standards deviation and cleaned out the covariance with the used parameter (see fig. 2.27 table 2.1).

The same method was applied to an artificial dataset with a simulated planetary signal added to the out of eclipse spectra (fig. 2.28 bottom) and another data set with no planetary signal added. This was tested to see

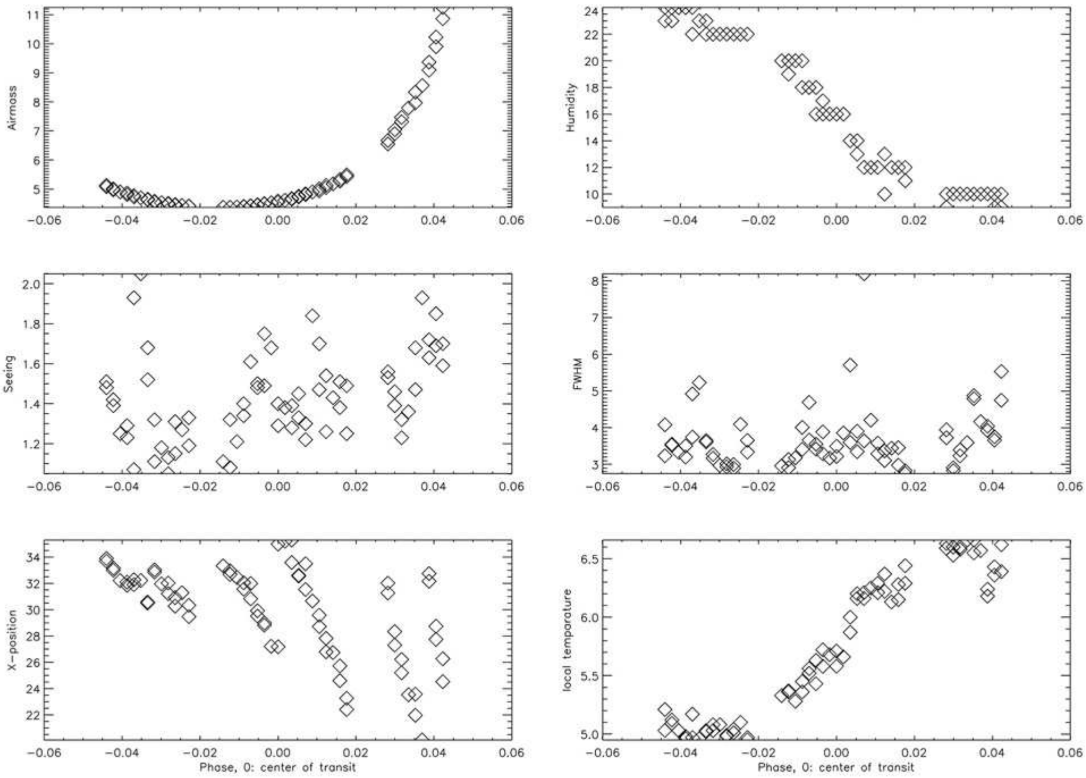

Figure 2.26.: Example of some observational parameters for the 2007 SINFONI run. Airmass (top, left), local humidity (top, right), seeing (center, left), FWHM (center, right), x-position on the detector (bottom, left) and local temperature (bottom, right)are plotted versus the observation time (scaled in planetary phase).

how deep the transit light-curve of an actual planetary signal would be after the 'indexing' and to exclude that the decorrelation imposts or destroys a transit signal.

This method is a powerful tool to improve the standard deviation of the time-series with each decorrelation step, while simultaneously separate the data from external influences during the observation. It can theoretically correct any systematic that is correlated to a parameter, as long as that parameter is observed simultaneously.

Observational parameter	Coefficient before airmass decorr.	Coefficient after airmass decorr.
Airmass	0.994045	0.000775055
Wind-speed	-0.567896	0.433901
Wavelength-shift	-0.348878	0.383352
Humidity	-0.638413	0.370100
Temperature	0.652521	-0.345674
Wind-direction	-0.0936889	0.112939
Strehl Ratio	0.588461	-0.00937599
Seeing	0.474509	-0.00885338
Pressure	-0.909824	0.131780
X-center PSF	-0.515934	0.107597
Y-center PSF	0.631093	-0.320321
FWHM in X-dir.	0.211757	-0.147461
FWHM in Y-dir. FIT	0.192949	-0.187359

Table 2.1.: Covariance coefficient for a set of observational parameters with the spectral index before (left) and after (right) airmass decorrelation. The left column shows that the airmass has the most significant correlation with the index at the start of the analysis. After the decorrelation of the airmass (right column) the covariance is down to $\sim 10^{-4}$. Also the covariance of Strehl-ratio and seeing, that are obviously correlated to the airmass, are much lower. Decorrelation steps like this (compare with fig. 2.27) were iterated - in each case using the parameter with the largest covariance - to get to the final light-curve (fig. 2.28 top).

2.9. Conclusions of Method A and B

Our study showed that we can reach the necessary levels of signal to noise of about 10^4 to detect the planetary signal. The observed depth of the light-curve in the 2.3 micron feature (fig. 2.28 top) is as deep as expected from the model (fig. 2.28 bottom), but it can not completely be excluded that this signal is caused by another observational bias that was not correlated to any of the used observational parameters.

Instrument systematics, changing airmass and even noise induced by weather parameters have been decorrelated with the described method. Nevertheless the central problem of variability in concentration of atmospheric trace gases, due to changing diurnal photochemistry can still bias the results. Our model calculations and the result of this work demonstrate the feasibility of the described spectroscopic observations. How-

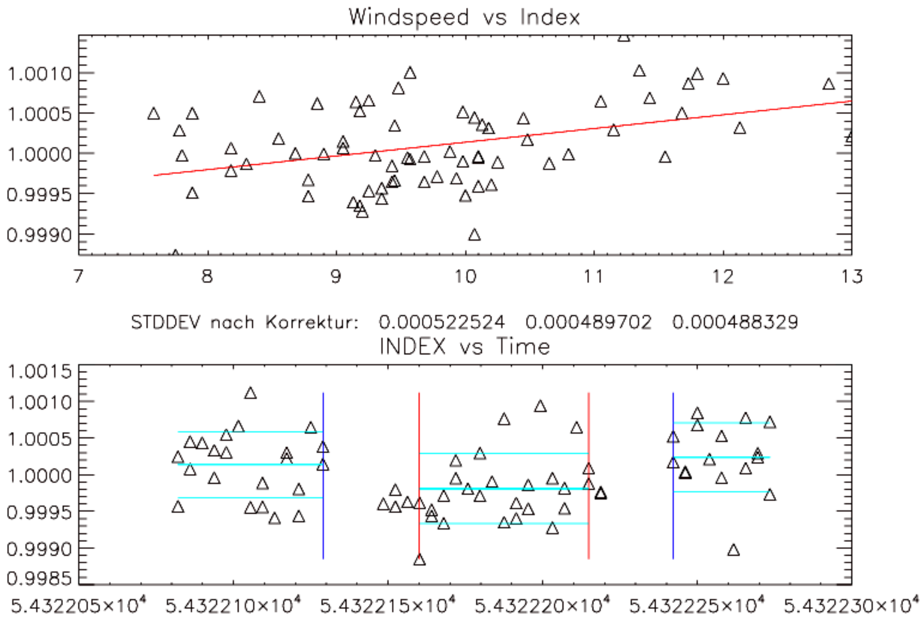

Figure 2.27.: Example of one decorrelation step used in method B. Top: The spectral Index I_s is plotted against the observational parameter wind-speed. The significant covariance was then decorrelated by substracting a linear fit. Bottom: time-series of spectral index with improved standard deviation after decorrelation (between the red lines: in eclipse, left and right: out of eclipse).

ever, problems concerning changes in atmospheric trace gases and the optimization of the decorrelation method are needed to be solved. Therefore the lessons learned from prior observations and even more advanced methods and experiences from within the community were used to set up method C.

2.10. Method C: The self-coherence method

Alternately, one can make use of a technique introduced by my collaborator P. Deroo that removes the Earth-atmospheric variability by correlating a number of spectral channels at full resolution to arrive at a signal at lower spectral resolution. This method employs an iterative approach to remove systematic errors, while the eclipse signal is extracted by computing a self-coherent spectrum of groups of channels. This technique has

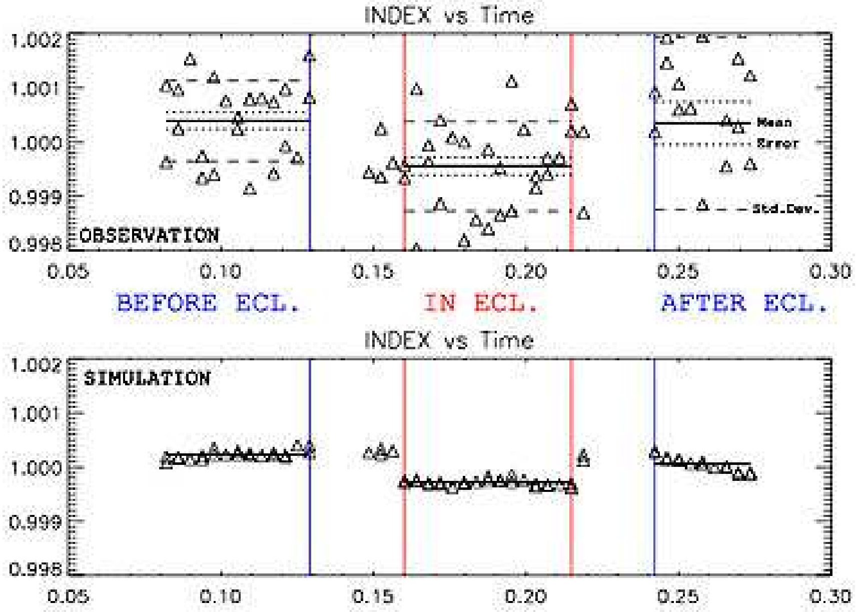

Figure 2.28.: Final light-curve of the spectral Index I_s of the 2.3 micron feature of the observed data (top; solid: Phase-mean, dashed: Standard deviation, dotted: error) and a noise-free simulated dataset (bottom). The observed depth of the light-curve in the 2.3 micron feature (top) is as deep as expected from the model (bottom). The bottom light-curve also demonstrates that the described method B conserves the transit signal. Another test performed with an artificial dataset without planet excluded that the method imposts a transit signal.

successfully been tested on an IRTF SpeX data-set (see fig. 2.29) of a secondary eclipse of HD 189733b (see 2.4.3 for details on this planet) , resulting in the first ever exoplanet spectrum observed from the ground.

The first step of this method is to divide the data in blocks of (in the IRTF case) 100 and 150 spectral channels in the K-band and L-band, respectively. For each block, the mean is computed and used to renormalize the individual time series. The objective of the normalization is to remove the common-mode systematic error components. The second step is to do a channel-by-channel air mass correction (similar to the decorrelation steps of method B), yielding a corrected time series. The next step is to iterate the channel-by-channel air mass correction and subsequent formation of the renormalized spectral channel time series. It can be shown, that this process of iterative normalization and de-trending converges quickly (for j= 4 or 5) at most wavelengths. Convergence is defined as the value of the renormalized flux density changing by less than 1 part in 10,000 at all wavelengths of interest. When the convergence criteria have been met, the common-mode and the non-common-mode (temporal) systematic errors have been reduced substantially. After that the signal, that is correlated in time between spectral channels, is extracted. This is done by forming the product of the Fourier transform of each individual renormalized time series in the defined blocks of 100-150 spectral channels. The product is normalized and transformed back into the time domain.

There is still some residual curvature and ripple in the resulting light-curves after the transformation back into the time domain. This is removed with a simultaneous minimization to the eclipse depth and a 3rd order polynomial. The result is a light-curve where the eclipse is detected at high signal-to-noise (see fig. 2.29)

An extensive description of the method along with a discussion of its specific assets and limitations is contained in a paper recently published (Swain et al., 2010).

Due to a different observing strategy, I regrettably did not observe the ingress or egress portion of the light-curve during that the previously described observations with SINFONI. Therefore the self-coherence approach is not directly applicable to this data.

2.11. Summary

Our study showed that we can reach the necessary levels of signal to noise of about 10^4 to detect the planetary signal. Instrument systematics, changing airmass and even noise induced by weather parameters can be decorrelated to a large extend with the described method. Nevertheless the central problem of variability in concentration of atmospheric trace gases, due to changing diurnal photochemistry has to be solved. Method C shows great potential to finally solve the issues of ground-based spectrophotometry of transiting exoplanets. I am currently working together with a team of collaborators on an expansion of this technique to other sets of data, e.g. taken with different instruments at different spectral resolution. Obviously, as the ground-based techniques are improved upon and refined, they promise to step jump in terms of both the number of observable planets (with large telescopes) as well as a dramatic improvement in the available spectral resolution.

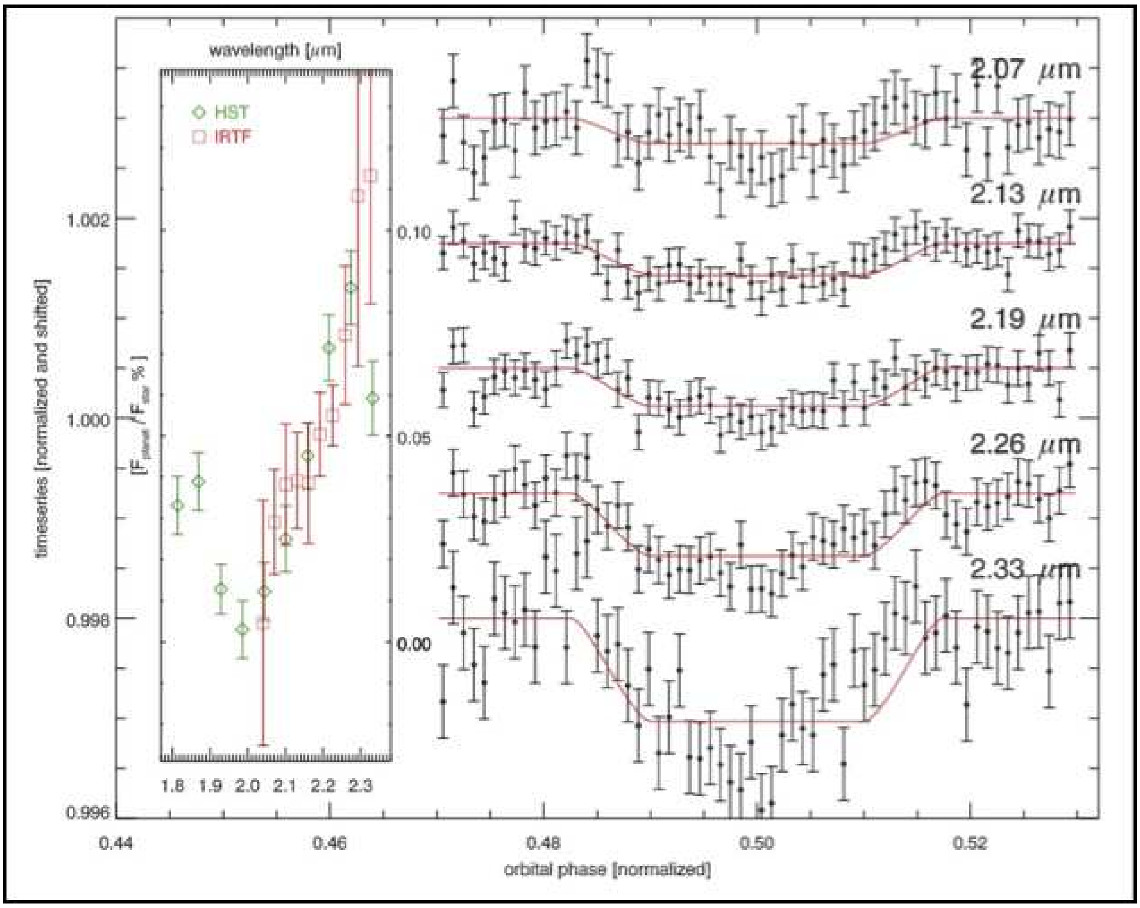

Figure 2.29.: Using the ground-based Infrared Telescope Facility (IRTF), in a collaborative project (Swain et al., 2010), we have obtained the day-side emission spectrum for HD 189733b between 2.0 and 2.4 $\mu\ m$. The light curves (right, for 5 example channels) show the measured secondary eclipse depth and the excellent agreement between the ground-based and space-based measurements the Hubble Space Telescope (left; green: HST, red: IRTF). Each calibrated light curve includes the averaged measurements (right, black diamonds with $\pm 1\ \sigma$ errors), and the best-fit eclipse model (red). In the comparison between ground-based and space-based measurements, the secondary eclipse depth is shown as the planet/star contrast ratio (Swain et al., 2010).

3. Space-based: HST-NICMOS observation of GJ436b

In this chapter I present a revised analysis of a previously published dataset of two primary eclipses of the transiting 'Hot Neptune' exoplanet GJ 436b with the HST-NICMOS instrument. I was able to extract a near infrared (NIR) spectrum of GJ 436b at a resolution of $R \simeq 30$ in the wavelength range from 1.3 to 1.9 micron. The final spectra for both visits are consistent with previous results.

3.1. Introduction

Due to their intrinsic measurement stability and the lack of an intervening atmosphere, space-based platforms allow excellent photometric capability, and considerable progress in measuring transmission and emission-spectra of transiting gas-giant planets. First successes were obtained with the Hubble Space Telescope's (HST) STIS instrument (Charbonneau et al. 2002) and with Spitzer in the mid-infrared with IRS (Richardson et al. 2007, Grillmair et al. 2007, Grillmair et al. 2008, Swain, Vasisht & Tinetti 2008) and in broadband photometry spanning nearly a decade in wavelength (Charbonneau et al. 2008, Knutson et al. 2008).

Spectroscopic analysis at near infrared wavelengths or near wavebands where the emission of these hot exoplanets peaks, has succeeded spectacularly with the NICMOS imager and spectrograph on-board the Hubble Space Telescope (HST). After the first detection of methane in the atmosphere of HD 189733b using HST-NICMOS transit time-series observations (Swain, Vasisht & Tinetti 2008) and demonstration of the feasibility of these types of measurements, this technique has been used to spectro-photometrically characterize three Jupiter-sized objects (HD 189733b, HD 209458b and XO-1b) in primary transit and secondary eclipse (Swain et al. 2009a, Swain et al. 2009b, Tinetti et al. 2010). Pont et al. (2009) acquired NICMOS spectrophotometric data on the Neptune analog GJ 436b. Herein I apply methods that I have developed to carefully calibrate these data. The ultimate goal is expand the method of primary transit spectrophotometry that probes the atmospheric composition, to smaller transiting objects and leading eventually to Super Earth spectra one day; GJ 436b is a $\simeq 22$ Earth-mass planet (0.072 M_J), representing the class of 'Hot Neptunes', albeit with an equilibrium temperature of 700 K, a factor of two lower than Jupiter mass planets such as HD 189733b and HD 209458b. GJ 436b is amongst the least massive transiting exoplanets (two super Earth class exoplanets, CoRoT-7b, and the recently discovered nearby super Earth, GJ 1214b, are lighter). A major advantage is that much like GJ 1214b, it orbits a relatively bright, nearby M2V parent star (V $= 10.68$, d $= 10.2$ pc, radius ~ 0.44 $R_\odot$) of small stellar radius that offers the opportunity of measurable contrast in transmission. Planetary models of GJ 436b suggest that it probably consists of a modest rocky core (more than 45% in mass), a very deep layer of methane-ammonia-water ice, and a significant (10 - 20% in mass) H-He envelope (Gillon et al. 2007, Figueira et al. 2009). These characteristics, and its anomalously high eccentric (e=0.15), moderate 2.64 day orbital, and a relatively cool temperature of about 700 K (Deming et al. 2007) make GJ 436b an important object for the theories addressing the assembly of materials during planetary migration and formation in the inner proto-planetary disc.

GJ 436 - the parent star

Name	GJ 436
Distance	10.2 pc
Spectral Type	M2.5
Apparent Magnitude V	10.68
Mass	0.452 (±0.012) M_{sun}
Age	6 (-5 +4) Gyr
Effective Temperature	3684 (-55+87) K
Radius	0.464 (-0.011+0.009) R_{sun}
Metallicity [Fe/H]	-0.32 (± 0.12)
Right Asc. Coord.	11 42 11
Decl. Coord.	+26 42 23

GJ 436b - the planet

Name	GJ 436 b
Discovered in	2004
Mass	0.072 (± 0.0025) M_{Jup}
Semi major axis	0.02872 (±6e-05) AU
Orbital period	2.6438986 (± 1.6e-06) days
Eccentricity	0.15 (± 0.012)
ω	351 (± 1.2) deg.
Radius	0.438 (-0.03+0.04) R_{Jup}
Ttransit	2454222.61588 (± 0.00012)
Inclination	85.8 (±0.25) deg.

3.2. Observations

GJ 436 was observed twice, phased around primary eclipses on Nov. 11 (visit 1) and Dec.15, 2007 (visit 2), using NICMOS G141 objective mode grism-spectroscopy (spectral range $1.1 - 1.9$ μm, resolution $\simeq 200$). Because in its standard configuration the instrument point spread function is severely undersampled, the NIC3 camera was set to DEFOCUS mode as that allows improved photometric performance against inevitable image motion. The applied defocus ($\simeq$ 5 pixels FWHM) mitigates photometric systematics, but cannot prevent these from occurring in entirety. This is because the detector response changes do not appear only on spatial-scales similar to the defocused PSF, but also rolls off at pixel edges on sub-pixel scales (the so called intra-pixel response). Whereas the defocus does help with the intra-pixel response, the very act of defocusing the instrument imposes considerable diffraction-induced ringing in the monochromatic PSF; this ringing is present on scales of λ/D, which is smaller than the pixel scale for NIC3. As a consequence, even subpixel wander, ~ 0.1 pixel, can lead to photometric systematics of the amplitude of the sought after signal. If the wander is small, its effects on the spectrophotometry can be removed by modelling the photometry as linear in perturbations (e.g. Swain, Vasisht & Tinetti, 2008).

The Hubble time-series of GJ 436 are segmented, i.e. they are interrupted by Earth-occultation of telescope and this complicates the analysis somewhat. Visits 1 & 2 were scheduled in a manner such that three (of four) orbits observed the out-of-eclipse baseline, while the third intermediate orbit was phased to coincide with a portion of the 46 min transit duration along with the planetary egress (see fig. 3.1, top). As is now standard observing procedure, the first orbit was partially used to obtain a set of narrow-band exposures to help set the wavelength scale for the spectra. Past experience shows that the opto-mechanical positioning of the G141 grism in the first orbit (i.e. the rotation of the dispersion axis w.r.t to undeviated ray) can be significantly different than in subsequent orbits and can result in image motion on the detector of up to 0.5 pixels from the mean position. Consequently, light-curves from the first orbit must be treated more carefully, and more often than not, eventually discarded from later analysis.

During each orbit about 180-250 exposures were taken adding up to about 900 exposures per visit. These data have been acquired and previously analyzed and published in Pont et al., 2009 (hereafter P09). Whereas Pont et al. did show a derived spectrum from one of two visits, they did not concentrate on spectroscopy per se, and instead primarily chose to treat lump the data into broadband photometry in order to derive revised parameters that result from high precision light-curve photometry. Pont et al. use their spectroscopic analysis to search for water, which they do not detect at high significance. Given that they simply use one visit for spectroscopy, and do not reach the fundamental noise limits allowed by the data, I argued that it was scientifically worthwhile to mount a parallel investigation of this data-set. I reasoned that it was at least theoretically possible to improve the limits set by Pont et al. by slightly more than a factor of 2, bringing us into a regime where it might be possible for us to discern the signatures of molecular volatiles in the GJ 436b atmospheres.

I argue that this exercise is important for three reasons. First, unlike the hot Jupiters, for which the transmission signatures are relatively large and have already been detected (Swain, Vasisht & Tinetti 2008; Tinetti et al. 2010), GJ 436b is a relatively cooler, Neptune-mass planet with a smaller atmospheric scale height, making its spectroscopy both scientifically and technically interesting. Second, these data are valuable and unique, and improved data possibly cannot be reacquired (until after the launch of the James Webb Space Telescope, JWST) because of the on-going engineering problems with NICMOS. The third reason is purely technical. Co-adding visits or eclipses yields better signal-to-noise, and future observatories such as JWST will need to co-add spectra from several such observations in order to detect atmospheric signatures in transmission from planets such as Super Earths (e.g. Deming et al. 2009). However, no one has demonstrated this yet, because transit (spectro-)photometry often works in the regime where noise due to stellar activity, planetary activity and instrumental systematics all become important; in fact the transit literature is littered with inconsistent measurements. I reasoned that the two-visit data of GJ 436b present an excellent chance because (a) GJ 436b orbits a relatively quiescent M-dwarf primary, (b) is cooler, i.e. not massively irradiated, making its atmosphere relatively stable against variations due to weather (note that this is a purely intuitive argument and I have no *a priori* knowledge that it is indeed factual), and (c) its transmission signatures are expected to be small, i.e., near the limit of detection.

The remainder of this section describes the data analysis in detail. While the conclusions I reach are no different from those of Pont et al. 2009, i.e., that the transmission spectrum (or equivalently, the planetary radius) of GJ 436b in the wavelength octave spanning 1.1-1.9 microns is flat and featureless, I am able to do this with better error bars resulting from combining data from across two separate visits.

3.3. Data reduction

Considerable collective experience from the past shows that NICMOS spectrophotometry observations are corrupted by a combination of effects listed by decreasing importance to the data quality (see fig. 3.1 and 3.7):

(i) orbit-to-orbit offsets, or photometric jumps, that are due to the ever-so-slight errors in the opto-mechanical repositioning of the filter-wheel when the grism is rotated back into the optical path after each Earth occultation. Examination of this effect, using several data-sets, shows that the repositioning is generally worse in data acquired with the G141 grism. G206, the only other grism with which exoplanetary data using Hubble have been acquired, clearly shows much better repositioning even though it is located in the same filter wheel. This positioning error rotates the re-imaged spectrum on the detector around a fairly well defined pivot. Whereas the GJ 436b visits show rotation worse than past G206 data (Swain, Vasisht & Tinetti 2008; Swain et al. 2009), the performance is far superior to that in other data-sets acquired with the same grism, e.g., the four visits of HD 149026b (Carter et al. 2009). These orbit-to-orbit effects are generally the hardest to model and properly remove from the data.

(ii) intra-orbit systematics that correlate well with the spacecraft orbital phase and are most likely the result of change in thermal forcing of the telescope optical system as it re-enters the Earth's shadow. This causes a periodic trajectory of the telescope focus, the effects of which are relatively easy to remove from the data.

(iii) a final effect is that the NIC3 flux, measured exposure-to-exposure, seemingly changes (say for a constant source), but that these changes prefer to live in "seven" anomalous states. This gives the time measurements a non-Gaussianity, that for bright stars, can have a level similar to the random noise, and when unnoticed, can lead to larger than necessary scatter and error estimates. An explanation for this effect is beyond the scope of this paper. However, this effect is common-mode across the imaged spectrum, and can easily be estimated and removed without significant noise penalty.

Our data analysis methods are tailored to cope with the very specific problem of high signal-to-noise spectroscopy of exoplanets. The analysis has two steps, the first being an application of an overall normalization to remove the periodic effects described previously in (ii). Inherent is the assumption that flux changes intra-orbit systematic are small and periodic enough, that they can be normalized with an averaged out-of-eclipse orbit. The second, more involved step, tackles the sum of orbit-to-orbit effects described in (i).

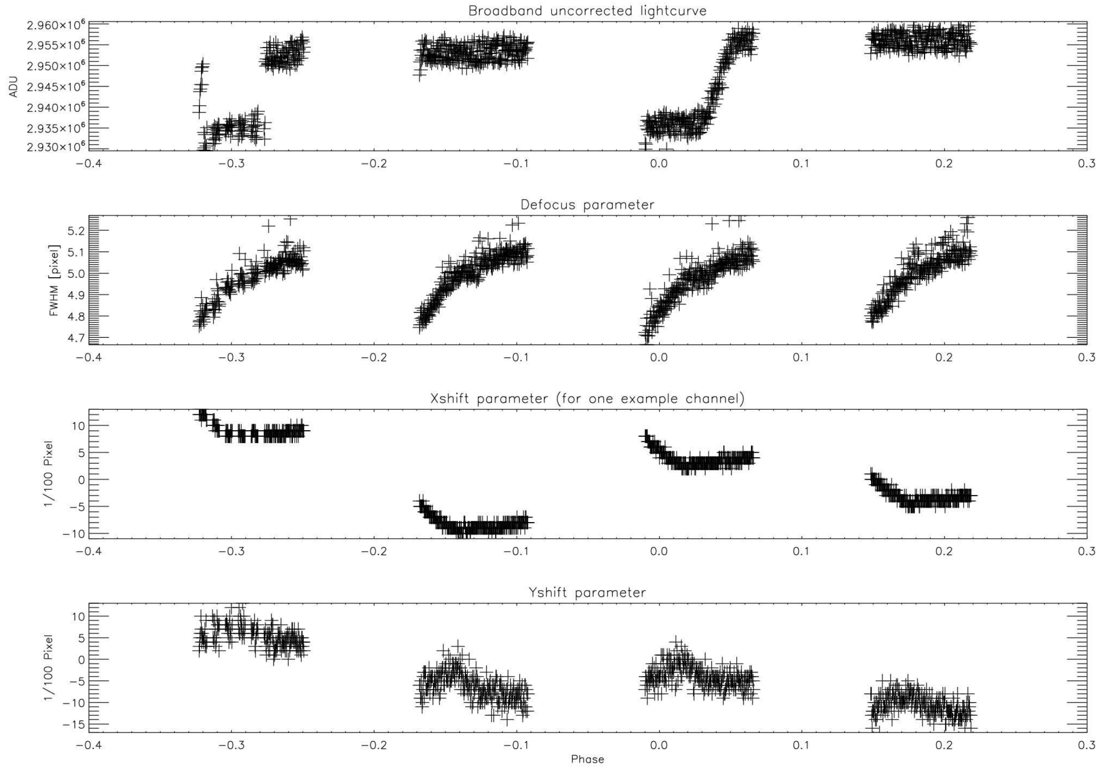

Figure 3.1.: Broadband light-curve for GJ436b (top) - note the effects in first orbit that HST-NICMOS observations are known for. Plots showing the observational parameters of defocus (2nd from top), shift in spatial direction (3rd) and shift in spectral direction (bottom). Two effects can be clearly seen: one is the absolute offset between the orbits, the other is the 'in-orbit' systematic variation of those parameters. The defocus/FWHM parameter varies for about half a pixel per orbit, while the offsets between the orbits are about 0.05 pixels. The relative shifts on the detector are about 0.05 pixels per orbit and can be up to 0.25 pixel between the orbits for this particular data-set.

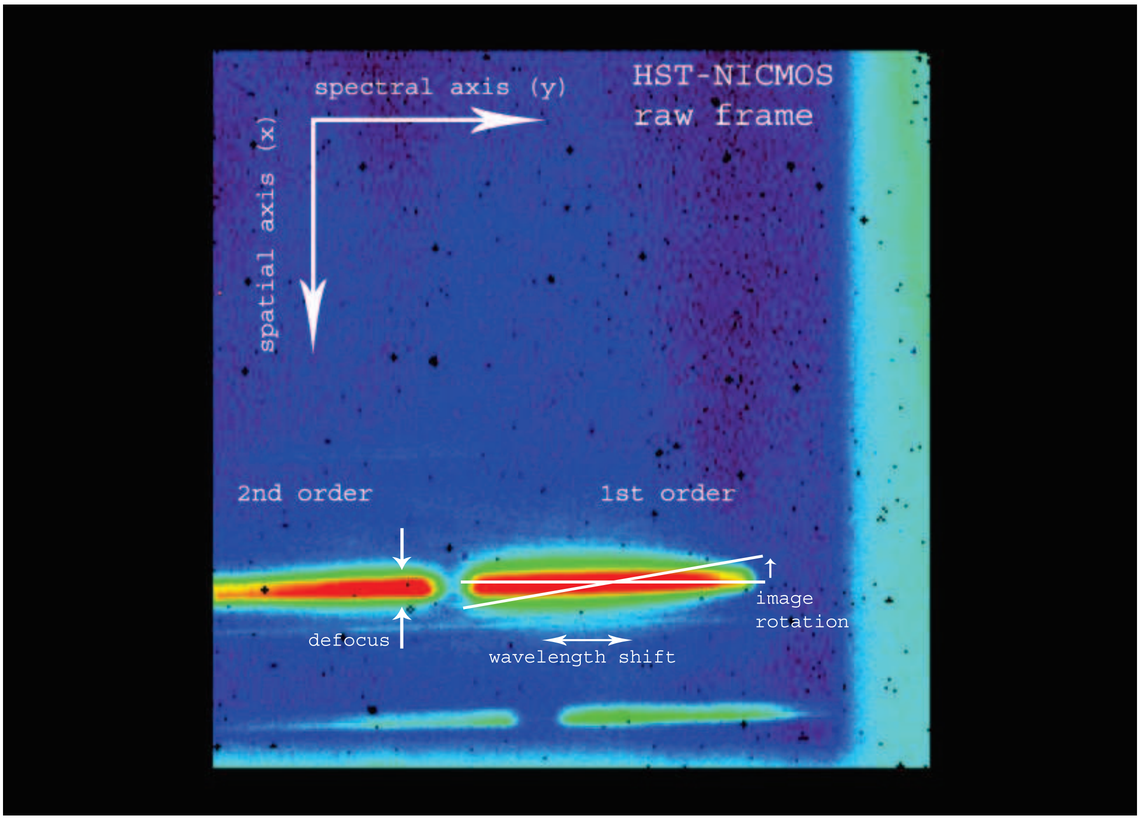

Figure 3.2.: Example for a raw science frame taken with the HST-NICMOS instrument. Note the labels that define the axis. 1rst and 2nd order were added up. The effect of image motion is illustrated.

3.3.1. Data preparation

The reduction starts from the time series of image files processed by the STScI DRP to include all NICMOS standard reductions except flat-fielding, i.e. the so-called CAL extension output. As a first step, I generate an observation-specific flat-field taking into account the color of the illuminated pixels. I use a set of recent on-orbit flats to fit the wavelength dependence for each pixel as a quadratic function over wavelength. I establish the wavelength for each column of the observation from the calibration exposures and extract the resulting quadratic at the appropriate wavelength by column and apply this correction to the observations. I note that a flat-field correction might be considered optional for differential photometry, since I am only interested in differential changes in time. But as there are small offsets between different exposures, good flat fielding reduces sensitivity to the coupling between detector response variations and image motion; that is, effective flat-fielding can remove the effect of detector response variations on spatial scales larger than a pixel. Finally, I correct the few bad pixels in the spectrum using nearest neighbor interpolation, and perform a careful background correction by fitting unilluminated regions adjacent to the spectrum.

With the data now homogenized after the normalization, I derotate and shift the spectrum to place all exposures in a common 2-d, pixel based reference frame. The rotation and shift operations necessarily require interpolation. However, tests show that the interpolation noise introduced is smaller than the shot noise in the spectra, and therefore, has indiscernible effects on the final planetary spectrum. A spatial mask is applied, and spectra are extracted by summing in the spatial direction. When both the first and second order of the grating are imaged onto the detector, signal from both orders can be co-added (after correction of systematics) for improved signal-to-noise. As a last step in the extraction, I determine the image motion in the direction of dispersion by identifying differential shifts from the edges of the G141 filter transmission.

Furthermore, I assume that the light curve behavior can be described by perturbations which are linear in these variables. It is clear from figure 3.1, that the position and angle of the spectrum on the detector in the first orbit differs strongly from the other orbits. I therefore exclude the first orbit data as a standard precaution in any further analysis, since the linear approach could work poorly for these data. Following Swain et al. (2008), I correct for instrumental systematics based on the behavior of the optical state vectors, the orbital phase and its square and the temperature of the detector. I do this by using a downhill-simplex method to minimize the residuals in the light curve. I tested the difference with a Gauss-Markov method (as in Swain et al. 2008) and find that both methods provide similar results, but a downhill-simplex method is easier to customize and faster. The standard approach of the pipeline is to do a joint decorrelation of the in and out of eclipse data, although it is also capable of the approach used in Swain et al. (2008) where an instrumental systematics model is derived from the out-of-eclipse data and interpolated to the in-eclipse section. In the joint decorrelation approach, I provide orbital parameters to the code and it will generate results for the free parameters. The approach is to compute the corrected light curve for trial decorrelations of the instrument systematics and trial model light curves. Minimizing the power in the residuals yields the desired parameters (e.g. planetary radius). I note that the decorrelation algorithm has the ability to extend the number of state vectors and to do a multi-parameter light curve modelling. Our strategy is, however, always to use the minimum number of variables possible, not to include non-causal parameters or to do over fitting.

Defining a wavelength array. The applied defocus reduces the native resolution of the spectra from $R \simeq 200$ to $R \simeq 40$, therefore one can define a wavelength channel at a reduced resolution by summing in the dispersion direction. Instead of constructing channels of equal width, as other investigators have done, I choose a different method. The transmission curve of spectra show irregular peaks and valleys. I sum the spectra by integrating the flux between adjacent transmission valleys. The reason is as follows – image motion along the dispersion axis (Y-axis) affects the photometric quality of channels that lie at locations where the local gradient of the transmission function is large. By choosing to define channels by adjacent transmission valleys (the local gradient being zero at the bottom of the valley), I prevent flux cross-talk between adjacent channels in the event of Y image motion. By adopting this procedure, I construct a total of 13 channels spanning the total wavelength range, with widths w_y ranging between 7 to 17 pixels, and resulting in an average $R \simeq 30$ which is close to the maximum resolution of 40 possible in the DEFOCUS mode.

I tested the analysis using alternative wavelength arrays shifted 5 pixels in either direction. These clearly show that define the array using transmission minima minimizes systematic noise introduced by shifts in wavelength direction to the extent that small shifts in the Y-axis can be ignored in further processing.

Deriving decorrelation parameters. Each wavelength channel, λ_i, has associated with it a $\simeq$ 900 sample long photometric time-series. Each individual time-series is corrupted by systematics and cannot as such be used to fit model light-curves to derive the transmission spectrum of the planet. These systematics have two primary causes, (i) the image motion of the spectrum on the NICMOS focal plane array, which has response variations on all spatial scales and (ii) a change in the instrumental PSF. The former are mitigated by color dependent flats, however, these are imperfect for the purposes of the type of precision differential photometry that I are interested in.

The total instantaneous flux detected in an channel, λ_i, is a 2-d spatial integral of the region of interest of the product of the imaged optical intensity and the detector response. In case of image motion, i.e. small displacements δx and δy, the detected flux can simply be expressed as a 2-d convolution of the aforementioned two quantities. In our case, the illumination is in the form of a spectrum, and as a result displacements δy along the dispersion axis are spatially averaged and mitigated by the choice of channel boundaries (as described above) and are of secondary importance. As a result, image motion along the spatial direction, X, causes a bulk of the systematics.

It is worth discussing the amplitude of the image motion, δx and δy. As mentioned before, the largest motion during the course of the observation is a rigid rotation of the spectrum with respect to the detector. Therefore, for a channel, λ_i, a mean distance of l pixels from the rotation pivot, $\delta x \simeq l\delta\theta$ and $\delta y \simeq l\delta\theta^2/2$. Hence, for a small rotation $\delta\theta$, $\delta y << \delta x$. In reality, rotation is not the only image motion – there is also pure translation of the spectrum. In our data, the total motion in the spatial direction is however dominated by the rotation of the spectrum. In the dispersion direction, it is dominated by the translation which severely effects the quality of the photometry at the band edges where the flux rolls off rapidly. Elsewhere, it is unimportant.

What is the amplitude of the image motion required to produce photometric errors larger than the sought after signal? This is an involved question. In principle, the defocus of about 5 pixels FWHM should provide sufficient averaging against sub-pixel image motion. However, in reality this is not enough. The act of defocussing the instrument, using the so called pupil alignment mechanism (PAM) within NICMOS, leaves diffractive ringing in the shape of a monochromatic PSF on scales of λ/D (in our case, this scale is just smaller than the size of a single pixel of the detector). Even image motion at the level of ~ 0.1 pixels causes photometric changes that are larger (e.g. 5×10^2 ppm) than the signal I wish to detect ($\sim 2 \times 10^2$ ppm). *This is the main reason that I have to cor-*

rect for the effects of image motion and PSF changes at level of a few one-hundredths of a pixel.

I derive the values of δx and δy using averaged templates cross correlated with individual spectra. Motion δx obviously depends on the wavelength channel given that it is dominated by rotation, whereas δy is identical for all channels. In order to derive δy the parameter for translation in the dispersion direction, or δx spatial direction on the detector (see fig. 3.2), each exposure was collapsed in both directions to derive an averaged filter function in spatial as well as in wavelength direction. Computing cross-correlation-offsets on these filter functions in the two directions for the $\simeq 900$ exposures, provides the vectors of decorrelation parameters. These vector parameters (see fig. 3.1) are estimated to roughly 0.01 pixels scale. This method of estimating image motion from data templates is superior (near optimal) to say using Gaussian-fits in the spatial direction (X), because the spectral profile along X cannot be described by an analytical function (let alone a Gaussian). The parameter D_{focus}, which captures the telescope focal breathing (i.e. the change in the PSF, with the FWHM increasing non-linearly towards the end of each spacecraft orbit), was defined by the FWHM of the collapsed PSF in spatial direction for each frame (see fig. 3.1, 2nd from top).

Matrix-correction of 'intra-orbit'-systematics. These systematics are periodic with the spacecraft orbital frequency, and I remove them right at the start of the decorrelation. This step can be explained using a matrix formulation. Assume that our NICMOS time-series data can be expressed as a matrix O. Its two dimensions are orbital phase ϕ (time after start of the nth orbit $t - t_{0,n}$) and wavelength λ. Each element of the orbital matrix O then describes the signal $S(\lambda_i, \phi_j)$ in a particular wavelength channel λ_i at a particular orbital phase ϕ_j :

$$O = \begin{vmatrix} S(\lambda_1, \phi_1) & ... & S(\lambda_1, \phi_j) \\ ... & ... & ... \\ S(\lambda_i, \phi_1) & ... & S(\lambda_i, \phi_j \end{vmatrix}$$

In order to correct the 'intra orbit' systematics, I define a standard out of eclipse orbital matrix O_{std} by computing an average matrix of all N out of eclipse orbits $O_{out,N}$. In these GJ436b data, I am forced to exclude the first orbit due to poor data quality ($\Rightarrow N = 2$), so that the standard matrix was an average of orbits 2 and 4.

The standard orbit O_{std} was derived by computing a mean of all N out-of-eclipse orbits:

$$O_{std} = \frac{1}{N} \sum^{N} O_{out,N}$$

To correct each of the all N out of eclipse orbits $O_{out,N}$ and the one in eclipse orbit O_{in} for orbital systematics, their matrices were divided by that standard orbit O_{std}:

$$O_{corr,N} = \frac{O_{out,N}}{O_{std}}$$

and

$$O_{corr,in} = \frac{O_{in}}{O_{std}}$$

Its 2d-format and the matrix calculations ensure that only data-points acquired at same orbital phase and same wavelength are compared. This turns out to be a straightforward but nevertheless powerful reduction step to correct for intra-orbit variations (see further in Error Analysis). As the photometry is now corrected for all effects correlated to the orbital phase, the decorrelation vectors δx, δy and D_{focus} must also be corrected for orbital phase related variations (see fig. 3.3). Therefore, these three vectors were also corrected by normalizing them in a manner similar to that for the photometry.

Decorrelation of 'inter-Orbit'-systematics In the previous section, I described the removal of intra-orbit effects by normalization using the 'standard' out-of-eclipse orbital matrix O_{std}. The next step, i.e. the removal of inter-orbit effects is more convoluted. It has been discussed before that these systematics result from image motion (fig. 3.2), the largest component of which is the non-repeatability in the positioning of the grism. The systematics observed in photometry *must* result from interaction of the image motion with the spatial detector response – there is no other causal reason for these systematics and I assert this to be the case; there can be temporal effects, such as quantum efficiency variations of the pixels with temperature, however the detector temperature can easily be derived assuming that each detector cell behaves as a diode – but this

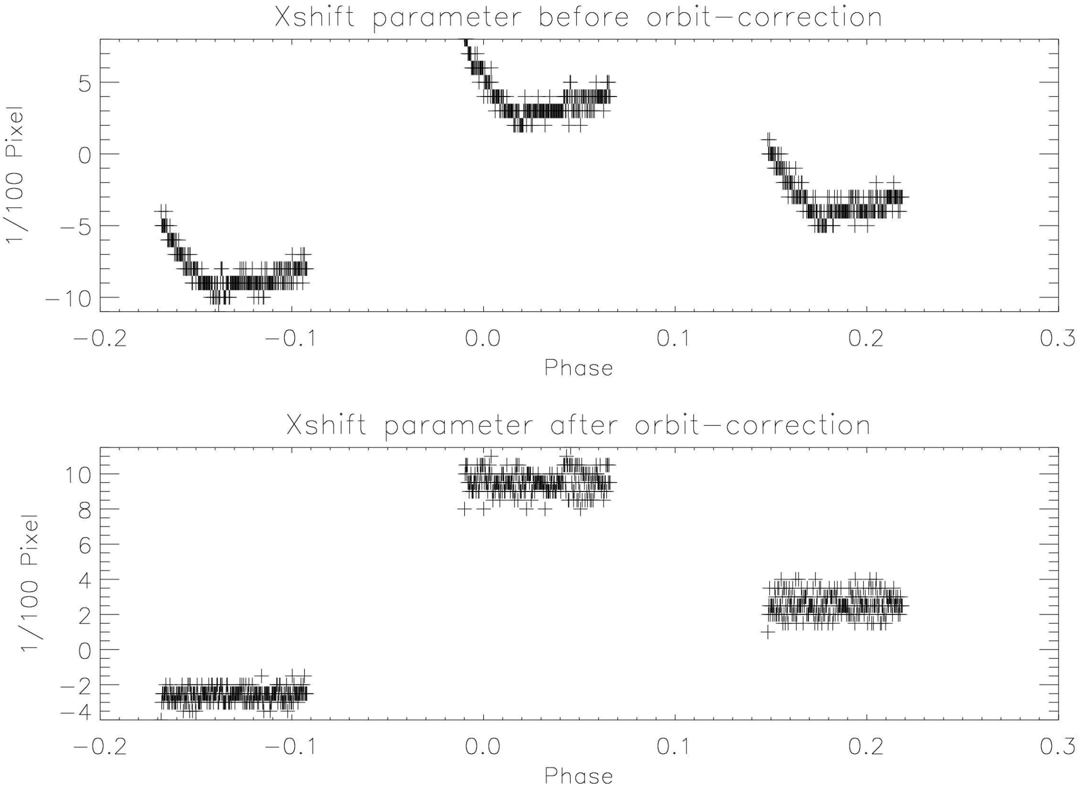

Figure 3.3.: Since the 'matrix-correction' already corrected for all effects correlated to the orbital phase, the observational parameters had to be disentangle from that effect either. Here you can see this correction for the x-shift parameter. The absolute offsets between the orbits as well as a very small noise level inside one orbit of about 3/100 pixel remain.

temperature does not show significant correlation with the photometric time-series.

Even a fraction of a pixel image motion results in a systematic shift in the detected flux. The is because of the interaction of (unresolved) structure in the PSF interacting with intra-pixel response; the response of a NICMOS detector pixel rolls off significantly at the pixel edges due to the reduced probability of "detection" of the electron-hole pairs created in the region. If the total peak-to-valley image motion around the mean location is less than about 0.1 pixel, the variations in the detected flux can be well described as linear in the motion vector. This is generally the case with grism G206 (1.45-2.55 microns) observations. Performance with G141 is generally degraded – this particular data-set shows repositioning errors at the edges of the spectrum (furthest away from the pivot of rotation) of up to 0.25 pixels (fig. 3.1). For these data, the flux cannot be described as linear in image motion alone. The *modification* I make is as such: if the detector flux can be described as a Taylor expansion in image motion and PSF variation, then I include terms in the Taylor series up to second order. Second order terms are proportional to terms such as, $(\delta x)^2$, $(\delta y)^2$, D^2_{focus}, and cross terms such as $\delta x \delta y$ etc. Judicious choice of channel boundaries minimizes effects due to $(\delta y)^2$ and its cross terms. The removal of intra-orbital periodic and quasi-periodic systematics in the previous step ensures that D_{focus}, D^2_{focus} and its cross terms are no longer significant.

Therefore, the photometric systematics resulting from image motion can be simplified to

$$F_{model} = 1 + c_1 \cdot \delta x + c_2 \cdot (\delta x)^2 + c_3 \cdot \delta y$$

This three parameter (c_1, c_2, c_3) model is a vector. I then take inner product of this with a vector describing the theoretical light curve to generate a combined model which is subjected to a joint least-squares analysis to determine the full set of unknown parameters, i.e. the sensitivities to image motion (c_1, c_2, c_3), as well as the astrophysical quantities derivable from light-curve fitting.

Transit light-curve fitting. For the analysis of primary transit light-curves, even in the near-infrared, a careful treatment of the limb-darkening is needed. In order to extract a transit depth for each wavelength channel, a transit light-curve was fit using the prescriptions in Mandel & Agol (2002). If the limb darkening were unknown, a primary transit model expands to relatively large set of unknown parameters. Therefore, I affixed the set of coefficients μ_i that describe the limb darkening (Mandel & Agol, 2002). Herein, I used the limb darkening coefficients μ_i (1.533, -2.234, 1.913, -0.643) used by Pont et al. (2009).

Inclination, the transit time offset and broadband transit depth were the free parameters in a first quick fit of the broadband light-curve, conducted using a standard simplex (Levenberg-Marquardt) technique. Thereafter, the inclination and the transit time offset are fixed, where as the broadband transit depth is used as a starting point for the channel-wise fits needed to derive the transmission spectrum. The channel-wise fits use just four free parameters per channel, i.e. the sensitivities c_1, c_2, c_3 and the transit depth (or planetary radius) at that wavelength.

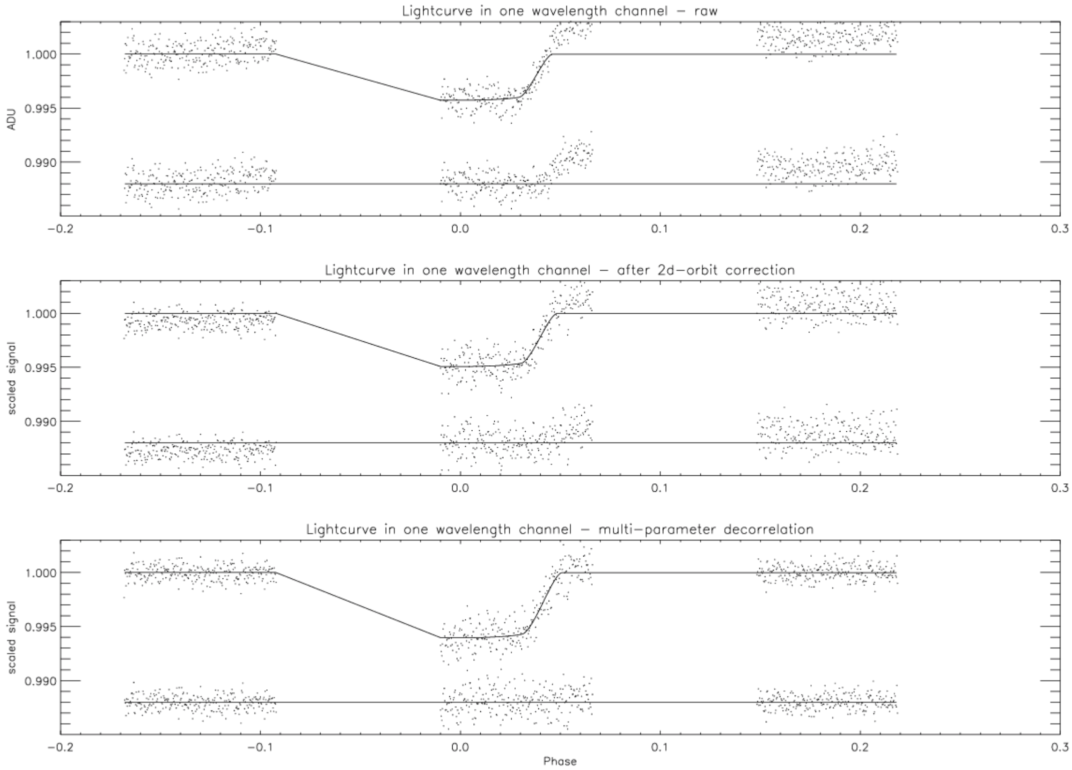

Figure 3.4.: Light-curves and fit-residuals in an example wavelength channel at different stages of the reduction. Top: raw light-curve, middle: after 2d-orbit correction, bottom: final after all corrections. See the strong orbital offsets in the residuals in the raw residuals that are corrected towards step two. Systematic offsets between the orbits are still visible in the residuals of the middle curve but are completely corrected after the final steps (bottom). See also how the overall noise level gets better (lower standard deviation of residuals from 2-3).

The transmission spectra obtained with this method (fig. 3.13), are transit depths fit for each of the i=13 wavelength channels. The next section details the calculation of the formal errors in the derived spectrum. The subsequent section describes an analysis of the resulting spectrum, that excludes Rayleigh scattering of H and He in the upper atmosphere of GJ 436b.

3.3.2. Error analysis

The modelling and removal of photometric systematics is necessary to achieve the precision required for searching for molecular features in the transmission spectrum of a planet such as GJ 436b. I now evaluate the formal errors on the transmission spectrum, and show that I am nearly detection noise limited.

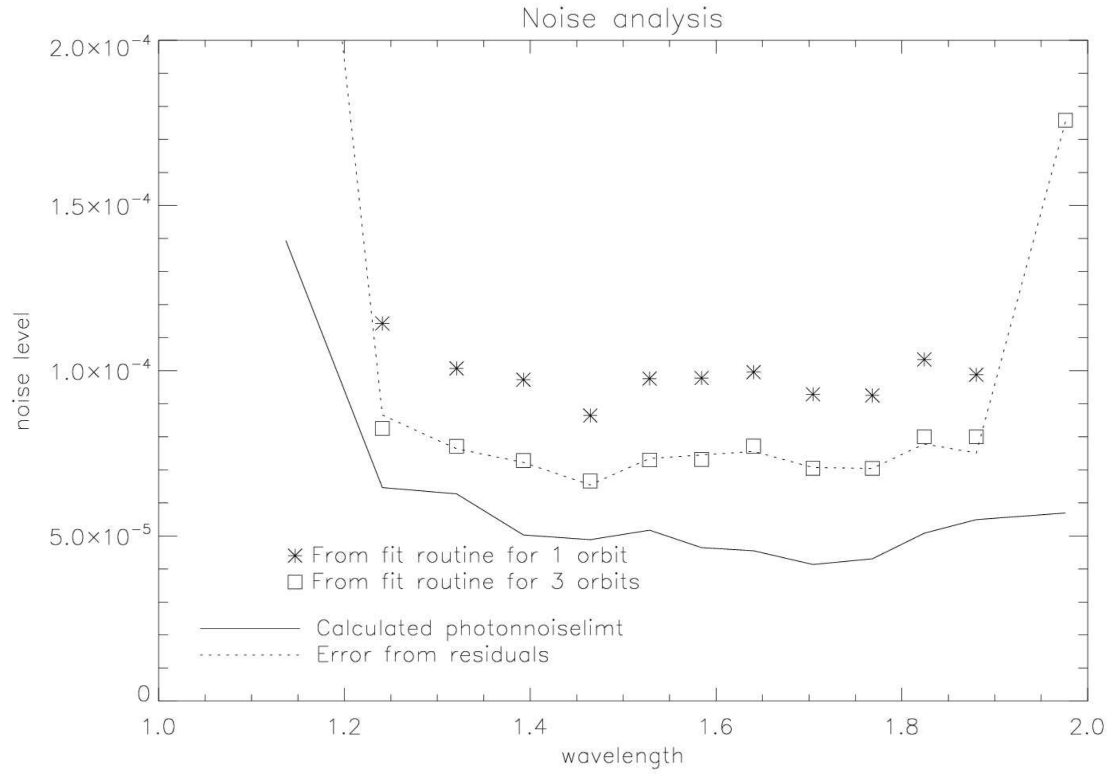

Figure 3.5.: Noise analysis for the observation. Estimated photon-noise limit (solid line), statistical error of the fit-residuals (dotted) and errors given by the fitting routine for the fits of the 252 bins of 1 orbit (stars) and using all 736 bins of 3 orbits (squares).

The statistical errors after decorrelation, of each of the channel light-curves λ_i was derived by dividing the standard deviation of the residuals by the square root of the number of used data-points m (minus the number of fitting parameters p, which can be ignored as $m >> p$), and are consistent with the errors output directly by the fitting routine's build-in error analysis (see fig. 3.5). The noise on transmission measurements (N_t) is then:

$$N_t = \frac{stddev(residuals)}{\sqrt{m}}$$

I analyze the fit residuals for remaining non-white errors using Fourier methods. The residual vectors, being unevenly sampled in time, are analyzed using Lomb-Scargle periodograms (LSPs).

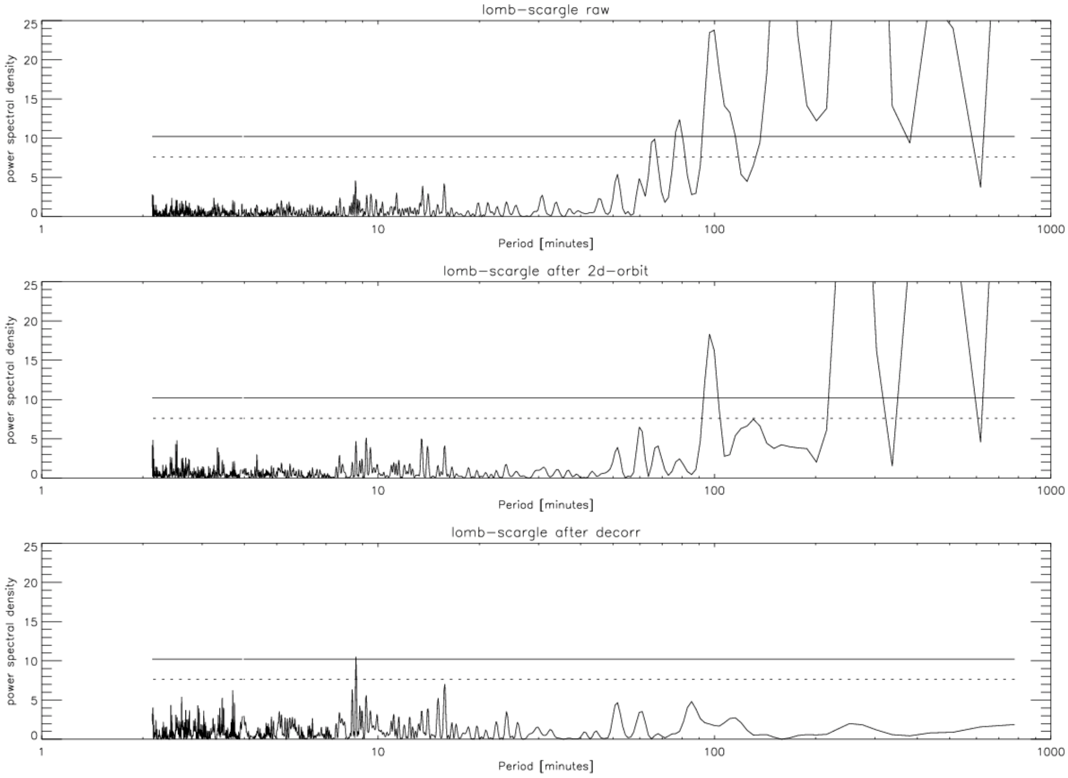

Figure 3.6.: Lomb-Scargle periodograms of the residuals in figure 3.4 at the three different stages of the reduction (raw, after 'matrix' correction and final). 50 percent (dotted) and 95 percent (solid) significance levels are over-plotted. The 'matrix' correction works well in taking out the periodic signal at 96 minutes (middle), the length of an HST-orbit. The final residuals (bottom) after non-linear decorrelation are completely free of significant spectral power in the important periods on timescales greater than 10 minutes.

Figure 3.6 shows LSPs of residuals of figure 3.4 at the three separate stages of the data reduction (raw photometry, post 'matrix' correction for intra-orbital systematics, and final decorrelation to remove orbit-to-orbit systematics). In the progression from step 1 to step 2, it shows a clear removal of the resonant peak on a timescale of $\simeq 190$ min, a frequency coincident with the second harmonic of the spacecraft orbital period (95-96 min).

In order to check the significance of the Lomb-Scargle diagrams to check for residual systematic errors I added two different artificial systematic noise functions (see fig. 3.7) to a model light-curve with some white noise of the order of our expected noise. Error function one corresponds to the aforementioned offset between the orbits, error two to the 'in-orbit' systematic effect.

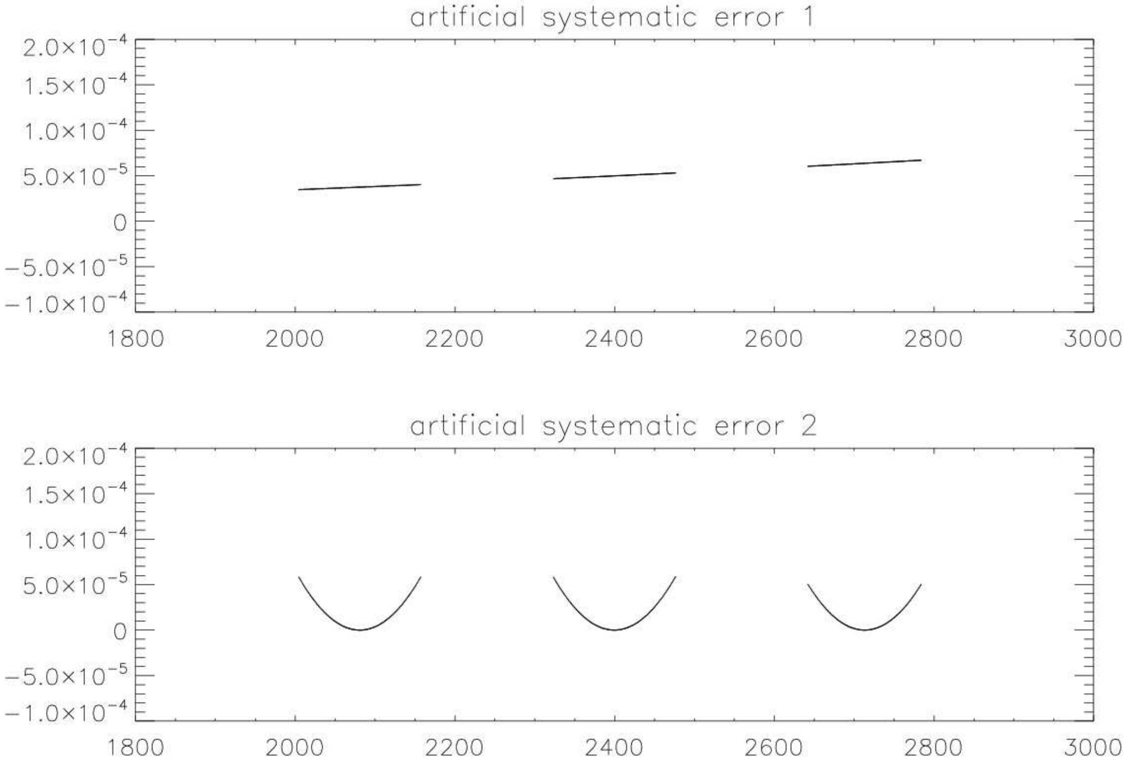

Figure 3.7.: Diagram that shows the two different noise functions used in the test. Each represent one dominant correlated noise source for the HST-NICMOS instrument: an absolute offset between the orbits (top) and an intra-orbit systematic (bottom). Both functions were scaled so that they induced an error of 0.00004 (top) and 0.00002 (bottom) in transit depth when added to the original light-curve and fitted.

In order to get an estimate for the offsets induced by those artificial systematics I first of all fitted a light-curve with white noise added at the statistical noise level and compared the resulting depth to the fitted depth when the errors were added.

The errors were scaled so that the resulting transit depth was changed for 0.00004 (for the fig. 3.7 top error) and 0.00002 (for the fig. 3.7 bottom error) due to the presence of the artificial residual systematic. After that I computed the LCP of the residuals to see the levels of spectral power introduced by the various errors added (fig. 3.8, right). This step was iterated about 100 times. It turned out that the artificial offset between the orbits almost always shows a significant peak in the LCP (fig. 3.8 middle, right). Even the in-orbit residual error shows a significant peak in more than half of the simulations (fig. 3.8 bottom, right).

This result is an argument to assume that the residual correlated error in the final result is well below the level of 0.0004 that was induced by the first artificial error. This argument is especially strong since none of the channels of the original data-set show any peak of spectral power in the periods larger than 10 minutes.

3.3.3. Testing for Rayleigh scattering

The results of this analysis will be interpreted using a full radiative-convection 1-D atmospheric model, coupled to atmospheric photochemistry and equilibrium chemistry. This model is at present in preparation and therefore beyond the scope of discussion herein. In this section I simply show that Rayleigh scattering by $H_2 - He$ can not explain for the shape of the resulting spectrum. Because Rayleigh scattering traces the entire atmosphere, a detection would have enabled a direct determination of the pressure-altitude relationship, which is required to determine the absolute fraction of other elements. Therefore, I first compute the $H_2 - He$ Rayleigh-cross-sections of He and H_2. These numbers are then used in an expression for the planetary radius as a function of wavelength for the case of purely small scattering particles in the upper atmosphere.

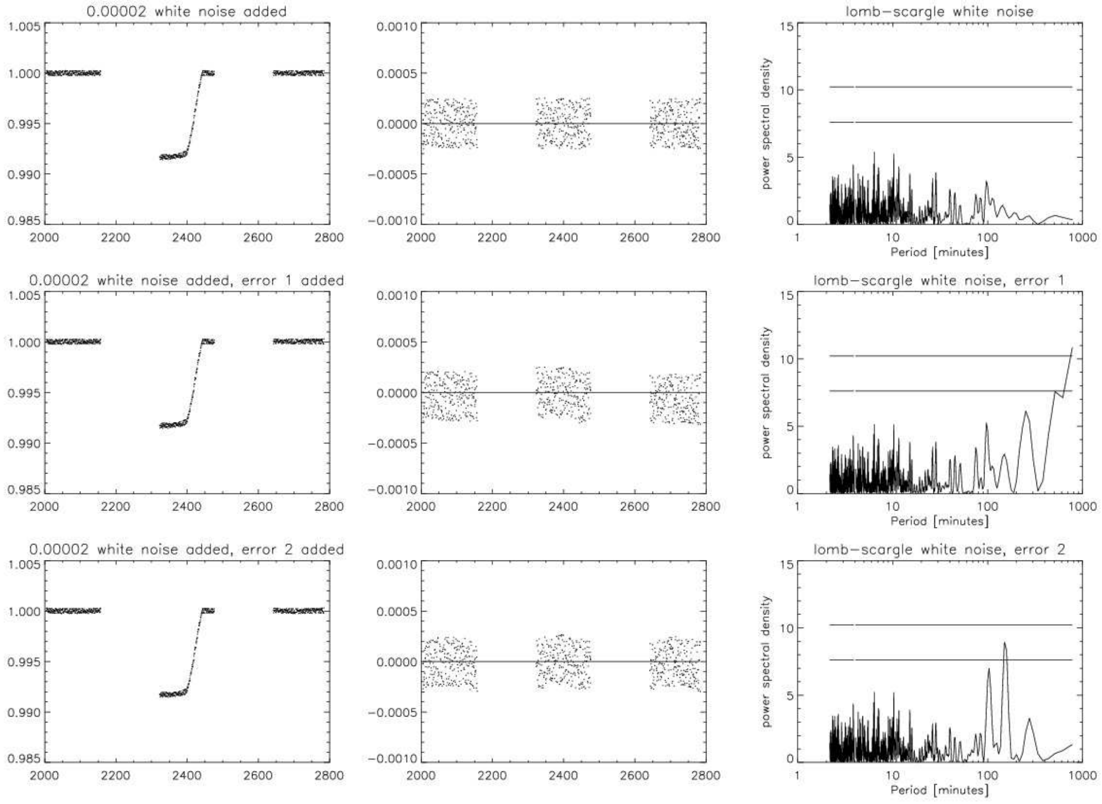

Figure 3.8.: Light-curve with white noise (left, top), error 1 (left, middle) and error 2 (left, bottom) added. Corresponding residuals after fit (central column). Lomb-scargle periodograms (LCP) of the fit residuals. The error that induces the orbit offset (middle row) showed a significant spectral power in the LCP in almost all simulated cases (middle, right). Even the in-orbit residual error shows a significant peak in more than half of the simulations (bottom, right).

Rayleigh scattering cross section

The Rayleigh scattering cross-section of an atom or molecule is (Allen, 1973) defined by:

$$\sigma_a = \frac{32\pi^3\delta}{3\lambda^4}(\frac{n-1}{N})^2 = \frac{128\pi^5}{3\lambda^4}\delta\alpha^2 = 1.306\times10^{20}\frac{\delta\alpha^2}{\lambda^4}cm^2 \quad (\lambda\, in\, \mu m) \quad (3.1)$$

with depolarization factor $\delta = (6+3\Delta)/(6-7\Delta)$ with Δ=0 for He and Δ=0.02 for H_2 (Irwin, 2003)). The polarizability $\alpha = (n-1)/(2\pi N)$ at low frequencies, (N: atoms per volume unit, n: refractive index) is $6.67\times10^{-25}cm^3$ for H and $2.05\times10^{-25}cm^3$ for He (Allen, 1973).

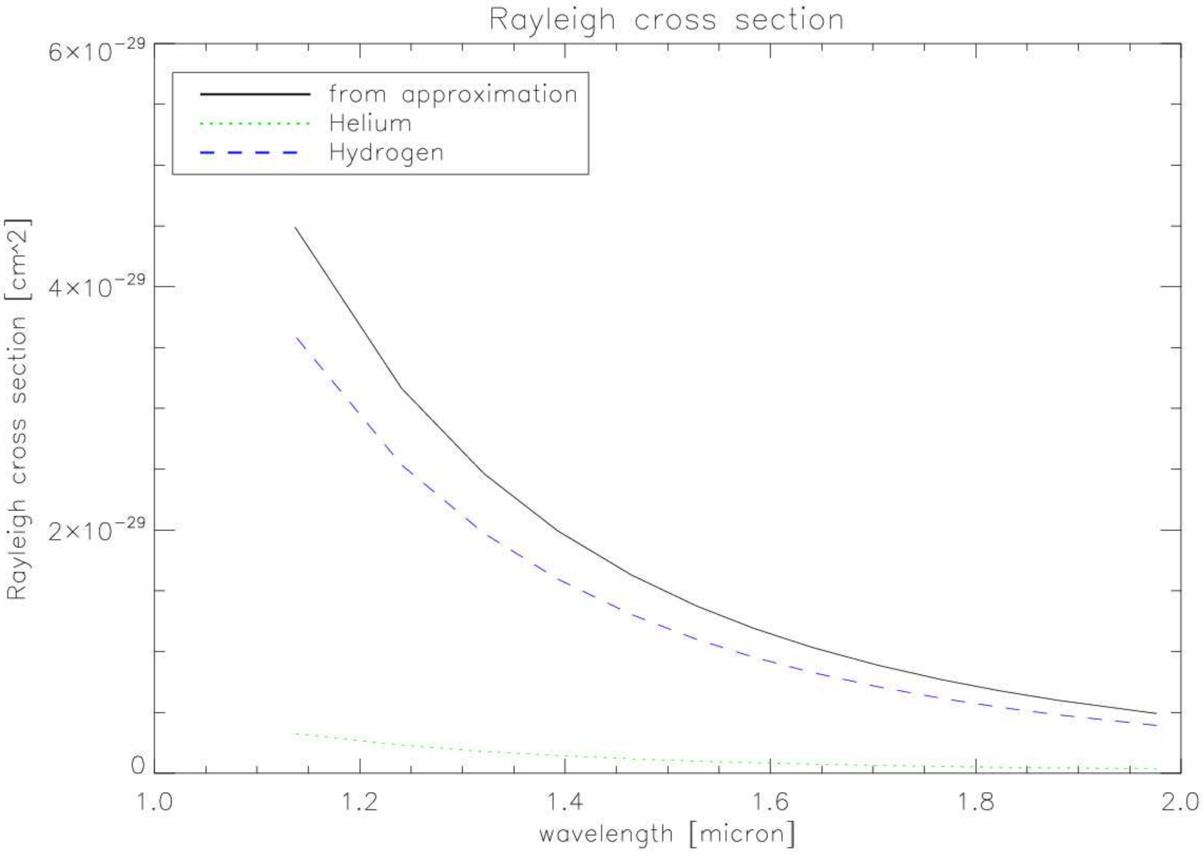

Figure 3.9.: Rayleigh cross sections for Helium (green, dotted) and Hydrogen (blue, dashed). The black line shows the result of the approximation(Atreya, 1986).

In practise for giant planet atmospheres with composition dominated by near-solar hydrogen-helium, it can reasonably accurately approximated by (Atreya, 1986):

$$\sigma_a = \frac{7.5 \times 10^{-17}}{\lambda^4} \quad (\lambda\ in\ , \sigma_a\ in\ m^2) \tag{3.2}$$

The resulting rayleigh cross-sections for Helium and Hydrogen between 1 and 2 micron are shown in figure 3.10 together with the result of the given approximation.

Atmospheric scale height

The atmospheric scale height H of a planet is defined by:

$$H = \frac{kT}{g_p \mu} \tag{3.3}$$

where T is the temperature, g_p is the surface gravity, and μ is the mean molecular weight of the atmospheric constituents. For GJ436b the temperature T is 712 K (Deming et al. 2007), $\mu = 2.3 \times m_{prot}$ and $g_p = 1.18 \times g$ (Lecavelier et al 2008). These numbers give a scale height of 220 km for GJ436b, about 0.6 percent of the planetary radius.

Radius difference

Wavelength-dependent differences in the effective cross section of the scatterers cause the planet to appear of different size in these wavelengths. This also causes different transit depths in these channels. The variation in apparent planetary radius in this case is given (Sing 2009 referring to Lecavelier 2008a) by:

$$\Delta R_p(\lambda) = R(\lambda_0) - R(\lambda) = H \times ln(\frac{\sigma(\lambda_0)}{\sigma(\lambda)}) \tag{3.4}$$

Fig. 3.10 and 3.11 show the expected shape of the spectrum in case of the presence of rayleigh scattering in comparison with the resulting spectrum. It is obvious that the $\sim \lambda^{-4}$ shape of the rayleigh scattering spectrum does not match the results of my analysis(see fig. 3.10). Even for an unrealistic atmospheric scale height H of 50km (see fig. 3.11), the agreement is only marginal.

3.4. Results

In this chapter I show that the presented data reduction method is suitable for HST-NICMOS-spectrophotometry. In fact, the method shows satisfactory performance with data of medium quality, i.e., relatively large orbit-to-orbit photometric offsets, and relatively incomplete coverage of the transit light-curve coupled with low coverage of the baseline.

The average radius of the planet as a fraction of the stellar radius R_P/R_S is 0.08277 ± 0.00038 for the first visit and 0.08241 ± 0.00042 for the second visit (see fig. 3.12). This translates to 25693.7 ± 84.9972 km or $4.03292 \pm$

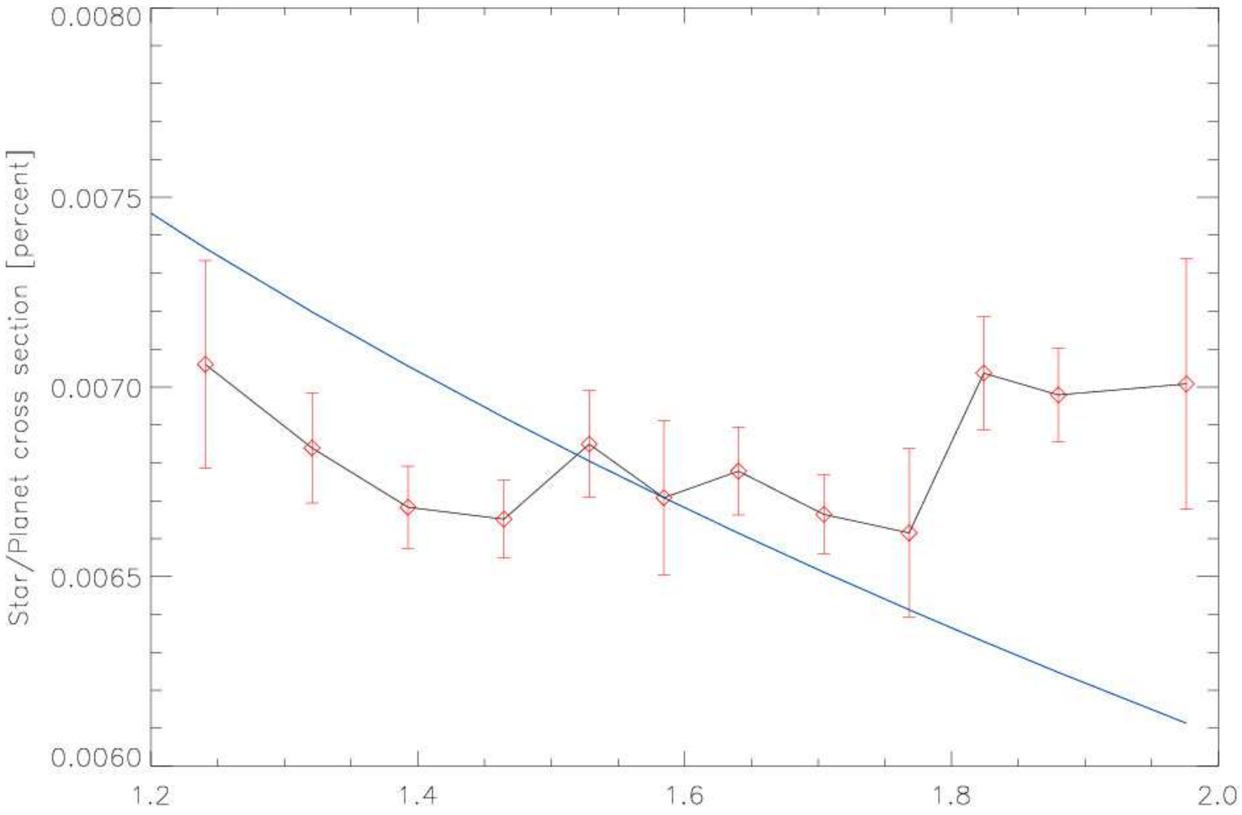

Figure 3.10.: Star/planet ratio averaged from two resulting spectra (red). Blue curve shows Rayleigh scattering. For smaller scale height this curve gets less steep.

$0.0133413\ R_{Earth}$ for visit one and $25582.2 \pm 95.3493\ km$ or $4.01542 \pm 0.0149661\ R_{Earth}$ for visit two. The error in the averaged radius is about half of the atmospheric scale height.

I have presented a consistent near infrared spectrum of GJ436b for both visits and using almost the complete wavelength range of the G141 grism (fig. 3.13) from 1.3 to 1.9 micron. The resulting spectra are flat within the error-limit. No features were observed down to a level of $2 \cdot 10^{-4}$. Especially the predicted signature from water absorption at 1.4 micron, could not be observed in either visit. In is not observed even when the spectra of the two visits are averaged. The flat shape of the spectrum also excludes a radius set by scattering from small particles such as molecules of hydrogen and atomic helium (see 3.3.3). There is no evidence for any kind of significant variability in the planetary signal between the two

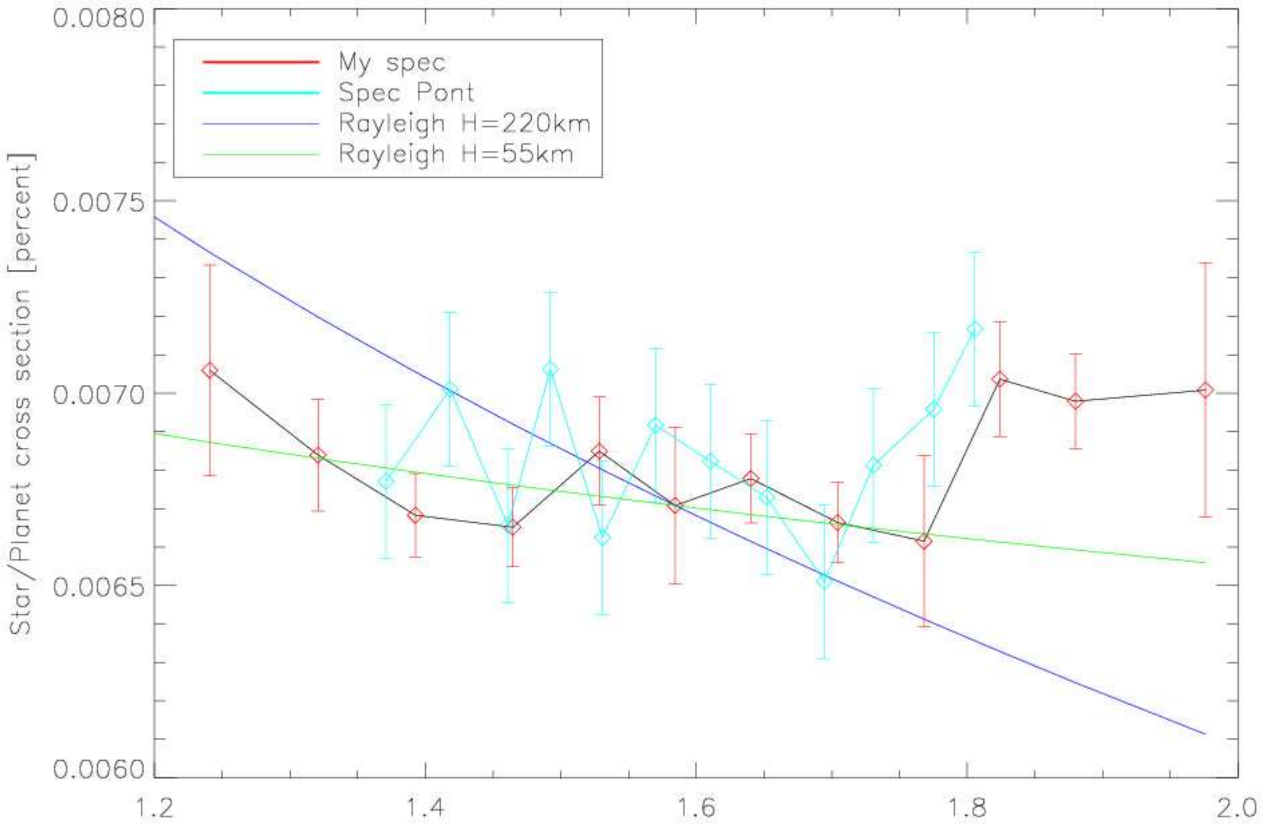

Figure 3.11.: Same as 3.10. With the spectrum of Pont (2009, light blue) and a Rayleigh model for H=55km (green). It is obvious that the $\sim\lambda^{-4}$ shape of the rayleigh scattering spectrum does not match the results of my analysis. Even for an unrealistic atmospheric scale height H of 50km, the agreement is only marginal.

visits down to the same level of some 10^{-4}. The $\sim 1\sigma$ differences between the two visit at 1.575 and 1.775 microns are probably statistical.

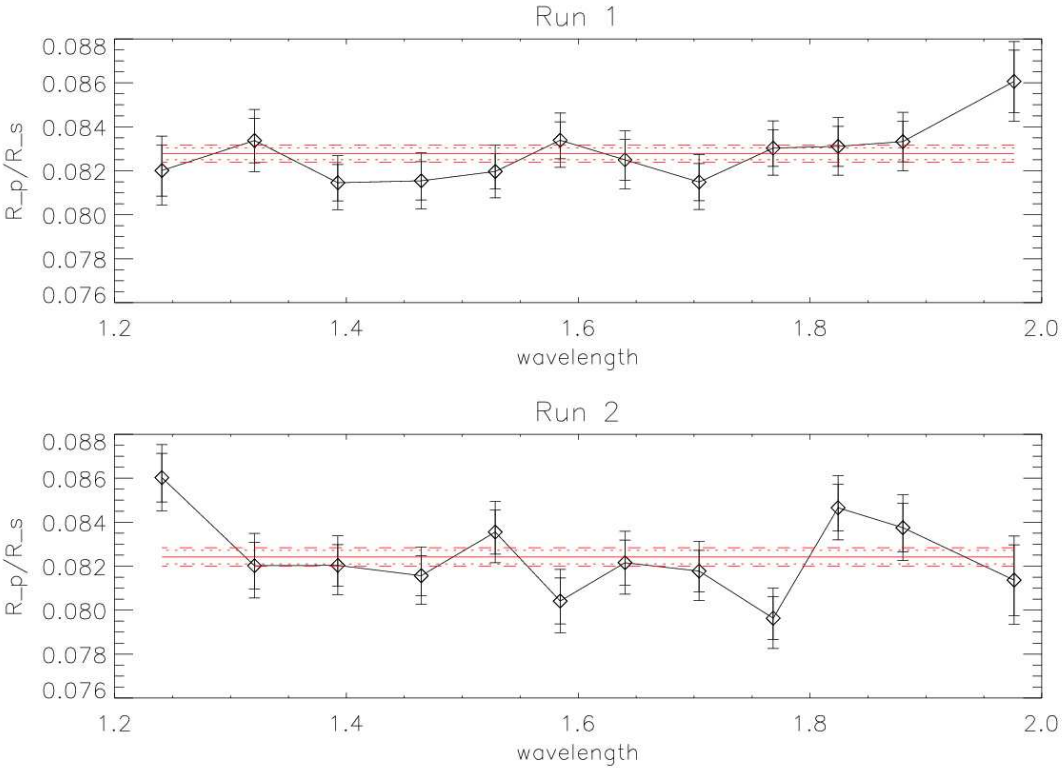

Figure 3.12.: Derived spectra for the two observations of GJ 436b (top: Visit 1, bottom: visit 2). The shorter error bars represent the random error only, the longer error bars have the derived limit for the systematic error added (see 3.3.2. The red solid lines show the average R_P/R_S for both visits (dotted: rand. err., dashed: rand.+ syst. err.))

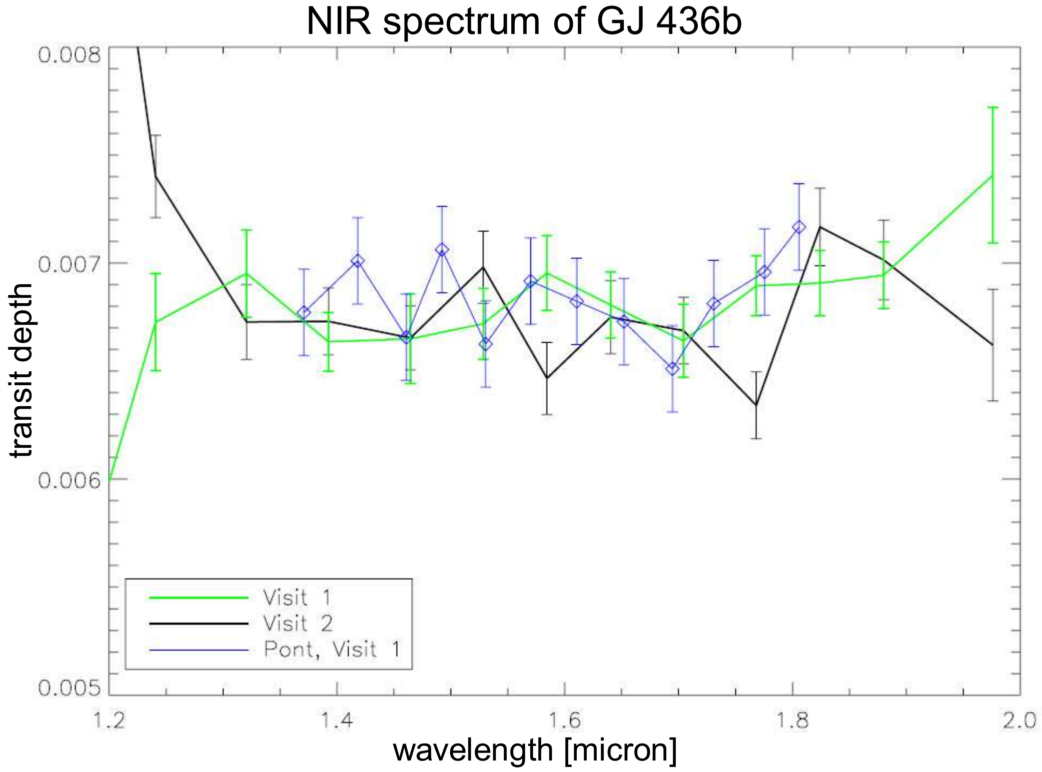

Figure 3.13.: Derived spectra for the two observations of GJ 436b (green: Visit 1, black: visit 2). The results of a previous analysis by Pont et al (2009) is plotted in blue.

4. Airborne-based: Observing extrasolar Planets with SOFIA

In this chapter I present an analysis of possible science cases for NASA's Stratospheric Observatory for Infrared Astronomy (SOFIA) in the field of extrasolar planet detection and characterization. Advantages of SOFIA and its instruments for exoplanet observations are illustrated and possible targets introduced. Possible future instrumentation is discussed.

4.1. Introduction

4.1.1. SOFIA - general advantages

Even the very close-in extrasolar planets, with distances to their host star of only a few stellar radii, are not much hotter than $T_{eff} \simeq 2000$ K. Therefore the equivalent black-body emission always peaks in the infrared. Depending on the temperature, which is closely connected to the planet's major orbital axis, this peak is located in the near infrared (NIR) for highly irradiated gas giants or in the mid to far infrared for exo-earths in the habitable zone. For example the planet to star contrast ratio of a Hot Jupiter like HD 189733b is a few 10^{-5} in the optical but increases to 10^{-3} in the near infrared. From this perspective SOFIA operates in the optimal wavelength regime for exoplanet observations (see fig. 4.1 for various targets).

For short-period close-in transiting planets with transits occurring every 2-4 days, the optimal observing schedules for ground-based transit observations are reduced to only few nights per year for a given observing site as the event is best observed close to target culmination and local midnight. One possible strategy is shown in figure 4.2, top. For the Hubble Space Telescope (HST) the situation is reversed: It is able to observe transits at many more opportunities but is limited to series of 96 minute

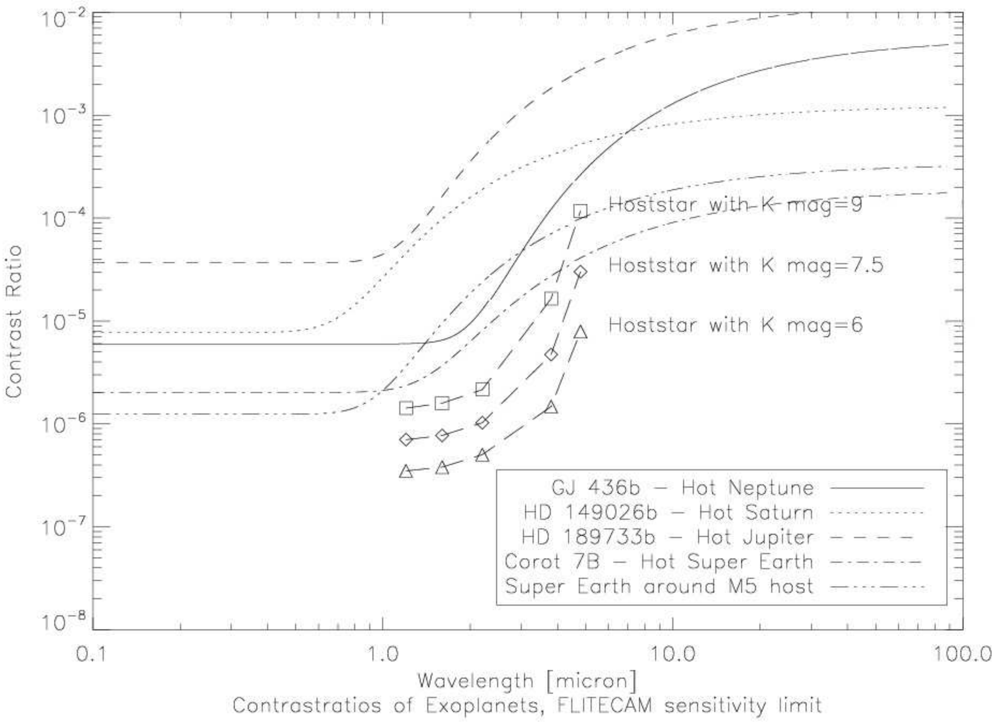

Figure 4.1.: Expected contrast ratios for different 'prototypes' of extrasolar planets. (See legend for details). From this perspective SOFIA operates in the optimal wavelength regime for exoplanet observations. The symbols in the center show the photon/background-noise limit for a 60 minute observation in the 5 imaging bandpasses of the FLITECAM instrument assuming host stars with apparent K magnitudes of 6, 7.5, and 9 (triangles, diamonds, squares). The figure shows that the noise limits are well below the contrast ratios for most of the targets. Thus reasonable S/N ratios even in low resolution spectroscopy mode can be expected.

on/off-target batches due to its near-earth orbit (see fig. 4.2, bottom). Especially for transiting planets with a very long orbit (such as HD80606, see 4.2.3) and therefore long transit durations this presets a substantial hurdle. The analysis of potential flight schedules (see fig. 4.3 as an example) shows that the mobile platform SOFIA will be able to take off close to the optimal geographic location for each of those events and will be able to observe the complete event continuously and with a very stable setup (telescope elevation, airmass, g-vector etc.).

Main difficulties for NIR exoplanet observations discussed in this paper are usually not introduced by photon-noise or background contributions, since bright host stars deliver enough photons for a reasonable signal-to-noise-ratio during one transit. In fact, suppression of systematic 1/f noise, created by a varying atmosphere and by limitations of the stability of the telescope and the scientific instrument turns out to be much more important. Once the required stability has been demonstrated, SOFIA will become an important follow-up observatory for the recently launched Kepler-mission and a testbed for choosing possible targets and testing observing strategies for the JWST.

4.1.2. SOFIA compared with other observatories.

Various observations with ground-based telescopes have been conducted to test their their feasibility for observing extrasolar planets. Photometric (Henry et al., 2000) and radial velocity observations (Mayor & Queloz, 1995) were very successful right from the beginning and even ground-based imaging observations have been possible lately (Marois et al., 2008). First successful spectroscopic observations and characterization of exoplanets have just recently been demonstrated from the ground (Swain et al., 2010). The variability of earth's atmospheric transmission as well as the temporal variability of its constituents (e.g. Angerhausen et al. 2007) is the most crucial challenge, in particular when it comes to the spectroscopic analysis of molecular features in the exoplanet's atmosphere that are also present as telluric trace gases such as water or methane.

Again, SOFIA will also deal very favorably with these effects since it will be able to fly high enough to be independent of near surface processes affecting in particular the water and methane lines (see fig. 4.4) . Changes

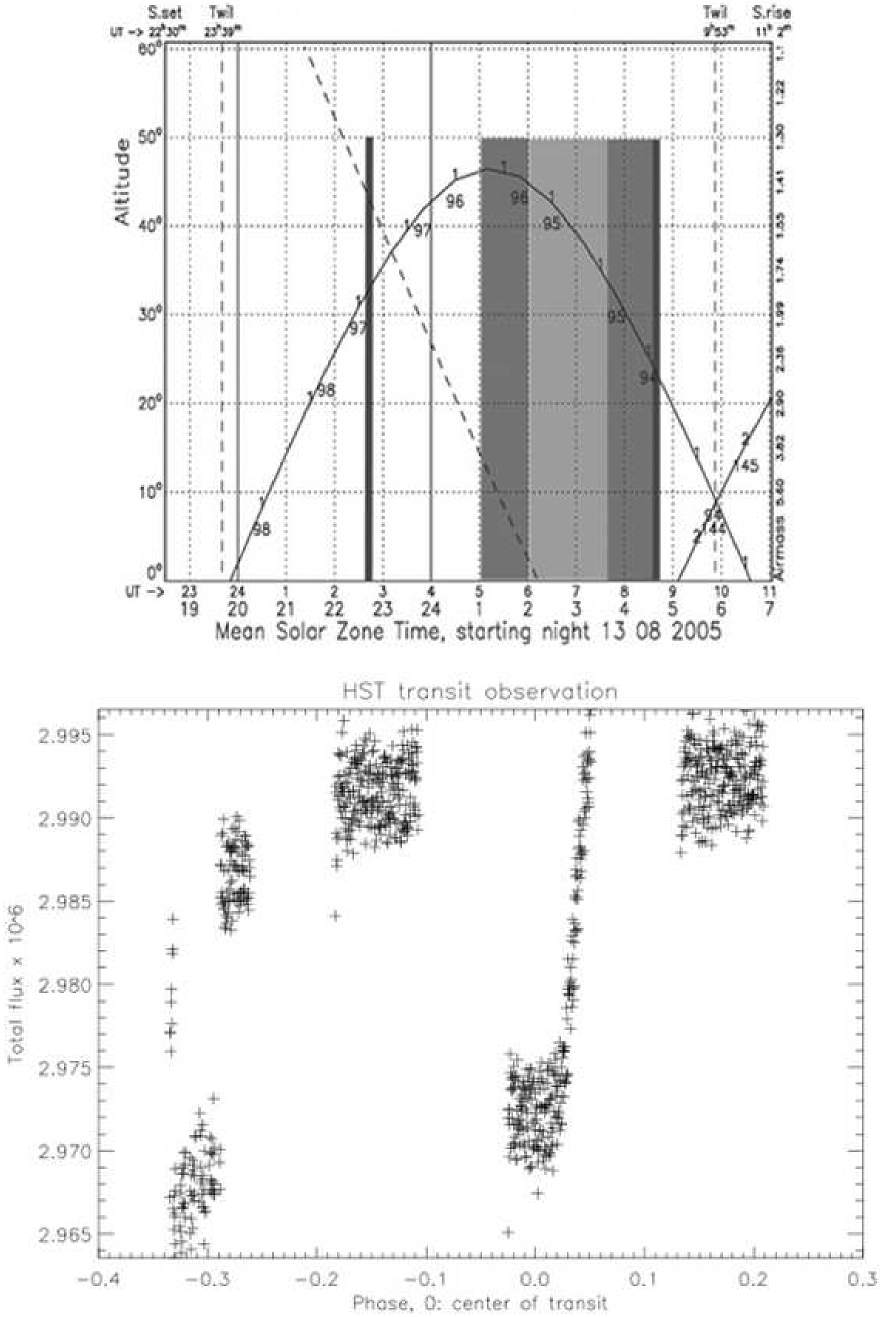

Figure 4.2.: Top: Elevation vs. time diagram of an example transit observation with SINFONI at the VLT (Angerhausen et al., 2007). Bold vertical lines represent start and end of the observation. The light grey area marks the phase of total conjunction, darker grey areas represent phases of ingress and egress. ’In’ and ’out of’ eclipse data can be observed at the same elevation/airmass. Observing condition like that are rare: generally only very few nights per year and telescope site. Bottom: Example for a photometric time-series observation of a transit of the Hot Neptune GJ 436b with HST-NICMOS. The Hubble space telescope is able to observe transits at a lot more opportunities but is limited to series of 96 minute on/off-target batches due to its near-earth orbit.

in concentration of these species cause most of the problems in ground-based NIR observations, because they vary on similar timescales as the transit-duration. However, diurnal photochemistry of molecular features high in the atmosphere on timescales of $\sim 12\ h$ and OH-emission on timescales of some minutes will still remain.

The turbulence spectrum of the remaining atmosphere in front of SOFIA is much more stable compared with ground-based telescopes. Consequently the lower scintillation and background noise as well as the reliably low and very stable extinction coefficients during such observations will provide SOFIA with a very stable environment for obtaining precise photometry over the duration of most transits (Sandell et al., 2003).

In principle the near infrared performance of the HIPO and FLITECAM instruments on board of SOFIA are comparable to the performance of the STIS and NICMOS instruments on HST. HIPO on SOFIA will be able to achieve comparable photometric precisions, making it one of the best observatories/instruments for high precision photometry at high temporal resolution (Dunham et al., 2007). At the slightly longer wavelengths SOFIA will be less sensitive than Spitzer but can work at higher angular and spectral resolutions compared to Spitzer (Roellig et al., 2009).

4.2. Science cases with SOFIA

In this section we will briefly discuss the different fields of exoplanet exploration and SOFIA's potential and limitations for these various areas. We will conclude that photometric and spectrophotometric follow-up observations during planetary transits are an excellent science case for SOFIA. In the last part of the next section we will present two example science cases with the High-speed Imaging Photometer for Occultation (HIPO) and the First Light Infrared Test Experiment CAMera (FLITECAM), incorporating the specific assets and limitations of these instruments.

4.2.1. Strategic considerations

Astronomical observations of extrasolar planets can be divided into three main categories: detection of new exoplanet candidates, confirmation of such candidates and follow-up characterization.

Detection of exoplanet candidates: Observations to find new extrasolar planets are commonly and most effectively conducted with large ground- or space-based transit- and radial-velocity (RV) survey programs. SOFIA can not compete with these surveys that are mostly executed with dedicated telescopes. Although SOFIA has the capability to detect new exoplanets, it is obvious that SOFIA is not a survey observatory and such observations will not become a major SOFIA science case.

Confirmation of exoplanet candidates: Transit surveys such as CoRoT, or the HAT and WASP programs are detecting an increasing number of planetary candidates around dwarf stars. The spectra of these planet-hosting stars are unfortunately featureless and/or just too faint in the optical, so that radial velocity (RV) follow up confirmation observations (to exclude imposers such as eclipsing or grazing binaries) have to be executed in the infrared with very high spectral resolution (up to at least some m/s). To reach these spectral resolutions it might be worth to introduce the heterodyne technique to the near infrared. Such an instrument could also be able to separate the signal of the observed planet from narrow line absorption in earth's atmosphere. Since RV-observations are time-consuming, such an instrument is operated best on a dedicated survey telescope and is not really an option for SOFIA.

In some cases SOFIA will be able to exclude imposers in transit-surveys (see photometry section) by comparing limb-darkening effects at optical and infrared wavelengths. In any case such a confirmation is just a byproduct of follow-up observations (see next) and no major science case for SOFIA either.

Characterization/follow-up observations of known extrasolar planetary systems: A variety of techniques have demonstrated their potential of characterizing already detected extrasolar planetary systems. High spectral resolution spectroscopy to measure the Rossiter-McLaughlin effect constraining the spin-orbit alignment in transiting systems is one of them (e.g Gaudi & Winn, 2007). Another is the direct imaging of already known planets at different wavelengths. Both examples are not well suited for SOFIA, either due to limited spectral resolution at shorter wavelengths (RL-effect requires $\Delta\, v\ \sim\ 5\, m/s$), limited available observing time or limited spatial resolution/telescope size.

However, the large group of photometric and spectrophotometric follow-up observations during planetary transits and eclipses will be feasible with SOFIA's instrumentation, especially with HIPO-FLITECAM. This technique and two example science cases are presented in the next two subsections. The first is high-precision primary transit photometry of HD 80606b using HIPO - the second is secondary eclipse spectrophotometry of HD 149026b using FLITECAM.

4.2.2. Transit photometry and spectroscopy

AS described in the introduction, systems with transiting extrasolar planets mostly offer two opportunities for transit observation. During a *primary transit* the planet occults the star - the broad-band transit-light-curve in this case measures the planetary radius R_p in units of the stellar radius R_*. The depth of the primary occultation is $\sim (R_p/R_*)^2$, which, for a Hot Jupiter, is of the order of $\sim 3\%$ (e.g Henry et al. 2000). At such a signal level several topics can be addressed. As already mentioned above, comparing the effect of limb-darkening in the optical and the infrared can exclude imposers in transit-survey candidates. Transit timing variations caused by additional bodies in the observed system can be detected by high-precision photometry. Ephemerides and various planetary parameters as well as information about the stellar surface such as limb-darkening or stellar spots can be drawn from photometric curves. Spectroscopic observations during the planet's passage (transmission spectroscopy) provides a measure of the relatively cool planetary terminator - the transit depth varies depending on the composition of the small atmospheric ring between day and night side that absorbs the stellar light. Here, the primary observable is the change of the effective planetary radius (i.e. $R_p(\lambda)$) as a function of color due to selective absorption of starlight along the slant geometry. Due to the slant optical depth, transmission spectroscopy probes relatively high pressure depths in the atmosphere ($10^{-2} - 10^{-4}$ bar) at NIR wavelengths. Due to reduced optical depth for small scatterers (e.g. molecular hydrogen), which can dominate at optical wavelengths (Pont et al. 2008), the NIR provides an important window for observing atmospheric composition and conditions at the terminator. The possible differences in transit depth between two wavelengths channels in the NIR, such as e.g. the methane signature detected by Swain, Vasisht & Tinneti (2008), in this case is usually in the range of a few 10^{-4} even at relatively low spectral resolutions.

During a *secondary transit* the planet disappears behind its host star. For a Hot Jupiter class planet the light missing during secondary eclipse is only about 0.3% of the stellar light in the NIR (see fig. 4.1). Secondary-eclipse spectrophotometry provides a direct measure of the planet's day-side emission/atmosphere. In the NIR, the relevant photosphere of emission lies deep in the atmosphere at pressure-depths ranging between 0.1-1 bar. The spectral features in the planetary emission spectrum are once again of the order of a few 10^{-4} in the NIR .

With HIPO and FLITECAM, SOFIA is well equipped with two (especially in combination) perfectly suited instruments for such observations. Ongoing surveys (ground-based, CoRoT, Kepler) will deliver more targets and a variety (or probably new classes) of objects in the near future.

The strategy for transit observations are usually relatively straight forward and similar to observations of standard stars, although lasting several hours. Therefore these observations might already be conducted during commissioning phase of SOFIA and its instruments. For example, test observations of the photometric stability of HIPO during commissioning can already be conducted during a transit event on the host star as calibrator. Hence, transit observations could in principle become one of the first observations with scientific output made by SOFIA.

4.2.3. Examples using HIPO-FLITECAM

In the following subsection two example observations using HIPO-FLITECAM on board of SOFIA are described in detail to provide the reader with a better impression about the feasibility of such projects. Future prospects using instruments not yet existing are discussed in §3.

One of the advantages of HIPO-FLITECAM is the ability to observe simultaneously in the optical and the IR with a dichroic beam splitter. It is for example possible, to get an independent broadband light-curve from HIPO at optical wavelengths (e.g to exclude or trace stellar activity such as starspots) as a calibrator for the spectroscopic data analysis with FLITECAM in the infrared. It is possible to use the HIPO optical light-curve to derive the necessary limb-darkening parameters, so that for the FLITECAM infrared data the only free model parameter is the transit depth.

The HD 80606b project is meant to be an example for observing long-period transiting planets with transit durations of more than 6 hours. The extremely long 12 hour transit of HD80606b is hard to cover completely, since it exceeds SOFIA's maximum flight duration. But for candidates with 6-8 hour transits, long periods and therefore rare observing opportunities the SOFIA timing and mobility advantage is obvious (see 4.1.1).

HD 149026b can serve as an example for NIR spectrophotometry of the Hot Jupiter and Hot Saturn class. Recent results (Swain et al., 2009) comparing day-side emission spectra of HD 189733b and HD 209458b, show significant differences in abundances of biogenic molecules such as water, methane or carbon-monoxide as well as differences in the temperature-pressure profiles of Hot Jupiters. FLITECAM on SOFIA can become an important tool for characterization observations of such kind in the sample of known and still to be discovered CoRoT/Kepler transiting exoplanet types. The detection limits of FLITECAM in its 5 bandpasses are shown in figure 4.1. The figure shows that the noise limits are well below the contrast ratios for most of the targets. Thus reasonable S/N ratios even in low resolution spectroscopy mode can be expected.

Photometry of HD 80606b using HIPO

The planet 80606b orbiting a G5 V parent star has the longest (111.5d) and most eccentric ($e = 0.934$) orbit of all known transiting exoplanets. HD 80606b was first discovered by radial-velocity observations (Naef et al., 2001). Time-dependent models of the atmosphere predicted temporal temperature and flux variations due to the very large planet-star distance variation and pseudo-synchronous rotation (Iro, 2008). The predicted increase of temperature from 800 K to 1500 K during a six hours period in the phase of closest approach to the host star in periastron was observed just recently. During the observation of this so-called flash-heating, Laughlin et al. also detected a secondary transit (Laughlin et al., 2009).

The predicted possible primary transit was first detected on February 14th 2009 by various groups (Fossey et al., 2009; Garcia-Melonde et al., 2009; Moutou et al., 2009) with relatively small telescopes at sites of mediocre quality. Due to the extremely long transit duration those groups were not able to cover the complete transit - therefore the resulting data for the transit duration and mid-transit point still vary, depending on the models used. Those transit light-curve models depend on a set of planetary and stellar parameters, such as radius, eccentricity, inclination or the argument of periastron.

SOFIA in turn will be able to observe a more than 8 hours stretch on such an event during a transatlantic flight (see fig. 4.3). A continuous observation of the complete primary transit - including egress, ingress and a reasonable amount out of transit - of HD 80606b will set much better constraints on many of the aforementioned planetary and stellar parameters as well as on possible other planets existing in that system.

HD 80606 (G5 V, Vmag = 8.93) has a close companion HD 80607 (G5 V, Vmag = 9.07). Since the companion is of almost identical spectral type the small separation of only 20 arcsec from HD 80606 makes HD 80607 a perfect calibrator for transit photometry. HD80606b's presence in a binary system like this combined with its extraordinary eccentricity makes it a perfect target for studies of migration processes, such as the mechanism of Kozai cycles or tidal dissipation (Fabrycky & Tremaine, 2007).

The HIPO instrument on board of SOFIA is very well suited for such time critical observation as it is much more sensitive than the instruments previously used for transit observations of this target. Its high temporal resolution is perfectly suited for transit observations with high dynamic ranges. An observation of a long transit of an highly eccentric, long-orbit planet like HD 80606 from the ground requires a composed campaign of an ensemble of telescopes spread around the globe. The need to combine the results from different sites with different instrumental and optical setups under changing observing conditions lowers the quality of the results significantly. SOFIA will be the only observatory to be able to observe almost the whole event with the same telescope/instrument-setup under much more stable conditions (see fig. 4.3) with an instrument like HIPO that was designed for observation exactly like the one proposed.

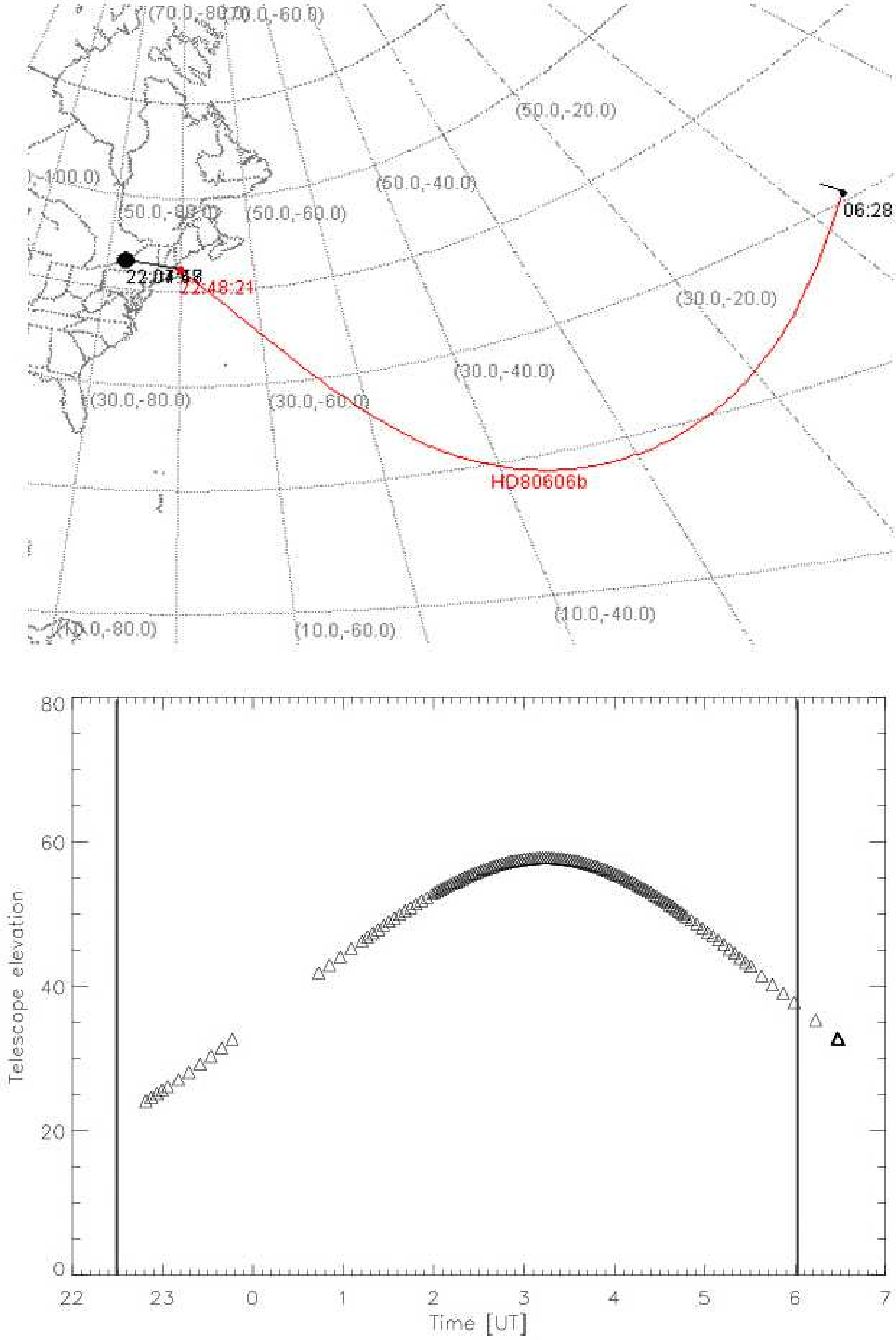

Figure 4.3.: Example flight plan for a SOFIA observation of a HD 80606b transit in January 2010. During a flight from Northern America to the Canary Islands (top) SOFIA is able to keep the star within the observable elevation range for the telescope, i.e. above 20 degree and below 60 degree, for more than 8 hours (bottom).

Observing only the two phases of the egress and ingress already provides crucial information about the exact transit timing and duration. Additional observations of the transit-baseline with high photometric sensitivity at high temporal resolution, is important for modelling the limb-darkening in the light-curve of the particular wavelength range. Furthermore special events as the occultation of a star-spot may occur during this phase.

In the near future many planets discovered by Kepler or CoRoT will have similar orbital configurations and similarly infrequent opportunities for earth-bound observations. SOFIA will be an almost unrivaled observatory for continuous and complete transit-observation of those candidates.

Spectrophotometry of HD149026b using FLITECAM

The observable atmosphere of a planet is a window into its composition and provides clues to its formation history. Since the close-in planets are highly irradiated, of major interest is how the stellar insolation affects the atmosphere. One question for example is how the irradiation affects the atmospheric structure, its temperature distribution and dynamics, its chemistry, and the planet's cooling and contraction. Day-side temperatures of the close-in transiting planets peak at $T_{eff} > 1000$ K, making the NIR an important wavelength regime for such studies (see fig. 4.1). A large fraction of the energy-flux is reradiated between $1.5 - 3$ μm. The emission photospheres lie at fairly deep pressure-depths (0.1-1 bar) where, due to short chemical timescales, the molecular populations should be in near thermochemical equilibrium. Many stable molecules (of abundant reactive elements - H, C, N and O), e.g. H_2O, CO at high temperature and H_2O, CH_4, NH_3 etc. at lower temperature, have strong rotational-vibrational transitions in the NIR under these conditions. At pressure-depths less than 0.1 bar it is likely that populations are increasingly affected by disequilibrium processes such as due to photolytic absorption of the incident ultraviolet radiation. A favorable temperature profile across the relevant emission photosphere given, chemical signatures of the exoplanetary atmosphere should be strongly imprinted in the emergent spectra. As stellar insolation influences the day-side temperature structure, strong horizontal temperature gradients are expected to exist away from the sub-stellar point.

HD 149026b, best qualified as a very hot Saturn, is in a 2.87 d orbit around a metal-rich G0 IV host star (Sato et al., 2005) stands out int the class of highly irradiated exoplanets. The small radius $(0.725 \pm 0.05\ R_J)$ of this planet immediately suggests a significantly metal-enriched interior, with a massive core of nearly 70 earth masses. Subsequent measurements and modelling have confirmed this massive core, with estimates ranging between 35 - 110 $M_{\bigoplus}$ (Sato et al., 2005; Fortney et al., 2006; Ikoma et al., 2006; Broeg & Wuchterl, 2007; Burrows et al., 2007). Given its anomalous properties, HD 149026b can have high impact on theories of formation, evolution and planetary migration; a group of publications already discusses possible solutions to the formation of this object. The radius of HD 149026b has already been determined at optical wavelengths (Sato et al., 2005; Winn et al., 2008), with NICMOS between 1.2-1.9 microns (Carter et al., 2009), and with the Spitzer IRAC 8 micron channel (Nutzman et al., 2009). Carter et al. (2009) find an anomalously large near-infrared planetary radius when compared with measurements in the optical and mid-infrared (the latter two are in agreement). This is hard to reconcile with the usual scenario of a hot stratified atmosphere with absorbers such as H_2O, CO, CH_4 present in expected concentrations with standard vertical distributions. The possibility of a novel atmosphere in this hot, highly-irradiated planet motivates SOFIA-FLITECAM observations. The goal would be to measure the color-dependent radius of HD 149026b in H- and K-bands (note: H-band lies within the wavelength span of the Carter et al. measurement).

These spectra are assumed to be dominated by opacity bands of water and CO. There exist two different models for highly irradiated planets, one with and one without temperature pressure inversion - an effect that splits up the class of highly irradiated hot gas giants into two subgroups (Fortney, 2008). FLITECAM on board of SOFIA is operating in the crucial wavelength region with the required sensitivity (see fig. 4.1), that is problematic to observe from the ground due to telluric absorption of the same molecules assumed to be present in the observed planet's atmosphere (see fig. 4.4). If tests with FLITECAM on SOFIA show that a signal to noise ratio of $\simeq\ 10^4$ at a resolution of $R \simeq 20$ per spectral

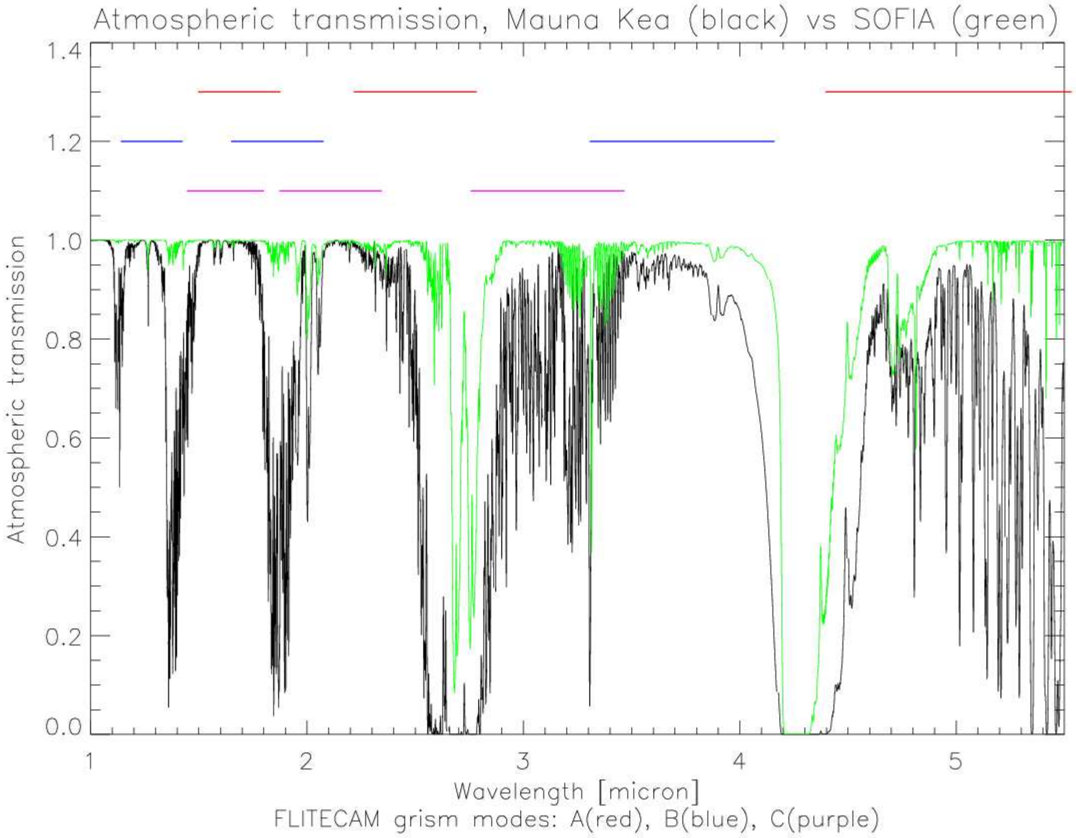

Figure 4.4.: Comparison of the atmospheric transmission on Mauna Kea (black) and at SOFIA's service ceiling (green). The flight level will place the instrument above most of the earth's atmospheric absorption of telluric trace gases such H_2O, CH_4 and CO_2, that are also present in the observed exoplanet's atmospheres. The red, blue and purple lines show the possible orders/filters for the 3 FLITECAM grisms (Smith & McLean, 2006).

channel is within reach and it is possible to proof FLITECAM's stability over a few hours, observations to distinguish between the two different models become feasible (see fig. 4.5).

4.3. Future instrumentation

One of the specific features of SOFIA, which sets it aside from space-based observatories is the fact that SOFIA will be flying up-to-date instrumentation. As such, new generations of instruments can be and will be developed for SOFIA. In this section we present two instrument concepts which are dedicated to exoplanet imaging and spectroscopy and discuss

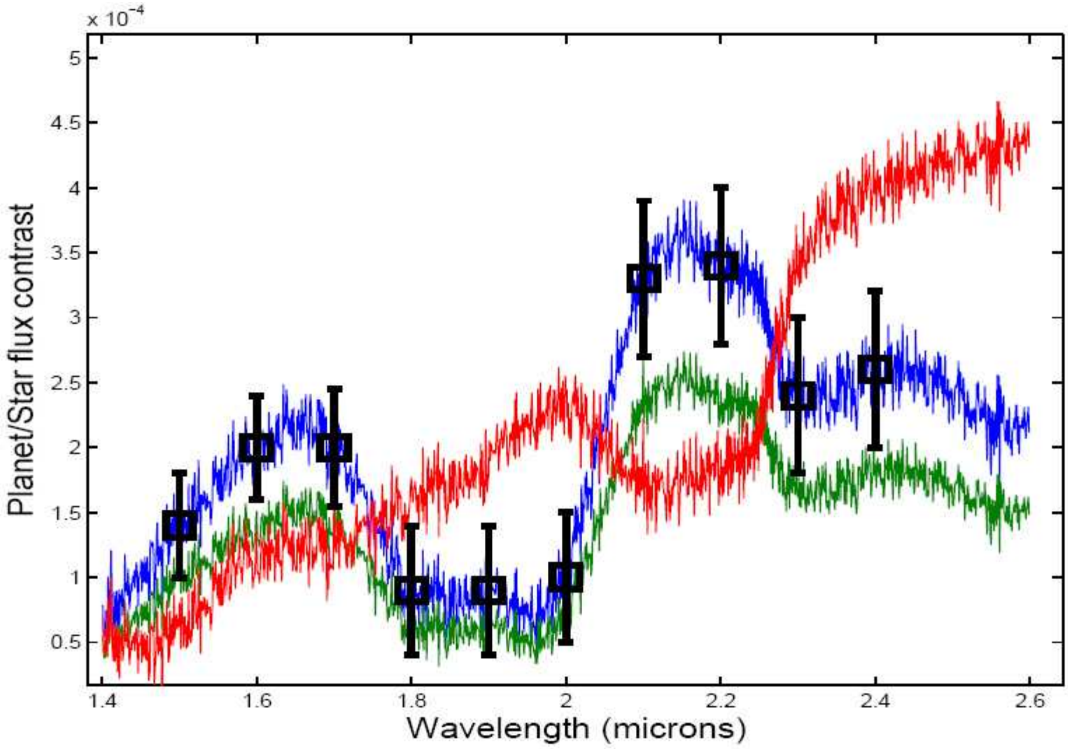

Figure 4.5.: Model contrast-spectra of HD 149026b with two classical (chemical equilibrium, no inversion) emission spectra that assume no (blue) and reasonably efficient (green) transport of the energy deposited by stellar insolation (Hubeny & Burrows 2007). The red model assumes a volatile high altitude absorber causing a deep temperature in- version, whereby the spectral bands of water and CO appear in emission (Taken from HST proposal; Vasisht, Angerhausen et al.). Black markers represent measurements at $R \simeq 20$ of the blue model with the proposed observations combining all possible FLITECAM grism spectroscopy and imaging filters.

their advantages and disadvantages if put on SOFIA.

One is multi-object-spectroscopy (MOS), the other coronagraphy combined with pupil-apodisation. While MOS emphasizes on the spectroscopic part and especially the cancellation of earth atmospheric effects, the coronagraphic approach concentrates on imaging exoplanets at very low spectral resolution. Both instruments are worthwhile to be ported to SOFIA since SOFIA enhances their specific strength and allows a wider wavelength range and therefore a larger number of targets than from the ground. Both instrument concepts do also have a wider field of application than exoplanet science only.

4.3.1. Multi object spectrometer

We already explained that transit observations require rather relative than absolute calibrations. The interesting signal is not the absolute signal of the observed star but the relative changes introduced by the planetary companion during the transit. Therefore constant observation of background, earth's atmosphere and instrument effects is mandatory. Using a multi object spectrometer solves this task by simultaneously observing a group of calibrator stars.

Our analysis showed that SOFIA's 8' x 8' FOV is sufficient to find a set of calibrator stars for multi-object-spectroscopy of most of the known transiting exoplanets (see fig. 4.6). Only for some close-by, bright stars harboring transiting exoplanets the sum of the light of many calibrators will not equal the light of the object. But surveys like CoRoT, Kepler look for lower main-sequence stars (LMSS) of $V_{mag} < 10$, which in most cases have enough stars of similar brightness in a radius of several arcminutes. Kepler for example has an estimated 223.000 stars of $M_V < 14$ in its 105 deg^2 field of view, averaging to about 2000 stars of $M_V < 14$ per deg^2(see fig. 4.7).

One specific advantage for MOS on SOFIA is the fact, that SOFIA can observe under much more stable conditions (e.g. telescope elevation, remaining atmosphere). MOS can also take advantage of observing transit events more frequently than from the ground (see section 4.1.1) and it will also provide SOFIA with an unique phase-space for MOS in wavelength regions not observable from the ground.

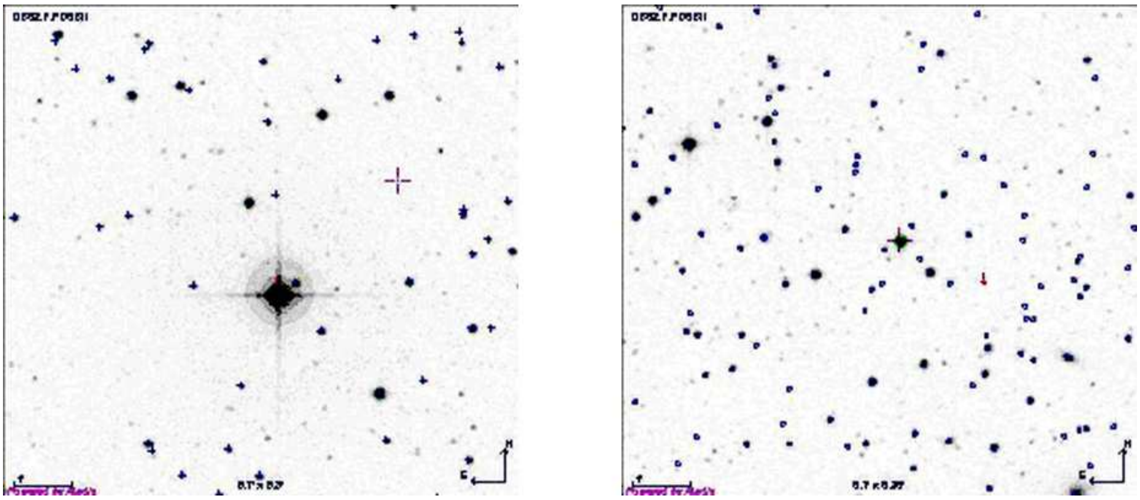

Figure 4.6.: Example for a 8'x8' field around two exoplanetary systems. For the relatively bright ($M_K \simeq 8$) star HD 149026 (left), a set of 6 stars of $M_K \sim 10-12$ and 20 stars of $M_K \sim 12-13$ in an area of the size of SOFIA's field of view might not be enough for MOS. For the fainter TReS-3 (right) system ($M_K \simeq 10$) there is is a nearby calibrator star of $M_K \simeq 9$. Two other examples for systems with very nearby, and - in their cases - even almost identical calibrator stars are X0-2 and HD80606b.

Alternative science goals for MOS on SOFIA can be young stars, galactic center objects, extremely low mass stars in star forming regions , stellar populations in nearby galaxies and AGN/galaxy surveys.

4.3.2. Coronagraph imager

Since extrasolar planets appear usually spatially close to their parent star on sky and are also much fainter, the crucial problem of exoplanet imaging is the cancellation or suppression of the contribution of the host star. One technique that has been gaining increasing popularity in the community in the past years is coronagraphy combined with pupil-apodization (PAC) to image sub-stellar companions or discs around young stars.

It may be possible to upgrade existing (or planned) imaging spectroscopy instrument on SOFIA with a coronagraph and/or pupil apodization unit rather than building a stand-alone instrument.

Ground based PAC instruments already survey hundreds of nearby stars for debris disks, brown dwarfs, and exoplanets. The recently launched Wide-field Infrared Survey Explorer (WISE) mission is going to detect a

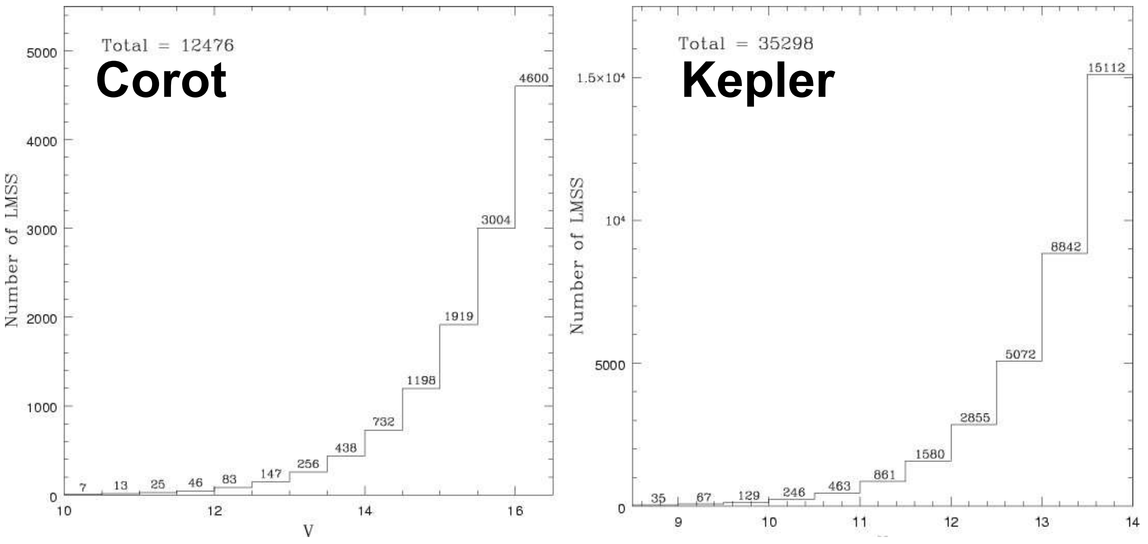

Figure 4.7.: Magnitude distribution of the $V \leq 16.5$ LMSS in a typical CoRoT field (left). Magnitude distribution of the $V \leq 14$ LMSS in the KEPLER field of view (right) from Gillon et al.(2005). Surveys like CoRoT, Kepler look for stars of $V_{mag} < 10$ which in most cases have enough stars of similar brightness in a radius of some arcminutes.

huge number of nearby (dwarf) stars that are too cool to be detected in the visible light. These stars will become primary objective for ground based surveys and probably deliver an even bigger number of possible targets. SOFIA, operating above the absorption bands of water, would be a perfect follow-up observatory for interesting science cases found from the ground at wavelengths not accessible due to atmospheric absorption. Observations in these bands can help to understand, for example, the distribution of water in proto-planetary discs. This can become one science objective for coronagraphic observations in the mid to far IR and is of crucial importance for questions like the formation of giant planets and formation and sustaining of life in planetary systems. The crucial issue of ground-based pupil apodization coronagraphs is the suppression of residual speckle noise. With SOFIA observing at elevations with much lower scintillation this problem should be reduced.

Being able to cancel out the stellar contribution to a level of some 10^{-5} at arcsec resolutions in the MIR/FIR can set a path to imaging and spectroscopy of rather cold, widely separated self-luminous sub-Jupiter class objects (see fig. 4.1).

Another idea to obtain coronagraphic observations with SOFIA is to use an external occulter. An occulter spacecraft can be located near a geostationary orbit and cast its shadow over the SOFIA telescope for relatively long periods of time with only modest velocity changes. At least 5-10 of the currently known exoplanets should be easily observable with a 30-m diameter occulter and SOFIA. These planets should be detectable with existing visible and NIR SOFIA cameras in about an hour of integration time per filter (Wiseman et al., 2006). The contrast required to image these candidates is relatively modest ($\sim$ 18 mag; a suppression of $\sim\ 2\ \times\ 10^7$). This would also be a cheap and straight forward probe mission - especially for external occulter formation flight techniques - for space mission concepts like the New World Observer (NWO) or an external occulter for the JWST.

4.4. Summary

We demonstrate that SOFIA has a specific and unique phase space for exoplanet research. SOFIA operates in the right wavelength regime, above most of the perturbing variation of atmospheric trace gases and can observe rare transient events under optimized conditions. SOFIA will instantaneously be a competitive observatory in the field of state of the art exoplanet astronomy and some science topics are even exclusively observable with SOFIA. We propose dedicated instrumentation which provides SOFIA with a unique edge in exoplanetary science.

5. Summary and Outlook

5.1. Synopsis of results

In this thesis the various methods of space- and ground-based exoplanet transit spectrophotometry were analyzed and applied to available sets of data. In the last chapter future possibilities of the airborne-based SOFIA telescope were discussed.

The ground-based part of this thesis describes the development of methods, with emphasis on the use of integral field units. The central problem of changes in atmospheric trace gases was revealed and several strategies to overcome these problems were described. The presented self-coherence method resulted in the amazing result of a NIR -spectrum of HD 189733b from an IRTF data set the first ever published ground-based exoplanet spectrum.

The space based part described the central issues of Hubble space telescope observations and a method to overcome those. The presented method was first proved to work on a previously published data-set of HD189733b and then applied to a data set of the transiting 'hot Neptune' planet GJ436b, resulting in two consistent H-band spectra of this planet.

In the final part future perspectives for SOFIA in the field of exoplanet science, especially in transit spectrophotometry using the HIPO-FLITECAM instruments were explained.

The publications Swain et al. (2009b), Swain et al. (2010), Angerhausen et al. (2006), Angerhausen et al. (2007) and Angerhausen at al. (2009) resulted from the work presented here. Furthermore a publication about the SOFIA exoplanet science case (chapter 4) is submitted to PASP and under review and a publication discussing the GJ 436b HST observation and results (chapter 3) is in preparation and close to submission.

5.2. Future perspectives

The next few years will see the expansion of observable extrasolar planets using ground-based discovery methods as well as the brightest targets from Kepler and CoRoT (see fig. 5.1). In the past few years Hubble (see chapter 3 as an example) and Spitzer have been successfully used for spectroscopic characterization of extrasolar planets. Since the HST-NICMOS instrument broke and Spitzer warmed up those space-based opportunities are limited until JWST starts operating. For the next 4 years CoRoT, Kepler and other (transit-) survey are going to deliver a large number of new targets with interesting opportunities for characterization. The methods using ground-based telescopes described in this thesis (see chapter 2) and the airborne-based platform SOFIA (see chapter 4) will help to close this gap to follow up Kepler/CoRoT planets and as testbed for future JWST observations.

Large ground based telescopes and SOFIA can provide the next set of breakthrough measurements, i.e., moderate to high resolution spectra of transiting planets in the near-IR atmospheric bands. As the techniques on these platforms are improved upon and refined, they promise to step jump in terms of both the number of observable planets as well as a dramatic improvement in the available spectral resolution.

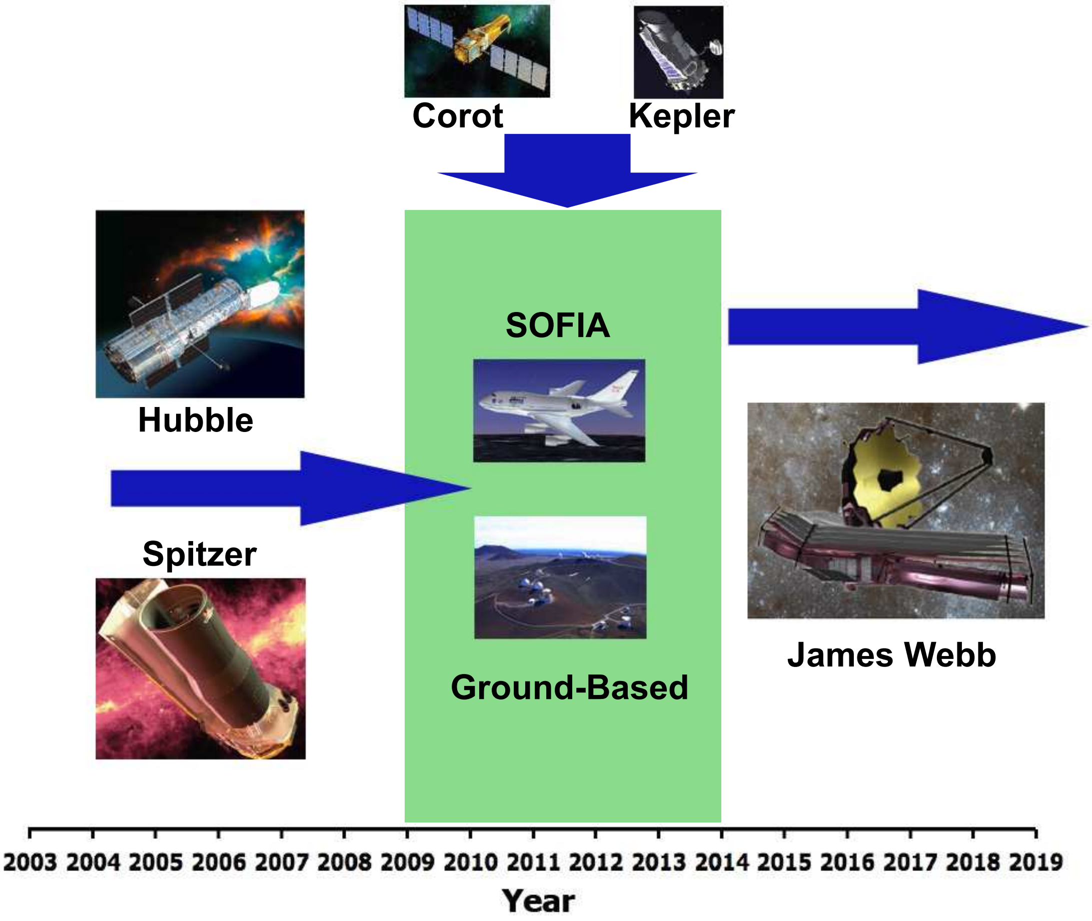

Figure 5.1.: Diagram to explain the short term future perspectives of the techiques described in this work. In the past few years Hubble and Spitzer (left) have been successfully used for spectroscopic characterization of extrasolar planets. Since the HST-NICMOS instrument broke and Spitzer warmed up those space-based opportunities are limited until JWST starts operating. For the next 4 years CoRoT and Kepler (top) are going to deliver a large number of new targets with interesting opportunities for characterization. The methods using ground-based telescopes described in this thesis and the airborne-based platform SOFIA (see last chapter) will help to close this gap to follow up Kepler/CoRoT planets and as testbed for future JWST observations.

A. Appendix I

A.1. Transit timing

Exact timing is critical since the observation time during the transit phase is limited to ~ 2 hours for close in Hot Jupiter class planets. The exact times of the secondary transit and its duration were still uncertain at the time of my first observation. I assessed them from the times of primary transit, which had been determined quite frequently, from the best determination of the orbital eccentricity and from the longitude of periastron. In the following part I describe the used calculations. My newer observations were made on targets already observed in secondary eclipse so that calculations like the following were not necessary. However, for newly detected transiting planets, those calculations have to be made for first time observations of a secondary eclipse.

Timing of the secondary transit (ST) is critical since the signal decreases with twice the time lag and the secondary transit only lasts about 2 hours per 2.2 days orbit. A timing error of just one hour would wipe out the entire observable signal. However, a careful determination of the orbit of HD189733b by Bakos et al. (2006) provided an accuracy of the primary transit (PT) times to within several minutes.

In first order calculations the uncorrected central time of secondary eclipse $T_{ST,unc.}$ can be drawn from primary transit central time T_{PT} and the known period P timing, assuming it occurs exactly half a planetary period after the PT, via:

$$T_{ST,unc.} = T_{PT} + \frac{P}{2} \tag{A.1}$$

However, depending on the orbital parameters of the system, the real central time of secondary eclipse $T_{ST,real}$ can differ from that value. The calculation of the timing difference between $T_{ST,unc.}$ and the real value $T_{ST,real}$ of secondary eclipse will be described in the following paragraphs.

A.1.1. Time difference of secondary eclipse central time

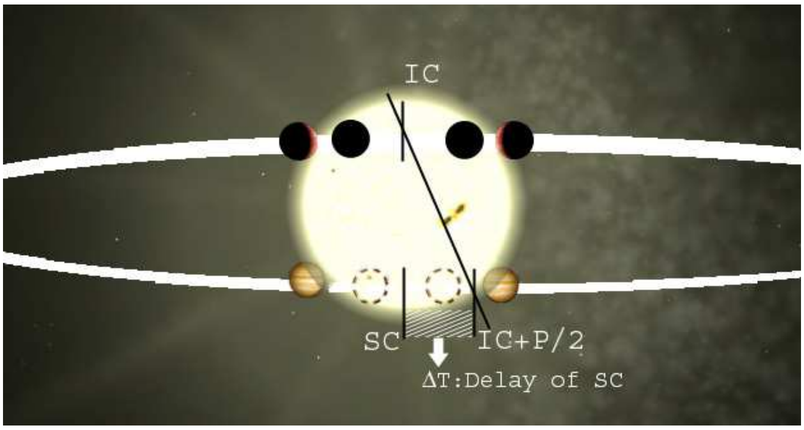

Figure A.1.: For geometric reasons the central point of secondary eclipse does not necessarily happen half a period after primary transit. Depending on the argument of periastron ω and eccentricity e (see equation A.4). Deriving the exact real point of secondary eclipse is of imminent importance for the success of such an observation.

As mentioned above, equation A.1 only calculates the uncorrected time $T_{ST,unc.}$, exactly half a period $\frac{P}{2}$ after primary transit T_{PT}.

In reality (see fig. A.1) there is a temporal difference δT between the time $T_{ST,unc.}$ and the real central time of secondary eclipse $T_{ST,real}$ (see equation A.4) due to the systems geometry. Reasons for that are close to, but not exactly zero eccentricity e in combination with the usually not very well determined argument of periastron ω.

$$\delta T = (T_{PT} + \frac{P}{2}) - T_{ST,real} = T_{ST,unc.} - T_{ST,real} \tag{A.2}$$

This difference δT can be calculated (Charbonneau et al. 2003, Kallrath $\&$ Milone 1999) :

$$\frac{\pi}{2P}(T_{ST} - T_{PT} - \frac{P}{2}) \simeq e \cdot cos(\omega) \leq e \tag{A.3}$$

$$\delta T = 2Pe\frac{cos(\omega)}{\pi} \tag{A.4}$$

The following figure A.2 shows a contour-plot of possible time shifts δT as a function of eccentricity e (x-axis) and argument of periastron ω (y-axis). The axis cover the complete 1-sigma space of ω and e for HD 209458b at the time I planned my first observation in 2005. At the intersection of the most probable value I get a time shift of δ T = 9 min. However, values between -9 min and +45 min are possible for all possible combinations of e and ω. This shows how important the very accurate derivation of those parameters is for the planning of secondary eclipse observation of planets, that only have been observed in primary transit before.

Deming et al. observed HD 209458b in secondary eclipse using the Spitzer Space Telescope (SST) in 2005 and derived a value δ T = 0 $\pm$ 7 min (Deming et al. 2006), confirming $e \simeq 0$. This value, well inside the error-bar of my calculation, was sufficient to plan my later observations.

A.1.2. Duration of secondary eclipse

For similar reasons as time-shifts in the transit midpoint can occur (see fig. A.3), the duration of secondary transit can be different from the duration od primary transit.

According to Charbonneau (2003) there is the following connection between eccentricity e,argument of periastron ω , duration of primary transit Θ_I and duration of secondary eclipse Θ_{II} :

$$\frac{\Theta_I - \Theta_{II}}{\Theta_I + \Theta_{II}} \simeq e \cdot sin(\omega) \tag{A.5}$$

$$\Theta_{II} \simeq \Theta_I \frac{1}{1 + 2e \cdot sin(\omega)} \tag{A.6}$$

For transiting exoplanets the times between 1st contact (start of *ingress*) and 4th contact (end of *egress*, see fig. 1.4) or primary transit T_{PT14}, as well as the duration of total occultation T_{PT23}, is usually very well determined.

The parameter of expected duration of secondary eclipse (fig. A.4)

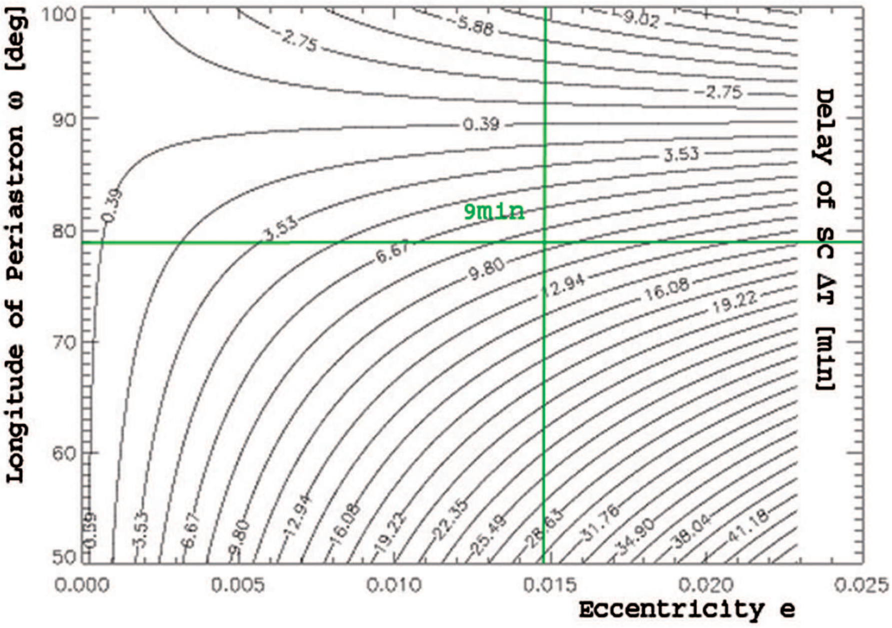

Figure A.2.: Contour plot of the isochrones of the time shift δT between the real transit midpoint $T_{ST,real}$ and the uncorrected $T_{ST,unc.}$as a function of eccentricity e (x-axis) and argument of periastron ω (y-axis). The axis cover the complete 1-sigma space of ω and e for HD 209458b at the time I planned my first observation in 2005. At the intersection of the most probable value I get a time shift of δ T = 9 min. However, values between -9 min and +45 min are possible for all possible combinations of e and ω. This shows how important the very accurate derivation of those parameters is for the planning of secondary eclipse observation of planets, that only have been observed in primary transit before.

can also vary from the duration of primary transit (especially for high-eccentric planets). Figure A.1.1 shows the expected duration of secondary eclipse Θ_{II} for HD209458b as a function of eccentricity e and argument of periastron ω, similar to figure A.1.1 for the time shift.

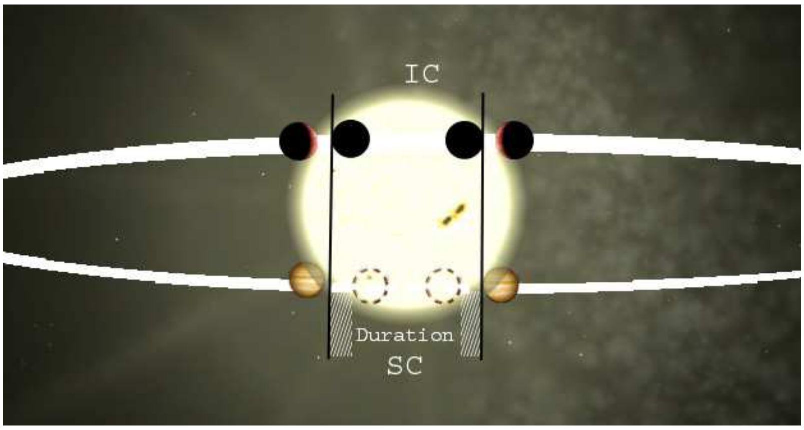

Figure A.3.: The parameter of expected duration of secondary eclipse (fig. A.4) can also vary from the duration of primary transit (especially for high-eccentric planets). Depending on eccentricity e and argument of periastron ω secondary eclipse can be significantly shorter or langer than primary transit (see equation A.6).

A.2. Signal to noise calculations for ground-based observations

In the following part we describe the model calculations we applied before our first transit observation with the SINFONI instrument.

To finally get to the expected signal to noise ratio we start with calculating the expected contrast of the planet in relation to its host star by comparing the expected fluxes.

Therefore we assume the host star to be a black-body, while we add contributions from reflected stellar light and its own black-body emission for the planet.

In a next step we integrate the influence of the adaptive optics system by dividing the flux in its diffraction and seeing part using the expected Strehl ratio.

In order to calculate the diffraction part (Airy-distributed) we calculate the flux of the star at the position of the planet and then integrated over the inner Airy-disc of the planet'S signal.

The calculation of the seeing part works analogue. First the Gaussian-distributed Intensity at the planet's position is calculated and then integrated over the inner Airy disc.

To avoid overexposure of the detector'S pixels and to get a number for

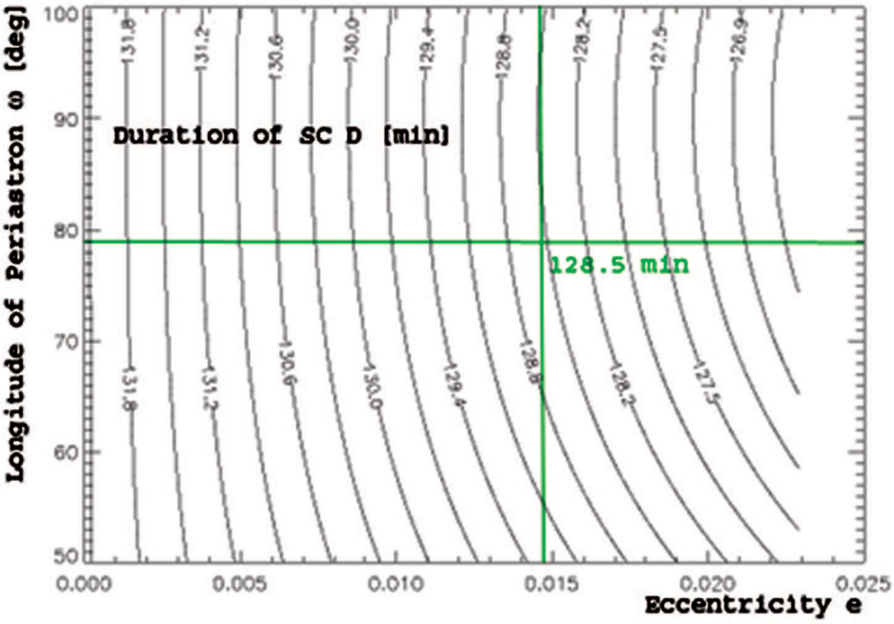

Figure A.4.: Contour plot of the possible eclipse durations Θ_{II} as a function of eccentricity e (x-axis) and argument of periastron ω (y-axis). The axis cover the complete 1-sigma space of ω and e for HD 209458b at the time I planned my first observation in 2005.At the intersection of the most probable value I get a duration of 128.5 min. However, values between 126 min and 132 min were possible.

the optimal integration times the next step is to get an estimate for the saturation.

Therefore the values of the Signal (from diffraction and seeing part) are calculated for the peak pixel and added with contributions from background or dark current of the detector.

In a last step all information are put together to get a final value for the expected signal to noise ratio.

A.2.1. Contrast planet-star

The contrast describes the relation between the flux contributed of the star S_{Pl} to the one emitted by the planet S_{St} :

$$C = \frac{S_{Pl}}{S_{St}} \tag{A.7}$$

Modelling the star as a black-body $B(\lambda, T_{St})$ with temperature T_{St} we get to an expression for S_{St} and S_{Pl} in a wavelength area $\Delta\lambda$:

$$S_{St} = B(\lambda, T_{St}) \cdot \Delta\lambda \cdot A_{Tel} \cdot \Omega_{St} \tag{A.8}$$

$$S_{Pl} = I_{Pl}(\lambda, T_{Pl}) \cdot \Delta\lambda \cdot A_{Tel} \cdot \Omega_{Pl} \tag{A.9}$$

Here I_{Pl} is the sum of the black-body-radiation $B(\lambda, T_{Pl}$ of a planet with temperature $T_{Pl})$ and a second term, that describes the amount of reflected starlight:

$$I(\lambda, T_{Pl}) = (1 - \epsilon_{\lambda}^{e}) \cdot B(\lambda, T_{Pl}) + B(\lambda, T_{St}) \cdot \frac{\Omega_{St@Pl}}{\Omega_{Hemi}} \cdot \epsilon_{\lambda}^{e} \cdot IL \tag{A.10}$$

IL describes the phase of the planet in the line of sight of the observer ($0 < IL < 1$, 0: night-side, 1: day-side of planet completely visible) and ϵ its emissivity. The fraction $\frac{\Omega_{St@Pl}}{\Omega_{Hemi}}$ describes the dilution of the reflected starlight at the planetary surface by the relation between the solid angle at the planet's position $\Omega_{St@Pl}$ and the whole hemisphere Ω_{Hemi}:

$$\frac{\Omega_{St@Pl}}{\Omega_{Hemi}} = \frac{\pi \frac{r_{St}^2}{d^2}}{2\pi} = \frac{r_{St}^2}{2d^2} \tag{A.11}$$

with stellar radius r_{St} and distance between star and planet d.

With regard to A.11 we get for the contrast C:

$$\frac{1}{C} = \frac{B(\lambda, T_{St}) \cdot r_{St}^2}{(B(\lambda, T_{St}) \cdot \frac{r_{St}^2}{2d^2} \cdot \epsilon_{\lambda}^{e} \cdot IL + (1 - \epsilon_{\lambda}^{e}) \cdot B(\lambda, T_{Pl})) \cdot r_{Pl}^2} \tag{A.12}$$

respectively

$$C = \left\{ \frac{\epsilon_{\lambda}^{e} \cdot IL}{2d^2} + \frac{(1 - \epsilon_{\lambda}^{e}) \cdot B(\lambda, T_{Pl})}{B(\lambda, T_{St}) \cdot r_{St}^2} \right\} \cdot r_{Pl}^2 \tag{A.13}$$

In this equation the first term represents the fraction of reflected starlight and the second term the thermal emission of the planet.

A.2.2. Imaging, adaptive optics

For our observation using adaptive optics in the NIR we assume a gaussian seeing-distribution and a good Strehl ratio with the diffraction maximum in Airy-distribution.

Inside a growing diffraction peak with constant FWHM the flux F_{diff} inside the peak is proportional to the height of the peak. FWHM of the seeing stays constant while the flux is distributed into the diffraction pattern. With regard to this the peak of the seeing distribution is also proportional to the flux inside the seeing-disc.

Hence the Strehl-ratio f_{Str} describes the relation between flux F_{diff} inside the diffraction pattern to the flux inside the seeing-pattern F_{seeing}. (E.g. 70 % Strehl: 0.7 · flux in side the diffraction-pattern, 0.3 · flux inside the seeing-pattern)

$$F_{St} = F_{diff} + F_{seeing} = f_{Str}F + (1 - f_{Str})F \tag{A.14}$$

Diffraction

The diffraction spike flux distribution is:

$$I_{diff} = I_0 \cdot \left(\frac{2J_1(u)}{u}\right)^2, u = \pi\frac{\oslash}{\lambda}\vartheta \tag{A.15}$$

with J_1 the Bessel-function of 1. order with argument u, that is a function of angular distance between star and planet $\vartheta = \frac{d}{D}$, wavelength λ and telescope diameter $\oslash$. This is the so-called *Airy-pattern.* D is the distance of the observed star from earth, while d describes the distance between star and planet.

The flux of the star at the location of the planet on the image as distributed by diffraction is:

$$I_{diff} = I_0 \cdot \left(\frac{2J_1\left(\pi\frac{\oslash d}{\lambda D}\right)}{\pi\frac{\oslash d}{\lambda D}}\right)^2 \tag{A.16}$$

I_0, denoting the peak value of the distribution function can be related to the total signal within the Airy disk:

$$F_{Airy} = S \cdot t_{int} \tag{A.17}$$

$$F_{Airy} = \int_0^{2\pi} d\varphi \int_0^{\infty} I(u) \cdot u \cdot du = I_0 \cdot 4\pi \tag{A.18}$$

$$I_{diff} = \frac{F_{Airy}}{\pi} \cdot \left(\frac{J_1\left(\pi \frac{\oslash d}{\lambda D}\right)}{\pi \frac{\oslash d}{\lambda D}} \right)^2 \tag{A.19}$$

I_{diff} provides the flux level of the Airy function at the distance - therefore position - of the planet. The stellar signal at this position can be obtained by integrating over the angular size of a planetary object, which certainly is point like, therefore, can typically be replaced by the integration over the inner Airy disk out to the first maximum, i.e. 1 beam. To simplify the integration a constant stellar signal is assumed across the inner planetary Airy disk. Then:

$$F_{St,1beam}^{Airy} = I_{diff} \cdot (1.22\pi)^2 \pi \tag{A.20}$$

Seeing

The angular seeing flux distribution:

$$I_{seeing} = I_0 \cdot \exp\left(\frac{-\vartheta^2}{2\sigma^2}\right) \tag{A.21}$$

with ϑ as above and

$$\sigma = \frac{FWHM_{seeing}}{2\sqrt{ln4}} \tag{A.22}$$

yields,

$$I_{seeing} = I_0 \cdot \exp\left(\frac{-d^2 \cdot 2ln4}{D^2 \cdot FWHM_{seeing}^2}\right) \tag{A.23}$$

I_0,

denoting the peak value of the distribution function can be related to the total signal within the 2 dimensional seeing disk

$$F_{seeing} = S \cdot t_{int} \tag{A.24}$$

$$F_{seeing} = I_0 \int_0^{2\pi} d\varphi \int_0^{\infty} \exp\left(\frac{-\vartheta^2}{2\sigma^2}\right) \vartheta d\vartheta = I_0 \cdot 2\pi\sigma^2 \tag{A.25}$$

The flux of the star at the location of the planet on the image as distributed by seeing is then:

$$I_{seeing} = F_{seeing} \cdot \exp\left(\frac{-d^2 \cdot 2ln4}{D^2 \cdot FWHM_{seeing}^2}\right) \cdot \frac{2ln4}{\pi \cdot FWHM_{seeing}^2} \tag{A.26}$$

I_{seeing} provides the flux level of the assumed radially symmetric seeing disk at the distance - therefore position - of the planet. Again, as above, the stellar signal at this position can be obtained by integrating over the inner Airy disk out to the first minimum, i.e. 1 beam. To simplify the integration a constant seeing is assumed across the inner planetary Airy disk. Then:

$$F_{St,1beam}^{seeing} = I_{seeing} \cdot \left(1.22\frac{\lambda}{\oslash}\right)^2 \cdot \pi \tag{A.27}$$

A.2.3. Sum: seeing and diffraction

The sum of the seeing and diffraction disk also considering the Strehl-ratio (A.14) then is:

$$\begin{aligned} F_{St,1beam} &= F_{St,1beam}^{diff} + F_{St,1beam}^{seeing} \\ &= F_{St}\left\{\frac{f_{Str}}{\pi}\left(\frac{J_1\left(\pi\frac{\oslash d}{\lambda D}\right)}{\pi\frac{\oslash d}{\lambda D}}\right)^2 (1.22\pi)^2\pi + \frac{1-f_{Str}}{2\pi\sigma} exp\left(-\frac{\frac{d^2}{D^2}}{2\sigma^2}\right)\left(1.22\frac{\lambda}{Tel}\right)^2 \pi\right\} \\ &= (1.22)^2 F_{St}\left\{f_{Str}\pi^2\left(\frac{J_1(u)}{u}\right)^2 + \frac{(1-f_{Str})\lambda^2 \cdot 2ln4}{FWHM_{seeing}^2 \oslash^2} exp\left(\frac{d^2 \cdot 2ln4}{D^2 FWHM_{seeing}^2}\right)\right\} \end{aligned} \tag{A.28}$$

This is the approximate contribution of the stellar flux at the position of the planet within 1 Airy disk.

The approximation holds for $\frac{d}{D} \geq 2.44 \cdot \frac{\lambda}{Tel}$.

A.2.4. Saturation and background

Saturation occurs if the number of e^- collected during the time t_{int} exceeds the maximum number of Photons max_{Ph}. Such a situation preferentially occurs at the peak of the combined seeing and diffraction stellar profile. The signal at that pixel is the sum of the signal from the star, the background, and the dark current in the detector.

Contribution from diffraction

Applying the calculations above yields for a quadratic pixel assuming Nyquist sampling:

$$F_{St}^{Airy}(1pixel@peak) \equiv F_{St,1peak}^{Airy} = I_{diff}(@center) \cdot \frac{(1.22\pi)^2}{4} \tag{A.29}$$

$$\lim_{u \to 0} I_{diff} = \frac{F_{Airy}}{4\pi} \tag{A.30}$$

thus

$$F_{St,1peak}^{Airy} = \frac{F_{Airy}}{4\pi}\frac{(1.22\pi)^2}{4} = \frac{1.22^2 \cdot \pi \cdot F_{Airy}}{16} \tag{A.31}$$

I have simplified the calculation in assuming a flat top profile across the pixel which is not true, of course. I overestimate the flux towards the conservative side by about 10 to 20 percent (estimated), which is acceptable here.

Contribution from Seeing

For the contribution from seeing accordingly:

$$F_{St}^{seeing}(1pixel@peak) \equiv F_{St,1peak}^{seeing} = I_{seeing}(@center) \cdot \frac{(1.22\frac{\lambda}{Tel})^2}{4} \tag{A.32}$$

$$\lim_{d\to 0} I_{seeing} = F_{seeing} \cdot \frac{2ln4}{\pi \cdot FWHM_{seeing}^2} \tag{A.33}$$

$$F_{St,1peak}^{seeing} = \frac{ln4 \cdot F_{seeing}}{2\pi} \left(\frac{(1.22 \cdot \lambda)}{{}_{Tel} \cdot FWHM_{seeing}} \right)^2 \tag{A.34}$$

Sum

The sum of both contributions is then:

$$\begin{aligned} F_{St,1peak} &= F_{St,1peak}^{diff} + F_{St,1peak}^{seeing} && \text{(A.35)} \\ &= F_{St} \left(\frac{1.22^2 \cdot \pi \cdot f_{Str}}{16} + \frac{ln4 \cdot (1 - f_{Str})}{2\pi} \cdot \left(\frac{1.22 \cdot \lambda}{{}_{Tel} FWHM_{seeing}} \right)^2 \right) && \text{(A.36)} \\ &= (1.22)^2 \cdot F_{St} \cdot \left(\frac{f_{Str} \cdot \pi}{16} + \frac{(1 - f_{Str}) \cdot \lambda^2 \cdot ln4}{2\pi \cdot FWHM_{seeing}^2 \cdot {}_{Tel}^{2}} \right) && \text{(A.37)} \end{aligned}$$

Using (A.24) and (A.8) we have for the stellar signal on the detector

$$\begin{aligned} F_{St} &= t_{int} \cdot B(\lambda, T_{St}) \cdot \Delta\lambda \cdot A_{Tel} \cdot \Omega_{St} \cdot T_{System} \cdot Q\eta && \text{(A.38)} \\ &= t_{int} \cdot F_{\lambda} \cdot \Delta\lambda \cdot A_{Tel} \cdot T_{System} \cdot Q\eta && \text{(A.39)} \end{aligned}$$

with $Q\eta$, the quantum- efficiency of the detector, we can replace:

$$F_{\lambda} = F_{\lambda}^{Vega} \cdot 10^{-0.4 m_{\lambda}} = B(\lambda, T_{St}) \cdot \Omega_{St} \tag{A.40}$$

T_{sys} denotes the overall transmission including atmosphere, telescope, and instrument without detector. A_{Tel} denotes the telescope collecting area.

The number of recorded photons n_{Ph}^{St} in the peak pixel are then:

$$n_{Ph}^{St} = \frac{F_{St,1peak}}{\frac{hc}{\lambda}} \tag{A.41}$$

A.2.5. Contribution from thermal background

The background in the NIR is dominated by the thermal emission $B(\lambda, T_{Tel,AO})$ of the telescope and AO system combined at temperature $T_{Tel,AO}$ and emissivity ε_λ. It is assumed to be spatially flat.

The background signal on the detector is:

$$F_{back} = t_{int} \cdot B(\lambda, T_{Tel,AO}) \cdot \Delta\lambda \cdot A_{Tel} \cdot \Omega_{Tel,AO} \cdot T_{Instr.} \cdot Q\eta \cdot \varepsilon_\lambda^{Tel,AO} \tag{A.42}$$

and for the number of photons n_{Ph}^{back} from background on each pixel:

$$n_{Ph}^{back} = \frac{F_{back}}{\frac{hc}{\lambda}} \tag{A.43}$$

$T_{Instr.}$ denotes the transmission coefficient. The quantity $A_{Tel} \cdot \Omega_{Tel,AO}$ is the throughput and constant throughout the optical path. It's value for one beam at the location of the planet at the focus of the telescope downstream the AO is the product of the FOV of one beam and the solid angle provided by the f-ratio f_{Tel}:

$$A = \pi \left(1.22 \frac{\lambda \cdot f_{Tel}}{\oslash}\right)^2, \Omega = \pi \left(\frac{\oslash}{2 f_{Tel}}\right)^2 \Rightarrow A\Omega = \left(\frac{1.22\pi\lambda}{2}\right)^2 \tag{A.44}$$

which is the same as the product of the telescope area $A_{Tel} = \frac{\oslash}{2}^2 \cdot \pi$ and the solid angle corresponding to one beam $\Omega_{Tel} = (1.22\lambda/\oslash)^2 \cdot \pi$.

For the thermal background on one single pixel, A is instead:

$$A = \pi \left(\frac{1.22}{2} \frac{\lambda \cdot f_{Tel}}{\oslash}\right)^2 \Rightarrow A\Omega_{Back} = \pi \left(\frac{1.22\lambda}{4}\right)^2 \tag{A.45}$$

A.2.6. Contribution from sky background

The sky background flux F_{Sky}^K per beam in K-Band is:

$$F_{Sky}^K = F_{Vega}^\lambda \cdot 10^{-0.4 m_{sky}^K} \cdot t_{int} \cdot \Delta\lambda \cdot A_{Tel} \cdot Q\eta \cdot \frac{T_{Sys}}{T_{Sky}} \cdot \frac{\Omega_{1beam}}{\Omega_{1''2}} \tag{A.46}$$

where: $\Omega_{1beam} = \left(\frac{\pi}{3600 \cdot 180}\right)^2$ and $\Omega_{1''^2} = \left(\frac{1.22\lambda}{4}\right)^2 \cdot \pi$,

are the solid angles for $1 arcsec^2$ and for the beam of the Airy disc out to the first dark ring. The sky background per single pixel, e.g., the peak flux pixel, is:

$$F_{Sky}^{K,1pixel} = F_{Vega}^{\lambda} \cdot 10^{-0.4m_{sky}^{K}} \cdot t_{int} \cdot \Delta\lambda \cdot A_{Tel} \cdot Q\eta \cdot \frac{T_{Sys}}{T_{Sky}} \cdot \frac{\Omega_{1pix}}{\Omega_{1''^2}} \tag{A.47}$$

where $\Omega_{1pix} = \left(\frac{1.22\lambda}{2 \cdot \varnothing}\right)^2$, the FOV^2 of one pixel assuming Nyquist sampling.

A.2.7. Maximum integration-time

The total signal on the detector pixel with the maximum flux is:

$$n_{Ph,ges} = n_{St}^{Ph} + n_{back}^{Ph} + n_{dark}^{e} = \frac{F_{St,1peak} + F_{back}}{hc/\lambda} + I_{Dark} \cdot t_{int} \tag{A.48}$$

The integration time per frame t_{frame}^{int} has to be selected such that $n_{Ph} < max_{Ph}$ always. Longer effective integration times t_{total}^{int} are achieved by repeating the integration m times

$$t_{total}^{int} = m \cdot t_{frame}^{int} \tag{A.49}$$

A.2.8. Signal to noise ratio

The signal of the planet on the detector is the total stellar flux F_{St} divided by the contrast C :

$$F_{Pl} = 0.838 \cdot F_{St} \cdot C \tag{A.50}$$

Here the factor 0.0838 accounts for the fact that the planetary signal is only integrated over the inner airy disc up to the first dark ring.

The number of photons n_{Pl}^{Ph} that are observed from the planet is:

$$n_{Pl}^{Ph} = \frac{F_{Pl}}{\frac{hc}{\lambda}} \tag{A.51}$$

The noise N^{Frame} at the position of the planet on the detector per frame then is (assuming Poisson photon statistics):

$$N^{Frame} = \sqrt{n_{St}^{Ph} + n_{back}^{Ph} + n_{Pl}^{Ph} + N_{Det}^{2}} \tag{A.52}$$

The total detector noise N_{Det} is:

$$N_{Det} = \sqrt{\frac{r^2}{NDS} + s \cdot NDS + I_{Dark} \cdot t_{int}} \tag{A.53}$$

where r is the readout noise, s the shift-register glow and NDS the number of readouts.

The S/N of an observation in a single spectral channel yields:

$$(\frac{S}{N})_{1channel} = \frac{n_{Ph}^{Pl}}{N^{Frame}}. \tag{A.54}$$

The total number of channels be $n_{channel}$.

A specific channel will only contribute to the overall S/N if the planetary spectrum is not identical with the stellar spectrum in that part of the spectrum. Assuming that specific planetary features account for a fraction e_{Pl} of the planetary spectrum, the total S/N per beam at the location of the planet is then:

$$\frac{S}{N} = \frac{n_{Pl}^{Ph}}{N^{frame}} \sqrt{m \cdot e_{Pl} \cdot n_{channel}} \tag{A.55}$$

where m is the number of repetitions.

A.2.9. Application to my observation

The calculation presented here were fed in to a computer model to calculate the needed parameters for our observation using the specific values of the used telescope and target.

Using the telescope, instrument and object values from tabular 3.1 and B.1.3 we get to the following model results for the VLT-SINFONI observation of HD 209458b:

For the average contrast we get a value of 0.0002, which is consistent with the models, especially with regard to our rather conservative assumptions. The S/N ration for the planetary signal per spectral bin assuming an integration time of 120 min per phase (in/out of transit) is 3.38. The expected S/N of the collapsed spectrum is then 108.2.

A.3. Observing efficiency: optimized frequency of sky-observations

A.3.1. Introduction

The goal of the following calculations is to define the optimal frequency of sky observations for the VLT-SINFONI campaigns described in chapter 2. Since the host stars of my targets are much brighter than the sky-background the ABAB (A:target observation, B: sky observation) observation pattern is not optimal. Instead the observing efficiency can be increased by observing just one sky frame after a certain number of target frames and still correct the noise induced by the sky in an sufficient way. Here I present a way to calculate this number depending on the the ratio of target flux to the background flux.

A.3.2. Defining the problem

Instead of using an ABAB target-sky observing pattern (see A.3.1), I define a general pattern of nABnAB, where n stands for the times I integrate on the target (A) before taking another sky-frame (B). The parameter n can be optimized to maximize the signal-to-noise-ratio:

$$\frac{S}{N}(nA - B) = \frac{nS_o}{\sqrt{nN_o^2 + nN_o^2 + n^2N_s^2}} \tag{A.56}$$

Here S_o is the signal of the target, N_o the noise of the target, N_s the noise of the sky and S_s the signal of the sky.

Assuming the target has x times more flux than the sky,

$$S_o = xS_s \Rightarrow N_o = \sqrt{x}N_s \tag{A.57}$$

I get to:

$$\frac{S}{N}(nA - B) = \frac{nS_o}{\sqrt{n}N_o\sqrt{1 + 1/x + n/x}} = \sqrt{\frac{nx}{x + n + 1}} \cdot \frac{S_o}{N_o} \tag{A.58}$$

In order to maximize the signal-to-noise ratio $\frac{S}{N}(nA - B)$ I assume N to be the total number of frames and K the number of (nA-B) groups obtained:

$$N = (n+1)K \tag{A.59}$$

$$\Rightarrow \frac{S}{N}(K(nA-B)) = \sqrt{\frac{xnK}{x+n+1}} \cdot \frac{S_o}{N_o} \tag{A.60}$$

since N is constant

$$= \sqrt{\frac{xnN}{(n+1)(x+n+1)}} \cdot \frac{S_o}{N_o} \tag{A.61}$$

The question now is, how much better this can be than the signal-to-noise-ratio $\frac{S}{N}(n(A-B))$, when observing in the conventional ABAB pattern:

$$\frac{S}{N}(n(A-B)) = \frac{\sqrt{n}S_o}{\sqrt{N_o^2 + 2N_s^2}} \tag{A.62}$$

With $N = (1+1)K = 2K = 2n$ (n:number of A-B pairs) and $N_o = \sqrt{x}N_s$,

$$\Rightarrow \frac{S}{N}(n(A-B)) = \sqrt{\frac{N}{2N_o^2(1+2/x)}}S_o = \sqrt{\frac{xN}{2(x+2)}} \cdot \frac{S_o}{N_o} \tag{A.63}$$

A.3.3. Maximize the efficiency

In order to maximize the observing efficiency I compute the the maximum of the fraction of the S/N ratios of the two cases:

$$\frac{\frac{S}{N}(nA-B)}{\frac{S}{N}(n(A-B))} = \sqrt{\frac{xnN2(x+2)}{(n+1)(x+n+1)xN}} = \sqrt{\frac{2n(x+2)}{(n+1)(n+1+x)}} = f(n) \tag{A.64}$$

$$\frac{df(n)}{dn} = 0, n > 0, x \geq 0 \tag{A.65}$$

$$\Leftrightarrow n = \sqrt{x+1}, x = n^2 - 1 \tag{A.66}$$

This result shows that, when the target is x times brighter than the sky background the optimal number n of target frames (A) to be taken between sky observations (B) is $n = \sqrt{x+1}$. If, for example, the target is 8 times brighter than the background, the optimal number n of target observations (A) is $n = \sqrt{8+1} = 3$. In this case AAABAAAB would be the most efficient observing strategy.

The maximum value (for $x = n^2 - 1$), i.e. the improvement of S/N for the individual observing pattern versus the ABAB pattern is then:

$$\frac{\frac{S}{N}(nA - B)}{\frac{S}{N}(n(A-B))} = \sqrt{\frac{2n(n^2+1)}{(n+1)(n+n^2)}} = \sqrt{2\frac{n^2+1}{(n+1)^2}} \tag{A.67}$$

For the example from figure A.5, where I get an optimal n of 7 for a taget/sky flux ratio of 50, the S/N is improved by a factor of $\sqrt{2\frac{n^2+1}{(n+1)^2}} = 1.25$ or 25 percent.

In the limit $n \rightarrow \infty$ I get:

$$\lim_{n\rightarrow\infty} \frac{n^2+^1}{(n+1)^2} = 1 \tag{A.68}$$

$$\lim_{n\rightarrow\infty} max = \sqrt{2} \tag{A.69}$$

This means, that the maximum increase in efficiency is by the factor of $\sqrt{2}$ in the extremal case of $n \rightarrow \infty$. This is the case, when no background observations are conducted at all. Thus the observation time on target is doubled, leading to an increased signal by a factor of $\sqrt{2}$.

A.3.4. Application to my observation

In the observations described in chapter 2 the host stars (HD 209458b and HD 189733b) are about 6th magnitude in the K-Band. The background (sky+telescope) is approximately about $12.6\ mag/arcsec^2$ (Allen, 1973). For SINFONI the FOV is $3\ arcsec \times 3\ arcsec = 9\ arcsec^2$ in the $50 \times 100\ mas$ scale and $0.8\ arcsec \times 0.8\ arcsec = 0.64\ arcsec^2$ in the $12.5 \times 25\ mas$ scale.

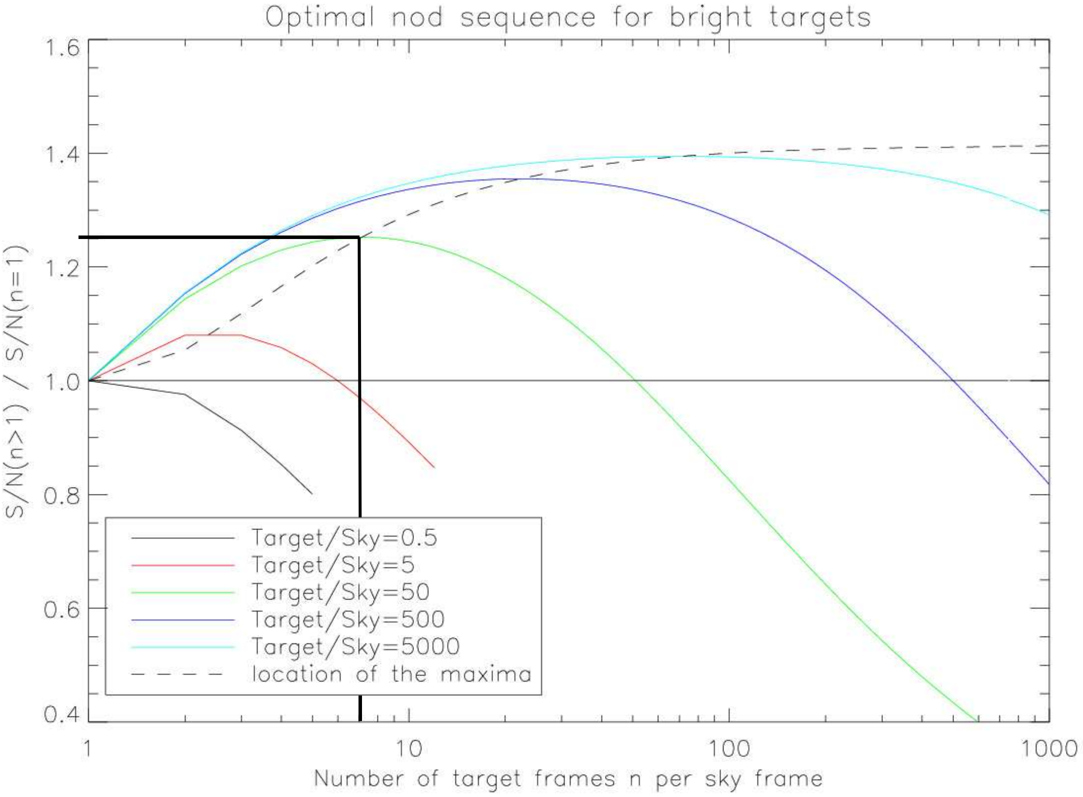

Figure A.5.: Figure to explain the optimal nod sequence for bright targets. The plot shows the improvement of S/N for 5 cases of target flux/ background flux (0.5, 5, 50, 500, 5000) (black, red, green, dark blue, light blue). The lines show the ratio (y-axis) of the S/N when observed in a nABnAB pattern, and the S/N when observed in an ABAB fashion, plotted against n (x-axis). For the example of the green curve, where the target is assumed to be 50 times brighter than the background, the optimal n is 7, leading to an improved S/N by a factor of 1.25, i.e. this strategy improves the S/N by 25 percent.

Then the ratio x of target signal S_o and background signal S_s is:

$$x = \frac{S_o}{S_s} = 10^{(12.6-6)0.4}\frac{1}{arcsec^2} = 405.509\frac{1}{arcsec^2} \tag{A.70}$$

This leads to the ratios x_{100} and x_{25} for the 100 mas and the 25 mas scales of SINFONI of:

$$x_{100} = 45.06, x_{25} = 633.6 \tag{A.71}$$

It should be mentioned that these calculations are on the conservative side since I usually do not extract the spectrum from the total FOV, but only from an aperture that is significantly smaller. These numbers in mind, the final decision for my observation was to use n=8, i.e. to observe 8 target frames and then one sky frame. This is also on the very conservative side, especially for the 25 mas scale. The reason for this was to also trace temporal changes in the background, that happen on similar timescales. The results also show that, in terms of background correction, the best choice for observational setup is always the smallest possible scale.

B. Appendix II

B.1. Tables

B.1.1. Python routines used, SINFONI pipeline

The following list provides the PYTHON-routines of the ESO standard reduction pipeline that were used in this work:

- `spredCreateBaxpix.py`: discovers bad pixels by comparing the surrounding area of a pixel in dark- and flatfield-exposures
- `spredCreateBaxpixLin.py`: discovers non-linear pixels in a set of flatfield exposures with increasing exposure time
- `spredCreateNoise.py`: discovers noisy pixels in a set of dark- or flatfield exposures with identical setup
- `spredCombineBadpix.py`: combines a set of bad pixel masks to a global mask
- `lampflats.py`: computes a global flatfield frame from sets of dark frames and flatfields
- `spredFindDistortion.py`: computes and corrects distortions in the field of view, identifies slitlet positions
- `spredWaveCal.py`: prepares a wavelength calibration map from Helium, Neon or Argon-lamp exposures and corresponding linelists
- `spredPrepFrame.py`: prepares the raw-frames (bad pixel correction, flatfielding, background subtraction etc.)
- `spredCreateCube.py`: reconstructs the 3d-data cube from the prepared 2d raw exposures

B.1.2. The SPIFFI/SINFONI Instrument

Feature	Value	Unit
Central wavelength	1.95(*), 2.05 (**)	μm
Spectral resolution R	1500 (*) 4000 (**)	
Pixel	2048 x 2048	
Dark current	0.27	e^-/sec
Instrument transmission	0.45	
Quantum-efficiency	0.7	
Transmission adaptive optics	0.85	
Read-out noise	18.1	e^-
Max. electrons	30000	e^-/pixel
Max. photons	64000	photons/pixel

(*): in H+K mode (**): in K mode

B.1.3. The Very Large Telescope

Feature	Value	Unit
Diameter primary mirror	8	m
Diameter secondary mirror	1.6	m
Expected seeing (*)	0.8	arcsec
Transmission telescope	0.8	
Background contribution (**)	12.06	mag
Temperature telescope	270	K

(*): at the Paranal site

(**): for observations in H- or K-Band

Bibliography

[Allen(1973)] Allen, C. W. 1973, London: University of London, Athlone Press, |c1973, 3rd ed.,

[Allington-Smith et al.(1998)] Allington-Smith, J. R., Content, R., & Haynes, R. 1998, Proc. of the SPIE, 3355, 196

[Angerhausen (2006)] Angerhausen, D. et al. 2006, in: McLean, Ian S.; Iye, Masanori (eds.), *Ground-based and Airborne Instrumentation for Astronomy*, Proc. of the SPIE, 6269, 62694S

[Angerhausen (2007)] Angerhausen, D. et al. 2007, in: C. Afonso, D. Weldrake, and Th. Henning (eds.), *Transiting Extrasolar Planets Workshop*, ASP Conference Series, 366, 262

[Angerhausen et al.(2009)] Angerhausen, D., Krabbe, A., & Iserlohe, C. 2009, IAU Symposium, 253, 552

[Arribas(2006)] Arribas, S. et al. 2006, *PASP*, 118, 839, 21-36

[Atreya(1986)] Atreya, S. K. 1986, Atmospheres and Ionospheres of the Outer Planets and their Satellites, XIII, 224 pp. 90 figs. (partly in color). Springer-Verlag Berlin Heidelberg New York. Also Physics and Chemistry in Space, volume 15,

[Bakos et al.(2006)] Bakos, G. Á., et al. 2006, ApJ, 650, 1160

[Barman (2005)] Barman, T. 2005, *ApJ*, 632, 1132-1139

[Beckers(1993)] Beckers, J. M. 1993, ARA&A, 31, 13

[Bonnet et al.(2003)] Bonnet, H., et al. 2003, Proc. SPIE, 4839, 329

[Bouchy et al.(2005)] Bouchy, F., et al. 2005, A&A, 444, L15

[Broeg & Wuchterl(2007)] Broeg, C., & Wuchterl, G. 2007, *MNRAS*, 376, L62

[Burrows(2007)] Burrows, A. 2007, Bulletin of the American Astronomical Society, 38, 231

[Carter et al.(2009)] Carter, J. A., Winn, J. N., Gilliland, R., & Holman, M. J. 2009, *ApJ*, 696, 241

[Charbonneau et al.(2002)] Charbonneau, D., Brown, T. M., Noyes, R. W., & Gilliland, R. L. 2002, ApJ, 568, 377

[Charbonneau(2003)] Charbonneau, D. 2003, Scientific Frontiers in Research on Extrasolar Planets, 294, 449

[Charbonneau et al.(2008)] Charbonneau, D.; Knutson, H. A.; Barman, T.; Allen, L. E.; Mayor, M.; Megeath, S. T.; Queloz, D.; Udry, S. 2008, *ApJ*, 686, 1341

[Deming et al.(2006)] Deming, D., Harrington, J., Seager, S., & Richardson, L. J. 2006, ApJ, 644, 560

[Deming et al.(2007)] Deming, D.; Harrington, J.; Laughlin, G.; Seager, S.; Navarro, B.; Bowman, W. C.; Horning, K. 2007,*ApJ*, 667, L199

[Deming et al.(2009)] Deming, D., et al. 2009, PASP, 121, 952

[Dunham et al.(2007)] Dunham, E. W., Elliot, J. L., Brown, T. M., Charbonneau, D., & McLean, I. S. 2007, Transiting Extrapolar Planets Workshop, 366, 256

[Eisenhauer et al.(2003)] Eisenhauer, F., et al. 2003, Proc. SPIE, 4841, 1548

[Figueira et al.(2009)] Figueira, P.; Pont, F.; Mordasini, C.; Alibert, Y.; Georgy, C.; Benz, W. 2009, *A&AS*, 493, 671

[Fortney et al.(2006)] Fortney, J. J., Saumon, D., Marley, M. S., Lodders, K., & Freedman, R. S. 2006, *ApJ*, 642, 495

[Fortney et al.(2008)] Fortney, J. J., Lodders, K., Marley, M. S., & Freedman, R. S. 2008, *ApJ*, 678, 1419

[Fossey et al.(2009)] Fossey, S. J., Waldmann, I. P., & Kipping, D. M. 2009, *MNRAS*, 396, L16

[Garcia-Melendo & McCullough(2009)] Garcia-Melendo, E., & McCullough, P. R. 2009, *ApJ*, 698, 558

[Gaudi & Winn(2007)] Gaudi, B. S., & Winn, J. N. 2007, *ApJ*, 655, 550

[Gillon et al.(2005)] Gillon, M., Courbin, F., Magain, P., & Borguet, B. 2005, *A&AS*, 442, 731

[Gillon et al.(2007)] Gillon, M.; Pont, F.; Demory, B.-O.; Mallmann, F.; Mayor, M.; Mazeh, T.; Queloz, D.; Shporer, A.; Udry, S.; Vuissoz, C. 2007, *A&AS*, 472, L13

[Grillmair et al.(2007)] Grillmair, C. J., Charbonneau, D., Burrows, A., Armus, L., Stauffer, J., Meadows, V., Van Cleve, J., & Levine, D. 2007, ApJ, 658, L115

[Grillmair et al.(2008)] Grillmair, C. J.; Burrows, A.; Charbonneau, D.; Armus, L.; Stauffer, J.; Meadows, V.; van Cleve, J.; von Braun, K.; Levine, D. 2008, *Nature*, Volume 456, 767

[Grillmair et al.(2008)] Grillmair, C. J.; Burrows, A.; Charbonneau, D.; Armus, L.; Stauffer, J.; Meadows, V.; van Cleve, J.; von Braun, K.; Levine, D. 2008, Nature, Volume 456, 767

[Knutson et al.(2008)] Knutson, H. A.; Charbonneau, D.; Allen, L. E.; Burrows, A.; Megeath, S. T. 2008, ApJ, 673, 526

[Henry et al.(2000)] Henry, G. W., Marcy, G. W., Butler, R. P., & Vogt, S. S. 2000, *ApJ*, 529, L41

[Hubeny & Burrows(2007)] Hubeny, I., & Burrows, A. 2007, *ApJ*, 669, 1248

[Ikoma et al.(2006)] Ikoma, M., Guillot, T., Genda, H., Tanigawa, T., & Ida, S. 2006, *ApJ*, 650, 1150

[Iro(2008)] Iro, N. 2008, Bulletin of the American Astronomical Society, 40, 402

[Irwin(2003)] Irwin, P. G. J. 2003, Giant planets of our solar system : atmospheres, compositions, and structure, by P.G.J. Irwin. Springer Praxis books in geophysical sciences. Berlin: Springer, 2003

[Kallrath & Milone(1999)] Kallrath, J., & Milone, E. F. 1999, Eclipsing binary stars : modeling and analysis / Joseph Kallrath, Eugene F. Milone. New York : Springer, 1999. (Astronomy and astrophysics library),

[Knutson et al.(2008)] Knutson, H. A.; Charbonneau, D.; Allen, L. E.; Burrows, A.; Megeath, S. T. 2008, *ApJ*, 673, 526

[Knutson et al.(2009)] Knutson, H. A., et al. 2009, ApJ, 690, 822

[Laughlin 2005] Laughlin G. et al. 2005, ApJ, 629, L121 11

[Laughlin et al.(2009)] Laughlin, G., Deming, D., Langton, J., Kasen, D., Vogt, S., Butler, P., Rivera, E., & Meschiari, S. 2009, *Nature*, 457, 562

[Lord (1992)] Lord, S. D., 1992, NASA Technical Memorandum 103957

[Mandel & Agol(2002)] Mandel, K. & Agol, E. 2002, ApJ, 580, L171

[Marois et al.(2008)] Marois, C., Macintosh, B., Barman, T., Zuckerman, B., Song, I., Patience, J., Lafrenière, D., & Doyon, R. 2008, Science, 322, 1348

[Mayor & Queloz(1995)] Mayor, M., & Queloz, D. 1995, *Nature*, 378, 355

[Moutou et al.(2009)] Moutou, C., et al. 2009, *A&AS*, 498, L5

[Naef et al.(2001)] Naef, D., et al. 2001, *A&AS*, 375, L27

[Nutzman et al.(2009)] Nutzman, P., Charbonneau, D., Winn, J. N., Knutson, H. A., Fortney, J. J., Holman, M. J., & Agol, E. 2009, *ApJ*, 692, 229

[Pearson, K. (1901)] earson, K. 1901, 'On Lines and Planes of Closest Fit to Systems of Points in Space', Philosophical Magazine 2 (6) 559

[Pont et al.(2008)] Pont, F., Knutson, H., Gilliland, R. L., Moutou, C., & Charbonneau, D. 2008, *MNRAS*, 385, 109

[Pont et al.(2009)] Pont, F.; Gilliland, R. L.; Knutson, H.; Holman, M.; Charbonneau, D. 2009, *ApJ*, 224, 39

[Richardson et al.(2007)] Richardson, L. J.; Deming, D.; Horning, K.; Seager, S. & Harrington, J. 2007, *Nature*, 445, 892

[Sandell et al.(2003)] Sandell, G., Becklin, E. E., & Dunham, E. W. 2003, Scientific Frontiers in Research on Extrasolar Planets, 294, 591

[Sato et al.(2005)] Sato, B., et al. 2005, *ApJ*, 633, 465

[Sing et al.(2009)] Sing, D. K.; Vidal-Madjar, A.; Désert, J.-M.; Lecavelier des Etangs, A.; Ballester, G. 2008, *ApJ*, 686, 658

[Swain et al.(2008)] Swain, M. R.; Vasisht, G.; Tinetti, G. 2008, *Nature*, 452, 329

[Swain, Vasisht & Tinetti (2008)] Swain, M. R.; Vasisht, G.; Tinetti, G. 2008, Nature, 452, 329

[Swain et al.(2009a)] Swain, M. R., Vasisht, G., Tinetti, G., Bouwman, J., Chen, P., Yung, Y., Deming, D., & Deroo, P. 2009, ApJ, 690, L114

[Swain et al.(2009b)] Swain,M. R. ; Tinetti, G.; Vasisht, G.; Deroo, P.; Griffith, C.; Bouwman, J.; Pin Chen; Yung, Y.; Burrows, A.; Brown, L.; Matthews, J.; Roe, J. F.; Kuschnig, R.; Angerhausen D. 2009, ApJ, 704, 1616

[Swain et al.(2010)] Swain, M. R., et al. 2010, Nature, 463, 637

[Thatte et al.(1998)] Thatte, N. A., et al. 1998, Proc. SPIE, 3353, 704

[Tinetti et al.(2010)] Tinetti, G., Deroo, P., Swain, M. R., Griffith, C. A., Vasisht, G., Brown, L. R., Burke, C., & McCullough, P. 2010, ApJ, 712, L139

[Westmoquette et al.(2009)] Westmoquette, M. S., Exter, K. M., Christensen, L., Maier, M., Lemoine-Busserolle, M., Turner, J., & Marquart, T. 2009, arXiv:0905.3054

[Wiseman et al. (2006)] . Wiseman et al., Space-Based ’Probe Class’ Missions for Exoplanet Research, NASA white paper

[Winn et al.(2008)] Winn, J. N., Henry, G. W., Torres, G., & Holman, M. J. 2008, *ApJ*, 675, 1531

[Wittenmyer 2005] Wittenmyer R. A. et al. 2005, *ApJ*, 632, 1157

Acknowledgements

Ich möchte mich bei allen, die mich während der Durchführung dieser Arbeit und während meines gesamten Studiums unterstützt haben, bedanken.

Ganz besonderer Dank gilt meiner Familie, ohne deren Unterstützung diese Arbeit und mein gesamtes Studium nicht möglich gewesen wäre: Ursula und Paul Angerhausen, Katrin, Martin und Tom Pütz. Insbesondere meinen beiden Grossmüttern, Therese Angerhausen und Christel Lentzen, gilt mein ganzer Dank.

Herrn Professor Alfred Krabbe danke ich für die Möglichkeit der Durchführung der Dissertation zu diesem Thema in seiner Arbeitsgruppe, für die Unterstützung, die Ideen und Vorschläge und das grosse Interesse am Fortgang der Arbeit und den Ergebnissen. Herrn Professor Kley danke ich für seine Unterstützung als Zweitgutachter.

Ebenfalls bedanken möchte ich mich bei Christof Iserlohe und Gautam Vasisht, stellvertretend für die vielen anderen Kollegen am I. Physikalischen Institut in Köln, am NASA-JPL/Caltech und am Institut für Raumfahrtsysteme der Uni Stuttgart. Die hervorragende Teamarbeit, das gute Arbeitsklima, die vielen aufschlussreichen und fruchtbaren Diskussionen haben diese Dissertation erst möglich gemacht.